Experiments on Whistler Wave Dispersion in Bounded Magnetised Plasmas

Reprint of the

INAUGURALDISSERTATION

zur

Erlangung des akademischen Grades eines

doctor rerum naturalium (Dr. rer. nat.)

an der Mathematisch-Naturwissenschaftlichen Fakultät

der

Ernst-Moritz-Arndt-Universität Greifswald

vorgelegt von

Christian M. Franck

geboren am 16.02.1973

in Bonn

Greifswald, im Januar 2003

Dekan:	Prof. Dr. Jan-Peter Hildebrandt
1. Gutachter:	Prof. Dr. Thomas Klinger
2. Gutachter:	Prof. Dr. Hans Pécseli
Tag der Promotion:	05.03.2003

Abstract

Within the scope of this work, a versatile large linear magnetised plasma experiment was designed, constructed, and subsequently put into operation. The magnetised plasma was used to investigate the dispersion of whistler waves (circular polarised electromagnetic waves) with regard to the influence of the plasma boundaries. After a brief review over electromagnetic plasma waves and the three discharge modes of a helicon source, the experimental device and the diagnostic tools are explained in detail. Great attention is devoted to the identification of a reliable, calibrated magnetic fluctuation probe design. To the understanding of dynamical phenomena in ionospheric plasmas, whistler wave measurements in laboratory experiments may contribute significantly because of the ability to vary plasma parameters and to do measurements with high spatial and temporal resolution. However, the boundaries of laboratory experiments change the dispersion behaviour of whistler waves significantly if compared to the unbounded ionospheric situation. The influence of the plasma boundary is studied in the present work on three different levels of increasing complexity. First, a high density, small wavelength regime is established to make the effect of the boundary negligible. Measurements are in full agreement with whistler wave theory for unbounded plasma geometry. Measurements below the ion cyclotron frequency reveal the strong influence of the ion dynamics on whistler wave propagation, but are not straightforward to interpret in terms of dispersion theory. Second, the other limit case is examined: bounded plasma helicon modes. These waves are, mathematically speaking, eigenfunctions of the plasma-boundary system and are of great practical importance for high density plasma discharges, the helicon source. Careful measurements of the equilibrium plasma parameters as well as the magnetic fluctuation profiles of the helicon source are done in all three modes of operation, the capacitive, inductive, and helicon wave sustained mode. The first two modes are fairly well understood and the measurements are consistent with existing models. The high density helicon mode, however, is still a scientific case. The measurements partially confirm existing assumptions. It is demonstrated that the plasma production is detached from the antenna edge region. Moreover, it is shown that the plasma parameters are self-consistently determined by the antenna geometry and the discharge parameters according to basic helicon wave theory. Finally, it is ruled out that the plasma density is the control parameter determining the transition point into the high density helicon mode. The measurements rather suggest that the rf power density is the important value. As a third aspect, whistler waves in an intermediate wavelength regime are studied and the transition from unbounded to bounded plasma wave dispersion is systematically investigated. It is shown both experimentally

and numerically that the wave dispersion in a plasma filled metal waveguide cannot be determined solely from wave vector measurements parallel to the magnetic field. For a correct description, the perpendicular mode profile has to be correctly taken into account. In contrast to simple helicon wave theory, it is demonstrated that the perpendicular mode profile is not only determined by the conducting vessel boundaries alone but the entire plasma-boundary system has to be considered as a unity. To summarise, this work has contributed to a better understanding of the physics of the propagation of whistler waves, where the particular role of metal boundaries acting as wave guides was highlighted. This basic science approach to the waves' dynamics is believed to be of significance in the course of the scientific debate on the physics principles of helicon discharges.

Zusammenfassung

Im Rahmen dieser Arbeit wurde eine große, universell einsetzbare, linear magnetisierte Plasmaanlage entworfen, konstruiert und erfolgreich in Betrieb genommen. In dieser Anlage wurden Experimente durchgeführt, die den Einfluss der Plasmaberandung auf die Dispersion von Whistlerwellen untersuchen. Die Arbeit wird durch eine kurze Einführung in die Physik von Plasmawellen und einem Überblick über die drei Entladungsmodi einer Helikonquelle eingeleitet. Anschließend werden das Plasmaexperiment und die verwendeten Diagnostiken erläutert. Besonderes Augenmerk ist auf die Konstruktion einer zuverlässigen und absolut kalibrierten magnetischen Fluktuationssonde gelegt worden. Im Gegensatz zu natürlichen, ionosphärischen Plasmen können die Plasmaparameter in Laborplasmen über einen großen Bereich hinweg kontrolliert werden und Messungen können mit hoher räumlicher und zeitlicher Auflösung durchgeführt werden. Dafür sind Laborplasmen aber gezwungener Maßen immer berandet und die Dispersionseigenschaften von Wellen werden dadurch mehr oder weniger stark verändert. In dieser Arbeit wird der Einfluss der Plasmaberandung in drei verschieden starken Ausprägungen untersucht. Zum einen wird gezeigt, dass der Einfluss der Berandung in Plasmen hoher Dichte und bei kleinen Wellenlängen vernachlässigbar gering ist. Messungen in der Nähe der Ionenzyklotronfrequenz zeigen den Einfluss der Ionen auf die Dispersion. Zum zweiten werden Wellen in stark berandeten Plasmen untersucht, so genannte Helikonwellen. Diese sind Eigenfunktionen des Plasma-Berandungs-Systems und haben z.B. in Helikonquellen eine weit verbreitete Anwendung gefunden. Räumlich hoch aufgelöste Messungen sowohl der Plasmaparameter als auch der magnetischen Fluktuationsprofile sind in allen drei Entladungmodi der Helikonquelle aufgenommen worden. Die Mechanismen des kapazitiven und induktiven Entladungsmodus sind in der Literatur zufriedenstellend erklärt und können mit den hier gezeigten Messungen voll bestätigt werden. Der Entladungsmechanismus des Helikonmodes hingegen ist immer noch in der Diskussion und gängige Annahmen können teilweise bestätigt werden. So ist z.B. die Plasmaproduktion von der Antennenrandschicht entkoppelt, was eindeutig gezeigt werden kann und auf Wellenheizung hindeutet. Desweiteren stellen sich die Plasmaparameter in Übereinstimmung zur Theorie selbstkonsistent mit den geometrischen Antennenabmessungen und den Entladungsparametern ein. Hingegen wird ausgeschlossen, dass die Plasmadichte der Kontrollparameter ist, der den Punkt des sprunghaften Übergangs in den Helikonmodus bestimmt. Die Messungen deuten eher darauf hin, dass die Leistungsdichte der RF-Antenne hierfür verantwortlich ist. Als dritten Aspekt des Berandungseinflusses wird die Wellenausbreitung in einem Bereich zwischen stark berandetem und

unberandetem Plasma untersucht. In Experimenten und mit Hilfe numerischer Berechnungen wird gezeigt, dass die Bestimmung der Wellenvektoren parallel zum Magnetfeld allein nicht ausreicht, um die Dispersion zufriedenstellend anzugeben. Vielmehr muss auch das senkrechte Wellenfeld für eine exakte Beschreibung berücksichtigt werden. Das senkrechte Wellenfeld ist, ganz im Gegensatz zu einfachen Theorien, nicht allein durch die leitende Berandung des Experiments gegeben, sondern muss aus dem gesamten Plasma-Gefäß-System bestimmt werden. Alles in allem trägt diese Arbeit zur wissenschaftlichen Diskussion um die Grundlagen der Wellenausbreitung in Plasmen bei. Besonders die Rolle der oft vernachlässigten Plasmaberandung wird dabei berücksichtigt und somit auch ein Beitrag zur derzeitigen intensiven Diskussion um den effizienten Entladungsmechanismus der Helikonquelle geleistet.

Contents

1

Introduction

Waves are almost ubiquitous in plasmas, which are mostly not in global thermal equilibrium. Waves can be driven by electric and magnetic fields or density and temperature gradients. There are numerous different waves in plasmas and especially the anisotropy due to an ambient magnetic field creates a great complexity in wave description and opens up an entire 'zoo' of plasma wave eigenmodes. Plasma waves are often classified in electrostatic or electromagnetic waves. Moreover, the direction of propagation and polarisation with respect to the magnetic field is often used for detailed classification. Mostly, the wave polarisation is a mixture of transverse and longitudinal polarisation. Wave modes are identified by their dispersion relation, the functional dependence between wavelength and wave frequency. From the dispersion relation, phase and group velocity of the wave, resonances and cut-off points can be derived.

The first observations of plasma waves were reported more than a century ago by Preece [1894] and Barkhausen [1919], long before plasma physics became a field of research itself. These so-called 'whistler waves' were heard on telephone lines and during the interception of enemy radio communication as whistling sounds with constant amplitude and declining frequency. Owing to their typical sound, they were named whistler waves. It was not until 1930 that this phenomenon was correctly described as the highly dispersive broadening of a sharp pulse, initiated by lightning [Barkhausen, 1930], that propagates in the ionosphere [Eckersley, 1935]. Whistler waves are right-hand circular polarised electromagnetic waves propagating mainly parallel to the magnetic field with frequencies below the electron cyclotron frequency. Since their first observation and subsequent explanation, the interest in whistler waves has steadily grown since they are an excellent diagnostic probe of the ionosphere. Whistler waves yield information, especially on the plasma density, along their path of propagation through the ionosphere.

A good understanding of the ionosphere, e.g. the plasma density distribution and its temporal variations, was and still is important. In the first half of the 20^{th} century, long range radio communication used electromagnetic waves with medium and long wavelengths ($\approx 100\,\text{m}$–$1\,\text{km}$). Reflections at the ionospheric plasma boundary enabled transmission beyond the horizon and therefore, a good knowledge of the ionospheric layer was important [Hutchinson, 2001]. Nowadays, much shorter wavelengths in the microwave range

are used for satellite based communication and positioning systems [Hofmann-Wellenhof et al., 2001; Klawitter, 2000]. For the increasing demand in precision in the operation of such systems, an even more detailed understanding of the ionosphere and its temporal evolution is required. The analogous counterpart, the left-hand polarised electromagnetic wave called ion whistler wave, propagates at frequencies below the ion cyclotron frequency and was observed in ionospheric plasmas by means of satellite recordings [Smith et al., 1964]. Gurnett et al. [1965] showed the coupling of these two types of waves and the generation of ion whistler waves was explained by the coupling to a conventionally triggered whistler wave. Refined analysis [Smith and Brice, 1964] in plasmas with multiple ion species enables the possibility of determining the ion species composition in the ionosphere [McEwen and Barrington, 1968]. And in our days, still, whistler wave measurements are amongst the key diagnostic tools to probe the ionosphere, passively observed as well as actively excited [Clilverd et al., 1991; Richards et al., 2000; Sonwalkar et al., 2001]. They are used to study daily or annual variations, as well as for the investigation of turbulent phenomena in the ionosphere [Muschietti et al., 1997; Trakhtengerts and Rycroft, 1998]. Whistler waves are not only interesting as a diagnostic tool. They are important as well for the understanding of certain dynamical phenomena itself. For example, high intensity bursts of lower hybrid waves near density striations were shown to be caused by linear mode-coupling with whistler waves [Bamber et al., 1994].

Early measurement in ionospheric plasmas were only possible from ground-based stations. Later, satellites and sounding rockets were increasingly used for whistler wave investigations. All these measurements are naturally limited in spatial resolution and lack the possibility of systematically studying the dependence of the whistler waves on plasma parameters. Experiments performed in the laboratory do not encounter these shortcomings and since the first laboratory whistler wave experiments by Gallet et al. [1960], measurements on propagation, damping, ducting as well as on resonance cones and antenna radiation patterns led to a profound understanding and stimulated many advances in plasma wave theory. The current whistler wave research deals primarily with their role in magnetic reconnection and energetic particle precipitation as well as antenna-wave coupling and the coupling into the earth-ionosphere waveguide [Stenzel, 1999]. The main difference to ionospheric plasmas is that laboratory plasmas are naturally always bounded. The influence of the plasma boundaries on the dispersion of electromagnetic waves was already theoretically investigated [Klozenberg et al., 1965; Uhm et al., 1988] but in experiments mostly circumvented by using small wavelengths [Gallet et al., 1960; Mahaffey, 1963] and large sized experimental devices [Stenzel, 1976; Mattoo et al., 2001].

Low frequency whistler waves in bounded plasma geometry, so-called ‘helicon’ waves, have attracted a lot of attention since Boswell [1984b] reported on their use for producing a plasma with surprisingly high efficiency. They have been studied in cylindrical radio frequency (rf) produced plasma by Lehane and Thonemann [1965] as well as in the free electron gas of solid metals by Legéndy [1965] and Harding and Thonemann [1965]. In contrast to the above discussed whistler waves, the dispersion of these waves depends

strongly on the boundary conditions as the waves are essentially the eigenfunctions of the plasma-boundary system [Boswell, 1984a; Chen, 1991]. Today, helicon plasma sources are widely established in research labs all around the world. Nevertheless, the discharge mechanism itself is still strongly discussed. Different explanations have been proposed [Chen, 1991; Shamrai and Taranov, 1996; Kwak et al., 1997; Cho, 2000], but so far no clear-cut picture could be developed, despite intensive experimental and numerical effort (see e.g. the reviews by Boswell and Chen [1997] and Chen and Boswell [1997]). Current research activity focusses on characterising the discharge to clarify the heating mechanism itself and on identifying the important plasma parameters that lead to efficient transfer from wave to particle energy. An overview of current topics is found in the contributions to the APS Mini-Conference on Applications of Helicon Plasma Sources [2001]. Finally, the role of reliable diagnostics for increasingly accurate measurements in helicon discharges is becoming more and more recognised [Light et al., 1995; Chen and Blackwell, 1999; Blackwell et al., 2002].

The present work analyses the whistler wave dispersion in bounded plasma geometry. According to the influence of the boundaries on the wave, three different research areas can be defined. First, electron and ion whistler waves are excited and measured in a regime, where the influence of the plasma boundary is negligible. In a second regime, the boundaries are essential as the wave is established as an eigenfunction of the plasma-boundary system. Low frequency helicon waves and their role in helicon plasma sources are investigated. And third, the wave dispersion in the intermediate regime between both extreme situations, the transition from unbounded to bounded plasma geometry, is studied both experimentally and numerically.

The present work is structured as follows: The theoretical framework on whistler waves in unbounded and bounded plasma geometry is briefly reviewed in Chap. 2. Helicon sources are known to operate in three different modes, depending on the ambient magnetic field strength and the applied rf power. In Chap. 3, the capacitive, inductive, and helicon wave sustained discharge modes are introduced and, as far as possible, explained in their physics. In the subsequent Chap. 4, the diagnostic tools and the experimental setup are described. Special attention is devoted to the new plasma device VINETA which was developed and constructed in the frame of the present work. The flexibility of the device not only enabled the present experimental investigations but also ensures numerous further experiments and other research activities. The main diagnostic tools for the present work are magnetic fluctuation probes that were carefully characterised and calibrated in an independent test bed. Basic electron and ion whistler wave experiments are reported in Chap. 5. To our knowledge, ion whistler waves have been excited and measured in a laboratory plasma for the first time. Chap. 6 is devoted to a detailed experimental characterisation of the different rf discharge modes in the VINETA. The stationary plasma profile parameters are measured with high spatial resolution and the different magnetic eigenmode structures are studied. The helicon mode is characterised in some more detail, thereby combining measurements of the mode structure in planes parallel and perpendic-

ular to the magnetic field with dispersion measurements at different ambient magnetic fields. The role of parameters that define the critical point of the transition to the helicon discharge mode is investigated. Chap. 7 reports on detailed measurements and numerical simulations to analyse the dispersion of waves in the transition regime between approximately unbounded and strongly bounded plasma geometry. The discussion in Chap. 8 and the summary in Chap. 9 conclude the work.

2

Theory of Whistler Waves

Whistler waves belong to the class of waves in magnetised plasmas with the group velocity mainly parallel to the magnetic field. The basic theory of whistler waves is covered in textbooks and review articles such as Swanson [1989]; Stix [1992]; Yeh and Liu [1972], and Al'pert [1980] and Stenzel [1999]. In order to interpret and classify the wave experiments considered in the present thesis, plasma waves are introduced theoretically in this chapter. The derivation follows the well established approach of Stix [1992] and Swanson [1989] and the waves are classified by their different roots in the cold plasma wave dispersion relation. Starting from Maxwells' equations and the cold plasma particle equations, the dielectric tensor and the dispersion relation are derived in Secs. 2.1 and 2.2. This general formalism leads directly to the dispersion of ion and electron whistler waves which are covered in Sec. 2.3. In laboratory experiments the plasma is necessarily always bounded and the theoretical models on bounded wave propagation are reviewed in Sec. 2.4.

2.1 Plasma Dielectric Tensor

The dispersion relation for a plasma can be obtained from solving Maxwells' equations together with the currents and fields in the plasma.

$$\boldsymbol{\nabla} \times \boldsymbol{B} = \mu_0 \left(\boldsymbol{j} + \epsilon_0 \frac{\partial \boldsymbol{E}}{\partial t} \right) = \mu_0 \left(\frac{\partial \boldsymbol{D}}{\partial t} \right) \tag{2.1}$$

$$\boldsymbol{\nabla} \times \boldsymbol{E} = -\frac{\partial \boldsymbol{B}}{\partial t} \tag{2.2}$$

$$\boldsymbol{\nabla} \cdot \boldsymbol{D} = \rho_{el} \tag{2.3}$$

$$\boldsymbol{\nabla} \cdot \boldsymbol{B} = 0\,, \tag{2.4}$$

where $\boldsymbol{E}$ is the electric field and $\boldsymbol{D} = \epsilon \boldsymbol{E}$ is the electric displacement. In a anisotropic medium like a magnetised plasma, the scalar dielectric permittivity ϵ is replaced by the effective dielectric permittivity tensor $\underline{\epsilon}$ and

$$\boldsymbol{D} = \underline{\epsilon} \cdot \boldsymbol{E} = \epsilon_0 \underline{\epsilon_r} \cdot \boldsymbol{E}\,. \tag{2.5}$$

Here, $\underline{\epsilon_r}$ is the dimensionless relative dielectric permittivity tensor and will be derived below. The electric displacement current $\partial \boldsymbol{D}/\partial t$ includes the vacuum displacement current $\epsilon_0 \partial \boldsymbol{E}/\partial t$ and the plasma current $\boldsymbol{j}$. Furthermore, $\boldsymbol{B}$ is the magnetic induction and is related to the magnetic field $\boldsymbol{H}$ by $\boldsymbol{B} = \mu_r \mu_0 \boldsymbol{H}$. For plasmas it is suitable to take the relative magnetic permittivity $\mu_r = 1$. Finally, ρ_{el} is the electric charge density. As a consequence of charge conservation, electric charges and currents in a plasma are related to each other via the continuity equation

$$\boldsymbol{\nabla} \cdot \boldsymbol{j} + \frac{\partial \rho_{el}}{\partial t} = 0\,. \tag{2.6}$$

When the plasma can be treated as a conductor with losses due to particle collisions, it is convenient to relate the plasma current to the electric field using Ohm's law:

$$\boldsymbol{j} = \underline{\sigma} \cdot \boldsymbol{E}\,. \tag{2.7}$$

But, the displacement currents in a plasma often dominate and it is common to take the dielectric tensor $\underline{\epsilon}$ instead of using the conductivity tensor $\underline{\sigma}$. To simplify the subsequent calculations, a first set of assumptions is made.

Assumptions 1

- Zero order quantities are constant in time and space; specifically: background magnetic field $\boldsymbol{B_0}$ and plasma density n_0.
- First order quantities are small compared to zero order quantities and can be expressed as monochromatic waves $\propto \exp[\mathrm{i}(\boldsymbol{k}\cdot\boldsymbol{r} - \omega t)]$; in particular the magnetic and electric fluctuations $\boldsymbol{E_1}$, $\boldsymbol{B_1}$.
- Linear Approximation: The product of two first order quantities is negligibly small.

The spatial and temporal derivatives of first order quantities (e.g. $\boldsymbol{B_1}$) read in Fourier space

$$\frac{\partial \boldsymbol{B_1}}{\partial t} = -\mathrm{i}\omega \boldsymbol{B_1} \quad \text{and} \quad \boldsymbol{\nabla_r} \boldsymbol{B_1} = \mathrm{i}\boldsymbol{k}\boldsymbol{B_1}\,.$$

A further assumption is generally fulfilled as well:

Assumption 2

- There is no static electric field ($\boldsymbol{E_0} = \boldsymbol{0}$) and no particle drift ($\boldsymbol{v_0} = \boldsymbol{0}$) in the plasma.

Eqs. (2.1) and (2.5) can be rewritten in Fourier representation as

$$\begin{aligned} \underline{\sigma}\boldsymbol{E_1} - \mathrm{i}\omega\epsilon_0\boldsymbol{E_1} &= -\mathrm{i}\omega\boldsymbol{D_1} \\ \text{or} \quad \boldsymbol{D_1} &= \epsilon_0\left(\underline{1} + \frac{\mathrm{i}\underline{\sigma}}{\epsilon_0\omega}\right)\boldsymbol{E_1}\,. \end{aligned} \tag{2.8}$$

Comparing Eq. (2.8) with Eq. (2.5) yields that the dielectric tensor $\underline{\epsilon_r}$ is connected to the conductivity tensor $\underline{\sigma}$ of the plasma via

$$\underline{\epsilon_r} = \underline{1} + \frac{\mathrm{i}\underline{\sigma}}{\omega\epsilon_0}\,, \tag{2.9}$$

combining the conductive and the dielectric picture of the plasma mentioned above. But still, an explicit expression from basic plasma properties for the conductivity or dielectric tensor is missing. The calculations are further simplified by making

Assumption 3

- The plasma is cold and collisionless, i.e., there are no effects due to pressure gradients (e.g. acoustic waves).

The total current density $\boldsymbol{j}$ in the plasma is due to the motion of the charged particles of all involved species s

$$\boldsymbol{j} = \sum_s \boldsymbol{j_s} = \sum_s n_s q_s \boldsymbol{v_s}\,. \tag{2.10}$$

The particle equations of motion in the cold and collisionless limit read

$$m_s \frac{\mathrm{d}}{\mathrm{d}t}\boldsymbol{v_s} = q_s\left(\boldsymbol{E} + \boldsymbol{v_s}\times\boldsymbol{B}\right)\,. \tag{2.11}$$

With assumptions 1, these equations can be written in Fourier representation as

$$\begin{aligned} \boldsymbol{B} &= \boldsymbol{B_0} + \boldsymbol{B_1}\exp\left[\mathrm{i}(\boldsymbol{k}\cdot\boldsymbol{r} - \omega t)\right] \\ \boldsymbol{E} &= \boldsymbol{E_1}\exp\left[\mathrm{i}(\boldsymbol{k}\cdot\boldsymbol{r} - \omega t)\right] \\ \boldsymbol{v} &= \boldsymbol{v_1}\exp\left[\mathrm{i}(\boldsymbol{k}\cdot\boldsymbol{r} - \omega t)\right]. \end{aligned} \tag{2.12}$$

Without loss of generality, $\boldsymbol{B_0}$ is taken to be along the z-axis $\boldsymbol{B_0} = B_0\hat{\boldsymbol{e}}_z$. Substituting Eq. (2.13) into the equations of motion (2.11) yields

$$-\mathrm{i}\omega m_s \boldsymbol{v_{1s}} = q_s\left(\boldsymbol{E_1} + \boldsymbol{v_{1s}}\times\boldsymbol{B_0}\right). \tag{2.13}$$

The solution to these equations for each species s is

$$\begin{aligned} v_{xs} &= \frac{\mathrm{i}q_s}{m_s(\omega^2-\omega_{cs}^2)}\left(\omega E_x + \mathrm{i}\varepsilon_s\omega_{cs}E_y\right) \\ v_{ys} &= \frac{\mathrm{i}q_s}{m_s(\omega^2-\omega_{cs}^2)}\left(-\mathrm{i}\varepsilon_s\omega_{cs}E_x + \omega E_y\right) \\ v_{zs} &= \frac{\mathrm{i}q_s}{m_s\omega}E_z\,. \end{aligned} \tag{2.14}$$

Here, $\omega_{cs} = |q_s|B_0/m_s$ denotes the cyclotron frequency of the species s and $\varepsilon_s = q_s/|q_s|$ is the sign of its charge. Eqs. (2.14) combined with Eq. (2.10) are used to express the current density components in the plasma caused by particle motion

$$\begin{aligned} j_x &= \sum_s \frac{\mathrm{i}q_s^2 n_s}{m_s(\omega^2-\omega_{cs}^2)}\left(\omega E_x + \mathrm{i}\varepsilon_s\omega_{cs}E_y\right) \\ &= \mathrm{i}\epsilon_0\sum_s \frac{\omega_{ps}^2\omega}{\omega^2-\omega_{cs}^2}E_x - \epsilon_0\varepsilon_s\sum_s\frac{\omega_{ps}^2\omega_{cs}}{\omega^2-\omega_{cs}^2}E_y \end{aligned} \tag{2.15}$$

$$\begin{aligned} j_y &= \sum_s \frac{\mathrm{i}q_s^2 n_s}{m_s(\omega^2-\omega_{cs}^2)}\left(-\mathrm{i}\varepsilon_s\omega_{cs}E_x + \omega E_y\right) \\ &= \epsilon_0\varepsilon_s\sum_s \frac{\omega_{ps}^2\omega_{cs}}{\omega^2-\omega_{cs}^2}E_x + \mathrm{i}\epsilon_0\sum_s\frac{\omega_{ps}^2\omega}{\omega^2-\omega_{cs}^2}E_y \end{aligned} \tag{2.16}$$

$$\begin{aligned} j_z &= \sum_s \frac{\mathrm{i}q_s^2 n_s}{m_s\omega}E_z \\ &= \mathrm{i}\epsilon_0\sum_s\frac{\omega_{ps}^2}{\omega}E_Z\,, \end{aligned} \tag{2.17}$$

where $\omega_{ps} = \left(n_s q_s^2/m_s\epsilon_0\right)^{1/2}$ is the plasma frequency of the s^{th} species. Comparing the set of Eqs. (2.15–2.17) with Ohm's law (2.7) yields an expression for the conductivity $\underline{\sigma}$ of the plasma and the dielectric tensor $\underline{\epsilon_r}$ can be written from Eq. (2.9) as

$$\underline{\epsilon_r} = \begin{pmatrix} 1-\sum_s\frac{\omega_{ps}^2}{\omega^2-\omega_{cs}^2} & -\mathrm{i}\varepsilon_s\sum_s\frac{\omega_{ps}^2\omega_{cs}}{\omega(\omega^2-\omega_{cs}^2)} & 0 \\ \mathrm{i}\varepsilon_s\sum_s\frac{\omega_{ps}^2\omega_{cs}}{\omega(\omega^2-\omega_{cs}^2)} & 1-\sum_s\frac{\omega_{ps}^2}{\omega^2-\omega_{cs}^2} & 0 \\ 0 & 0 & 1-\sum_s\frac{\omega_{ps}^2}{\omega^2} \end{pmatrix}. \tag{2.18}$$

For future calculations it is convenient to introduce Stix [1992] notation

$$S \equiv 1-\sum_s\frac{\omega_{ps}^2}{\omega^2-\omega_{cs}^2} \tag{2.19}$$

$$D \equiv \sum_s\frac{\varepsilon_s\omega_{ps}^2\omega_{cs}}{\omega(\omega^2-\omega_{cs}^2)} \tag{2.20}$$

$$P \equiv 1 - \sum_s \frac{\omega_{ps}^2}{\omega^2} \tag{2.21}$$

$$R \equiv S + D = 1 - \sum_s \frac{\omega_{ps}^2}{\omega(\omega + \varepsilon_s \omega_{cs})} \tag{2.22}$$

$$L \equiv S - D = 1 - \sum_s \frac{\omega_{ps}^2}{\omega(\omega - \varepsilon_s \omega_{cs})}\,. \tag{2.23}$$

The dielectric tensor in this notation reads

$$\underline{\epsilon_r} = \begin{pmatrix} S & -\mathrm{i}D & 0 \\ \mathrm{i}D & S & 0 \\ 0 & 0 & P \end{pmatrix}. \tag{2.24}$$

2.2 Cold Plasma Dispersion Relation

As pointed out above, deriving the plasma dispersion relation means solving Maxwells' equations self-consistently including the plasma currents due to the plasma particle motions. Maxwells' Eqs. (2.1) and (2.2) written in Fourier space combined with Ohm's law Eq. (2.7) and Eq. (2.9) read

$$\mathrm{i}\boldsymbol{k} \times \boldsymbol{B} = \mu_0 \left(\underline{\sigma}\boldsymbol{E} - \mathrm{i}\omega\epsilon_0 \boldsymbol{E}\right) = -\mathrm{i}\omega\mu_0\epsilon_0\underline{\epsilon_r}\boldsymbol{E} \tag{2.25}$$

$$\mathrm{i}\boldsymbol{k} \times \boldsymbol{E} = \mathrm{i}\omega\boldsymbol{B}. \tag{2.26}$$

After taking the cross product with $\boldsymbol{k}$, Eq. (2.26) is substituted into Eq. (2.25) and $c^2 = 1/\mu_0\epsilon_0$ is used to obtain the wave equation

$$\boldsymbol{n} \times \boldsymbol{n} \times \boldsymbol{E} + \underline{\epsilon_r}\boldsymbol{E} = 0\,, \tag{2.27}$$

where $\boldsymbol{n} = \boldsymbol{k}c/\omega$ is the index of refraction vector and $\underline{\epsilon_r}$ the dielectric tensor derived in the previous section. $\boldsymbol{n}$ is pointing in the direction of the wave vector $\boldsymbol{k}$ and its magnitude is the index refraction. The convention is to choose $\boldsymbol{n}$ to lie in the x-z-plane as depicted in Fig. 2.1. θ is defined as the angle between $\boldsymbol{n}$ and the ambient magnetic field $\boldsymbol{B_0}$.

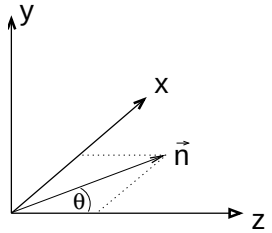

$$\boldsymbol{n} = \begin{pmatrix} n_x \\ 0 \\ n_z \end{pmatrix} = \begin{pmatrix} |\boldsymbol{n}| \sin\theta \\ 0 \\ |\boldsymbol{n}| \cos\theta \end{pmatrix} \tag{2.28}$$

Figure 2.1: The wave vector is defined to lie in the x-z-plane.

In this coordinate system, the first term in Eq. (2.27) reads

$$\boldsymbol{n} \times \boldsymbol{n} \times \boldsymbol{E} = \begin{pmatrix} -n^2 \cos^2\theta & 0 & n^2 \cos\theta \sin\theta \\ 0 & -n^2 & 0 \\ n^2 \cos\theta \sin\theta & 0 & -n^2 \sin^2\theta \end{pmatrix} \begin{pmatrix} E_x \\ E_y \\ E_z \end{pmatrix} . \tag{2.29}$$

The wave equation (2.27) now has the form

$$\begin{pmatrix} S - n^2 \cos^2\theta & -\mathrm{i}D & n^2 \cos\theta \sin\theta \\ \mathrm{i}D & S - n^2 & 0 \\ n^2 \cos\theta \sin\theta & 0 & P - n^2 \sin^2\theta \end{pmatrix} \begin{pmatrix} E_x \\ E_y \\ E_z \end{pmatrix} = 0 . \tag{2.30}$$

The requirement for nontrivial solutions is that the determinant of the coefficients vanishes

$$(S \sin^2\theta + P \cos^2\theta)n^4 + [(RL \sin^2\theta + SP(1 + \cos^2\theta)]n^2 + PRL = 0 . \tag{2.31}$$

Eq. (2.31) is biquadratic in n and is solved for n^2

$$n^2 = \frac{RL \sin^2\theta + SP(1 + cos^2\theta) \pm \sqrt{(RL - PS)^2 \sin^4\theta + 4P^2D^2 \cos^2\theta}}{2(S \sin^2\theta + P \cos^2\theta)} . \tag{2.32}$$

The most interesting features of the solution are resonances and cut-offs.

- *Resonances* are characterised by a phase velocity going to zero ($v_p = \omega/k \to 0$) which is equivalent to the index of refraction $n = kc/\omega$ going to infinity ($n \to \infty$). The wave energy is absorbed by the plasma at resonance points. Resonances can be used for plasma heating. The cold plasma approximation is no longer valid at resonance points, but the electrostatic approximation can be used instead.

- *Cut-offs* are defined by the index of refraction going to zero ($n \to 0$). At these cut-off points, the wavelength goes to infinity and the waves are reflected. Cut-off points can be used for plasma density measurements.

From Eq. (2.32) the general resonance condition can be found by setting the denominator to zero:

$$2(S \sin^2\theta + P \cos^2\theta) = 0 \quad \Leftrightarrow \quad \tan^2\theta = -\frac{P}{S} . \tag{2.33}$$

The general cut-off condition in turn can be seen from Eq. (2.31) by setting $n = 0$:

$$PRL = 0 . \tag{2.34}$$

If the dispersion relation is used to make statements about waves travelling into a certain direction, it is more suitable to express (2.31) in terms of the propagation angle θ. After lengthy but straightforward algebraic manipulation one obtains

$$\tan^2\theta = \frac{P(n^2 - R)(n^2 - L)}{(Sn^2 - RL)(n^2 - P)} . \tag{2.35}$$

With Eqs. (2.33), (2.34) and (2.35) the necessary equations to study waves in the cold and small amplitude limit are completed. From Eq. (2.35) the two special cases of perpendicular ($\theta = \pi/2$) and parallel ($\theta = 0$) wave propagation are easily investigated.

2.3 Plasma Waves in a Cold and Unbounded Plasma

2.3.1 Perpendicular Propagation ($k \perp B_0$, $\theta = \pi/2$)

Within this work, waves propagating perpendicular to the direction of the magnetic field are not investigated experimentally. For completeness, however, perpendicular propagating waves are introduced in brief. A more detailed analysis can be found in textbooks on plasma waves, e.g. Swanson [1989] or Stix [1992]. For perpendicular wave propagation, in which case the denominator of Eq. (2.35) must vanish, there are two possibilities:

1. Ordinary waves: $(n^2 - P) = 0$
   The dispersion relation for the O-mode wave reads

$$k^2c^2 = \omega^2 - \sum_s \omega_{ps}^2 \,. \tag{2.36}$$

   The wave propagation is not affected by the magnetic field as the electric field vector is parallel to the axial magnetic field ($\boldsymbol{E_1} \| \boldsymbol{B_0}$). The dispersion, plotted dashed on the left-hand side of Fig. 2.2, has real solutions (the wave propagates) above the cut-off $\omega > \omega_{pe}$. As the dispersion depends on the plasma density only, O-waves can be used for plasma diagnostics, e.g. reflectometry and interferometry

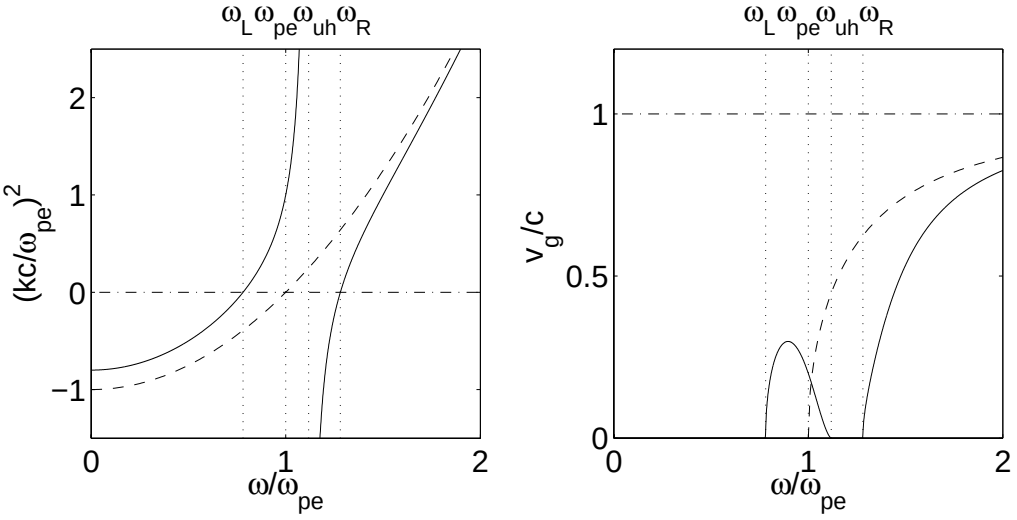

Figure 2.2: Normalised dispersion relation $k(\omega)$ and group velocity $v_g(\omega)$ of the X-wave (solid line) and the O-wave (dashed line). Only electrons are taken into account and $\omega_{ce} = \omega_{pe}/2$.

[Hutchinson, 1987; Wesson, 1997; Hartfuß, 1998]. The group velocity of the O-mode wave increases monotonically up to the speed of light.

2. Extraordinary waves: $(Sn^2 - RL) = 0$
   The dispersion of the X-mode wave is more complicated as neither the resonances nor the cut-offs can be seen straightforward

$$\frac{k^2 c^2}{\omega^2} = \frac{\left(1 - \sum_s \frac{\omega_{ps}^2}{\omega(\omega + \varepsilon_s \omega_{cs})}\right)\left(1 - \sum_s \frac{\omega_{ps}^2}{\omega(\omega - \varepsilon_s \omega_{cs})}\right)}{1 - \sum_s \frac{\omega_{ps}^2}{\omega^2 - \omega_{ce}^2}}\,. \tag{2.37}$$

   Fig. 2.2 shows the high frequency approximation (static ion background) of the X-mode wave (solid lines). It propagates (has real solutions) in the two frequency regimes $\omega_L < \omega < \omega_{uh}$ and $\omega > \omega_R$. The two cut-off frequencies are defined by

$$\omega_{L,R} = \left[\left(\frac{\omega_{ci} + \omega_{ce}}{2}\right)^2 + \omega_{pe}^2 + \omega_{pi}^2\right]^{1/2} \pm \frac{\omega_{ci} - \omega_{ce}}{2}\,, \tag{2.38}$$

   where the plus sign is attributed to ω_L and the minus sign to ω_R, respectively. The X-wave resonates at the upper and the lower hybrid frequency: $\omega_{uh}^2 = \omega_{ce}^2 + \omega_{pe}^2$ and $\omega_{lh}^{-2} = (\omega_{ce}\omega_{ci})^{-1} + (\omega_{pi}^2 + \omega_{ci}^2)^{-1}$. They are called hybrid frequencies, because the wave resonates with a hybrid motion of the electrons and ions (ω_{lh}) and the hybrid electron motion determined by density and magnetic field (ω_{uh}). The lower hybrid resonance cannot be seen in Fig. 2.2 as it does not appear in the high frequency approximation. The X-mode wave is used for plasma diagnostics at the cut-off frequencies [Wesson, 1997] and for plasma heating at the resonance frequencies [Schumacher, 1993; Pinsker, 2001], predominantly in hot magnetically confined plasma devices. Close to the lower hybrid frequency, the X-wave becomes mainly electrostatic ($k_\perp \to \infty$) [Swanson, 1989; Stix, 1965] and transfers its energy via Landau damping mainly to the electrons [Schumacher, 1993; Pinsker, 2001].

2.3.2 Parallel Propagation ($k \| B_0,\ \theta = 0$)

For parallel wave propagation, in which case the numerator of Eq. (2.35) has to vanish, there are three possible solutions:

1. Plasma oscillation: $P = 0$
   This is the simplest plasma motion. Combined with Eq. (2.21) this reads

$$\omega^2 = \sum_s \omega_{ps}^2. \tag{2.39}$$

   This degenerate case is not a propagating wave as the group velocity is zero for

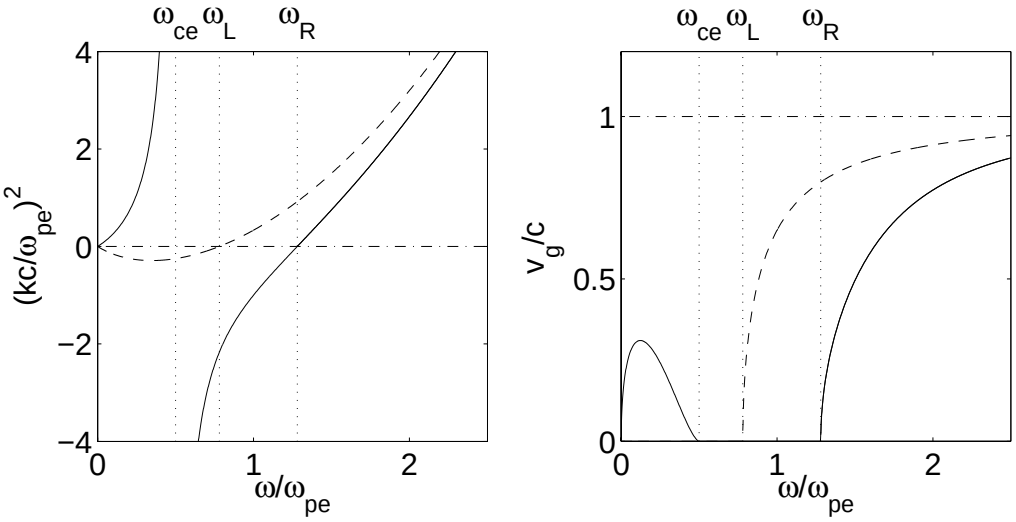

Figure 2.3: Normalised dispersion relation $k(\omega)$ and group velocity $v_g(\omega)$ of the R-wave (solid line) and the L-wave (dashed line). Only electrons are taken into account and $\omega_{ce} = \omega_{pe}/2$.

all frequencies. It represents an oscillation at the plasma frequency. Usually, this frequency is the electron plasma frequency ω_{pe} as this term is by far the largest in the sum ($\omega_{pe} \gg \omega_{pi}$).

2. R-waves: $(n^2 - R) = 0$
   The dispersion relation resulting from this root is

$$k^2c^2 = \omega^2 - \sum_s \frac{\omega\omega_{ps}^2}{\omega + \varepsilon_s\omega_{cs}}. \tag{2.40}$$

   There is one resonance at the electron cyclotron frequency ω_{ce}. This wave is right-hand circular polarised and thus couples to the electron gyration at ω_{ce}. The dispersion and the group velocity are plotted in Fig. 2.3 (solid line), where, again, only the electron motion with a static ion background is assumed. There is a cut-off at ω_R, but in contrast to the O-mode and the X-mode, there is as well a propagating low frequency wave ($\omega < \omega_{ce}$). This part of the R-wave is the only electromagnetic wave mode that propagates at low frequencies. It is called a 'whistler wave' and will be treated in more detail in Sec. 2.3.3.

3. L-waves: $(n^2 - L) = 0$
   The dispersion relation for the L-wave has only one different sign in the denominator compared to Eq. (2.40), but the consequences are much more far reaching

$$k^2c^2 = \omega^2 - \sum_s \frac{\omega\omega_{ps}^2}{\omega - \varepsilon_s\omega_{cs}}. \tag{2.41}$$

   The resonances are now at the cyclotron frequencies of the positive ion species in

the plasma. The wave is left-hand circular polarised and couples to the ion gyration. Fig. 2.3 (dashed line) shows this dispersion relation for an electron plasma alone (high frequency approximation). Obviously, there is no resonance but a wave cut-off at ω_L. For frequencies well above the ion cyclotron frequency, the magnetic field has no influence on the ion motion. The more interesting case of low frequency L-waves, called 'ion whistler waves', is treated for a single and a two component ion species plasma in Sec. 2.3.4.

2.3.3 R-Waves at Low Frequencies: Whistler waves

The R-wave dispersion (2.40) for parallel propagation simplifies at small frequencies $\omega_{ci} \ll \omega \ll \omega_{ce}, \omega_{pe}$ (static ion background) to

$$k^2 c^2 = \frac{\omega \omega_{pe}^2}{\omega_{ce}}\,, \tag{2.42}$$

the so-called whistler wave dispersion (see the low frequency part of the R-wave in Fig. 2.3) . The group velocity

$$v_g = \frac{\partial \omega}{\partial k} = \frac{2c}{\omega_{pe}} \sqrt{\omega \omega_{ce}} \tag{2.43}$$

increases monotonically with increasing frequency up to the approximate limit $\omega \approx \omega_{ce}/4$ [Yeh and Liu, 1972]. That means, high frequency signals propagate faster than those with lower frequency. An initially broadband signal thus disperses along its path of propagation with high frequencies arriving first. A schematic representation of such a dispersed signal is shown in Fig. 2.4. A broadband signal can be initiated from a short impulse like a lightning as the Fourier transform of a pulse, e.g. a delta peak, is a white noise spectrum with constant amplitude for all frequencies:

$$\hat{\Phi}_\delta(\omega) = \frac{1}{2\pi} \int e^{\mathrm{i}\omega t} \delta(T_0) dt = 1\,. \tag{2.44}$$

These sounds of declining tones were first heard at the end of the 19th century on telephone lines [Preece, 1894]. Barkhausen [1919] was the first to link these observations to

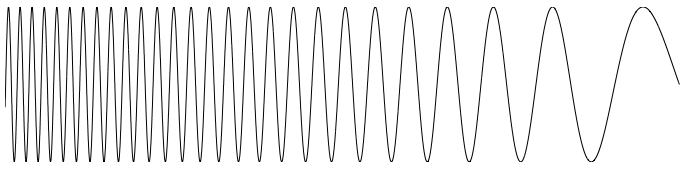

Figure 2.4: Schematic drawing of a dispersed whistler wave signal with high frequencies arriving first.

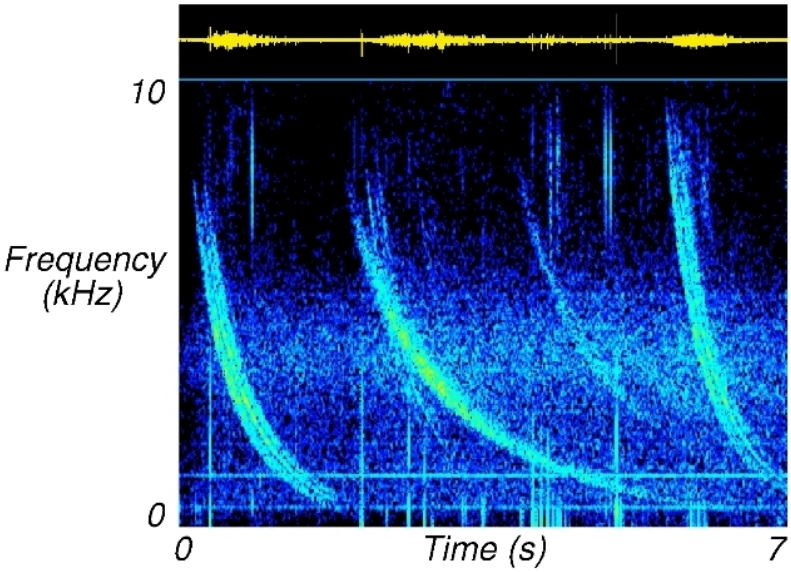

Figure 2.5: Example ionospheric whistler observation. Shown are the signal amplitude (top) and the spectrogram (bottom). Taken from http://www-pw.physics.uiowa.edu/mcgreevy/.

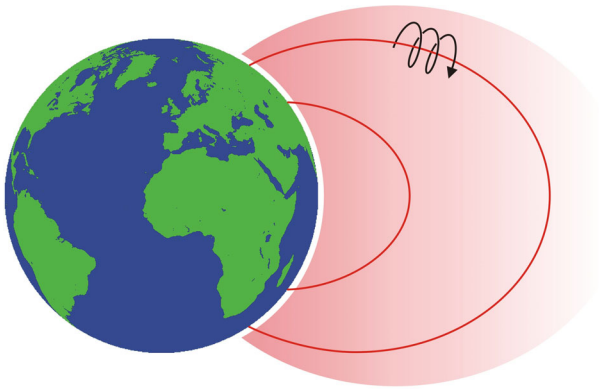

Figure 2.6: Schematic of the whistler wave propagation along the field lines of the earth magnetic dipole.

atmospheric phenomena. Later, Barkhausen [1930] and Eckersley [1935] related this to the dispersive broadening of a white noise spectrum initiated from a lightning stroke in the ionosphere. A sample spectrogram (temporal evolution of the frequency spectrum) of whistler waves in the ionosphere is shown in Fig. 2.5. Clearly visible are the declining tones. The four events are initiated by a lightning. They are triggered at different points and thus propagate along different paths (magnetic field lines, cf. Fig. 2.6). Depending on the length of the path, the magnetic field strength and the plasma density along the path, the signal dispersion is different. According to this, the received signals show differences in the spectrogram with respect to their duration and slope.

The dispersion relation and group velocity of whistler waves are shown in the low frequency part of Fig. 2.3. Dispersion diagrams are usually plotted as the normalised wave vector kc/ω_{pe} vs normalised frequency ω/ω_{pe}. In laboratory experiments, however, the

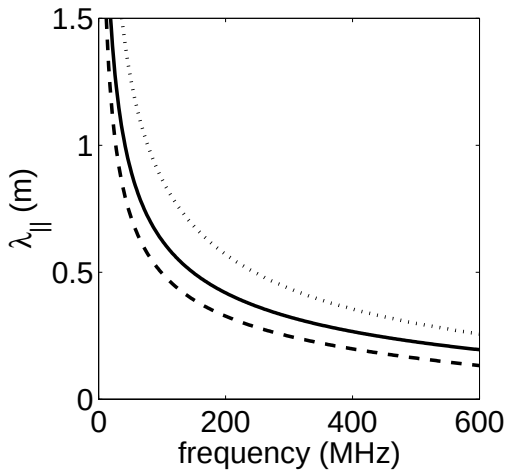

Figure 2.7: Whistler wave dispersion (2.42) plotted for physical quantities as parallel wavelength $\lambda_{\|}$ vs frequency f. The ambient magnetic field and the plasma density are: $B_0 = 56\,\mathrm{mT}$, $n = 4 \cdot 10^{16}\,\mathrm{m}^{-3}$ (solid line), $B_0 = 56\,\mathrm{mT}$, $n = 2 \cdot 10^{16}\,\mathrm{m}^{-3}$ (dotted line), and $B_0 = 36\,\mathrm{mT}$, $n = 4 \cdot 10^{16}\,\mathrm{m}^{-3}$ (dashed line).

observed quantities are wavelength $\lambda_{\|} = k_{\|}/2\pi$ parallel to the ambient magnetic field and frequency $f = \omega/2\pi$. Fig. 2.7 shows the whistler wave dispersion branch as determined by Eq. (2.42) with these quantities for three different sets of plasma conditions: $B_0 = 56\,\mathrm{mT}$, $n = 4 \cdot 10^{16}\,\mathrm{m}^{-3}$ (solid line), $B_0 = 56\,\mathrm{mT}$, $n = 2 \cdot 10^{16}\,\mathrm{m}^{-3}$ (dotted line), and $B_0 = 36\,\mathrm{mT}$, $n = 4 \cdot 10^{16}\,\mathrm{m}^{-3}$ (dashed line). The dispersion is sensitive to both parameters, the ambient magnetic field B_0 and the plasma density n. One can see from Fig. 2.7 and Eq. (2.42) that the wavelength at a given frequency decreases for decreasing magnetic field and for increasing plasma density. Moreover, the wavelength depends on the frequency as well, it decreases monotonically with increasing frequency. The nomenclature in 'space research' unfortunately deviates from that of 'laboratory research'. I will follow the latter one and call low-frequency R-waves 'electron whistler waves' or simply 'whistler waves' and the low-frequency L-waves 'ion whistler waves'. In the space community, a whistler wave is only defined as 'an electromagnetic wave excited by lightning and dispersed while propagating through the ionosphere or the magnetosphere' [Stenzel, 1999]. All other phenomena are classified by their appearance on spectrograms or their sound as hiss, roar, chorus, risers, hooks, etc. [Helliwell, 1965].

2.3.4 L-Waves at Low Frequencies: Ion Whistler Waves

The L-wave dispersion in the low frequency limit $\omega_{ci} \sim \omega \ll \omega_{ce}$ differs qualitatively from its high frequency approximation. One resonance per ion species (that means per charge to mass ratio Z/m_i) arises. Fig. 2.8 shows the dispersion relation and the group velocity of the L-wave (dashed lines) with one single charged argon ion species. There is a resonance at the ion cyclotron frequency $\omega_{c,Ar}$. The group velocity of the L-wave

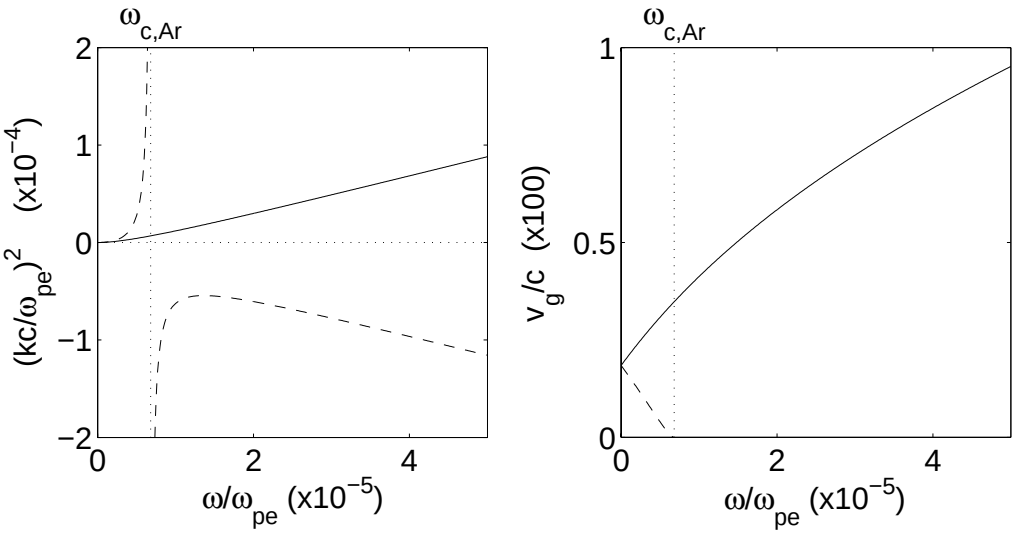

Figure 2.8: Normalised dispersion relation $k(\omega)$ and group velocity $v_g(\omega)$ of the R-wave [solid line, Eq. (2.42)] and the L-wave [dashed line, Eq. (2.41)] at low frequencies in a pure argon plasma ($\omega_{ce} = \omega_{pe}/2$). The vertical dotted line indicates the cyclotron frequency of argon $\omega_{c,Ar}$.

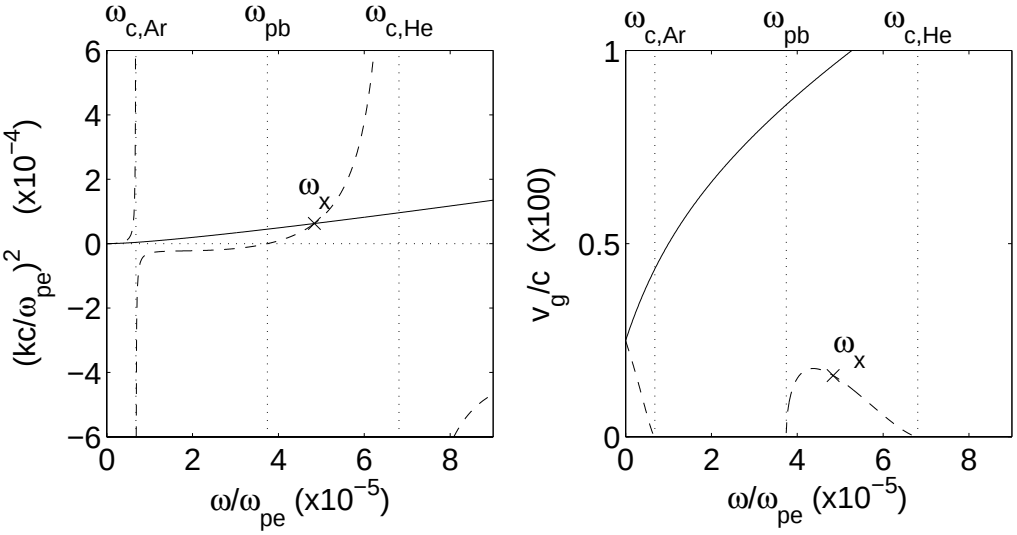

Figure 2.9: Normalised dispersion relation $k(\omega)$ and group velocity ($v_g(\omega)$ of the R-wave (solid line) and the L-wave (dashed line). Now there are two ion species (50% Helium and 50% Argon) and again $\omega_{ce} = \omega_{pe}/2$. The vertical dotted lines indicates the cyclotron frequency of argon $\omega_{c,Ar}$ and helium $\omega_{c,He}$ as well as the pass-band frequency ω_{pb}.

decreases monotonically up to the resonance. Above this limit, no low frequency L-wave can propagate. The ionospheric plasma mostly consists of more than one ion species. The L-wave dispersion changes dramatically if a second ion species is added. The L-wave has now two resonances, one at each ion cyclotron frequency. In Fig. 2.9 the dispersion relation and the group velocity for a 50% Argon–50% Helium plasma are shown together with the R-wave dispersion (2.42). There are two regions of wave propagation, one for frequencies $\omega < \omega_{c,Ar}$ and one for frequencies in a pass-band with $\omega_{pb} < \omega < \omega_{c,He}$, where $\omega_{pb} = \alpha_{Ar}\omega_{c,Ar} + \alpha_{He}\omega_{c,He}$. The relative ion densities of the two species are defined by $\alpha_{Ar} = n_{Ar}/n$ and $\alpha_{He} = n_{He}/n$ such that $\alpha_{Ar} + \alpha_{He} = 1$. The dispersion relation of the R-wave and the L-wave intersect at the 'crossover frequency' $\omega_\times$. From Eqs. (2.40) and (2.41), the crossover frequency can be calculated to $\omega_\times^2 = \alpha_{Ar}\omega_{c,Ar}^2 + \alpha_{He}\omega_{c,He}^2$. For frequencies above $\omega_\times$, the group velocity of the L-wave decreases, whereas the group velocity of the R-wave is still monotonically increasing. At the crossover frequency in such a multicomponent plasma, mode coupling can occur between the R-mode and L-mode wave [Smith and Brice, 1964; Gurnett et al., 1965; Yeh and Liu, 1972; Leer et al., 1978].

In a spectrogram recorded at a distant point away from the excitation by a lightning pulse, the R-wave would still appear as the well-known whistler, but the L-wave, excited from mode coupling at the crossover frequency, would occur as a signal with the frequency $\omega_\times$ arriving first. From its appearance in a spectrogram, such as Fig. 2.10, this is called 'nose whistler'. These type of spectrograms are typical for an ion whistler and have been detected in satellite data in the ionosphere [Ruud, 2000]. Clearly visible in Fig. 2.10 are the common trace of a whistler wave ($t > 0.15\,\mathrm{s}$) and the ion whistler wave ($t > 0.35\,\mathrm{s}$), both emphasised by white dashed lines. The measured ion cyclotron frequency

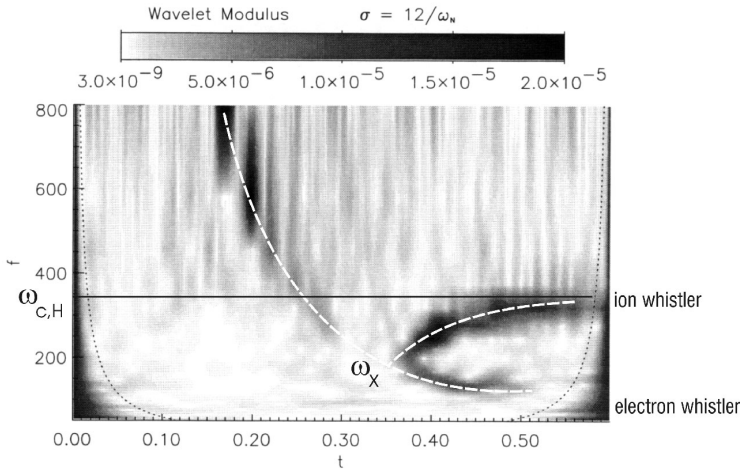

Figure 2.10: Example spectrogram of a whistler measurement from the Freja-satellite showing the typical trace of an electron whistler and an ion whistler waves (white dashed lines) with a nose frequency of $\omega_\times = 195\,\mathrm{kHz}$. The horizontal solid line indicates the cyclotron frequency of hydrogen $\omega_{c,H} = 375\,\mathrm{kHz}$. Adapted from Ruud [2000].

$\omega_{c,H} = 375\,\mathrm{kHz}$ corresponds well to the expected value calculated from the magnetic field strength. The crossover frequency of $\omega_\times = 195\,\mathrm{kHz}$ was found between $\omega_{c,He}$ and $\omega_{c,H}$. As the crossover frequency varies with the ion species ratio, the spectrograms have been used to determine the ion composition of the plasma at the detection point [McEwen and Barrington, 1968; Ruud, 2000]. These compositions partially deviate [Ruud, 2000] from models that are based on measurements with different techniques. Confer e.g. the 'International Reference Ionosphere' [Bilitza, 1997].

2.3.5 Propagation at Arbitrary Angles

R-waves in unbounded plasmas do not necessarily have to propagate purely parallel to the ambient magnetic field. In this section, the R-wave propagation oblique to the ambient magnetic field is treated. The angle between the wave vector $\boldsymbol{k}$ and the ambient magnetic field $\boldsymbol{B_0}$ is called θ (cf. geometry in Fig. 2.1). Taking in Eq. (2.35) only the electron motion into account, the dispersion reads to be similar to Eq. (2.40)

$$k^2c^2 = \omega^2 - \frac{\omega\omega_{pe}^2}{\omega - \omega_{ce}\cos\theta}\,. \tag{2.45}$$

The total wave vector is the sum of the perpendicular and the parallel components $k^2 = k_\perp^2 + k_\parallel^2$ and in contrast to Eq. (2.42) this formula holds true not only in the low frequency limit. For parallel propagation ($\theta = 0$), the wave resonance frequency is again ω_{ce}, as previously derived for parallel R-wave propagation and $k = k_\parallel$. For increasing propagation angle, the resonance frequency decreases up to an angle $\theta_{\mathrm{res}} = \cos^{-1}(\omega/\omega_{ce})$. Above θ_{res}, no propagation is possible. This means, the R-wave propagation is restricted to a

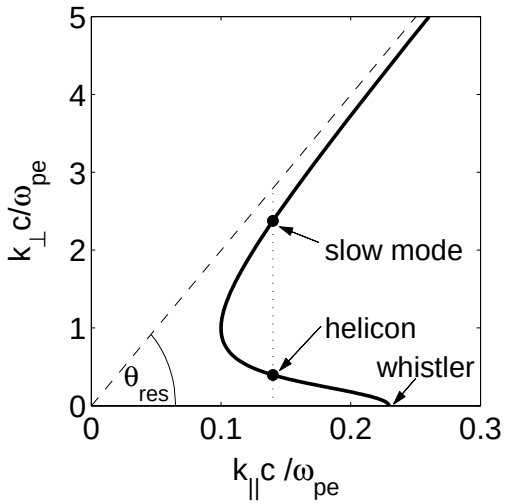

Figure 2.11: R-wave dispersion (2.45) plotted in a polar plot for normalised $k_\perp$ vs $k_\parallel$ (solid line). The resonance cone limit for the maximum angle of propagation θ_{res} is plotted dashed. The three approximated cases, the whistler, the helicon, and the slow mode wave are marked. Note the different scales of the axis.

cone along the magnetic field with the angle $\theta_{\rm res}$, called the 'whistler resonance cone' [Kuehl, 1962; Fisher and Gould, 1969]. For whistler waves, the maximum angle of the group velocity is $19.5°$ [Swanson, 1989] and thus the energy flow is restricted within that cone. This means that the whistler wave is strongly guided by the magnetic field and whistler waves propagating in the earth's magnetosphere can often be found at conjugate magnetic points away from their excitation. Furthermore, it can be shown that the wave is purely electromagnetic for parallel propagation and becomes purely electrostatic at the resonance cone angle. At intermediate angles, the wave shows both characteristics [Swanson, 1989]. The resonance cone can be seen in the diagram if the wave vector is plotted in polar representation as normalised $k_\perp c/\omega_{pe}$ vs $k_\parallel c/\omega_{pe}$ at a given ω/ω_{pe}. Fig. 2.11 shows such a normalised graph for $\omega_{pe} = 2\omega_{ce} = 1$ and $\omega = 0.01$. The whistler wave is found for parallel propagation ($k_\perp = 0$). The resonance cone angle $\theta_{\rm res}$ can as well be seen from the plot to be the maximum permitted angle. The two marked points are explained below.

2.4 Whistler Waves in a Bounded Plasma

Laboratory plasmas are necessarily always bounded and mostly non-uniform. Significant changes of the propagation behaviour of waves are expected if compared to predictions of unbounded plasma theory that deals with plane waves in infinite and homogeneous plasmas (cf. Sec. 2.3.2). Low frequency whistler waves in bounded geometry, the helicon mode, is introduced in Sec. 2.4.1. A more rigourous treatment starting with a wave in a cylindrical plasma-filled waveguide is presented in Sec. 2.4.2, following the work of Uhm et al. [1988]. As these bounded waves are not only identified by the axial wave number $k_\parallel$ but also by their radial modenumber $k_\perp$, the radial wave mode structure is considered in Sec. 2.4.3. The waves are treated in a plane wave ansatz in cylindrical geometry

$$A(r)\exp[i(k_\parallel z - m\phi - \omega t)]\,. \tag{2.46}$$

2.4.1 Helicon Waves

Helicon waves are R-waves at frequencies in between the ion and electron cyclotron frequencies $\omega_{ci} \ll \omega \ll \omega_{ce}$ in a radially bounded plasma. Helicon waves were investigated first in the 1960's in metal solids [Aigrain, 1960; Legéndy, 1965] and the gaseous plasma of an rf discharge [Lehane and Thonemann, 1965]. Helicon waves became popular in laboratory experiments and industrial plasma engineering since the mid 1980's, when Boswell [1984b] discovered that helicon wave sources are surprisingly efficient in plasma production. The dispersion relation of helicon waves can be derived from that of an R-wave Eq. (2.45) with oblique propagation in the low frequency limit $\omega_{ci} \ll \omega \ll \omega_{ce}$ with wave number $k_\perp$ and thus, the wave vector is $k^2 = k_\perp^2 + k_\parallel^2$.

For the discussion of the heating mechanism, it is helpful to consider wave damping.

The collisional damping is expressed in the dispersion relation as an imaginary collision frequency $\mathrm{i}\nu$, including electron collisions with both ions and neutrals. Substituting ω by $\omega + \mathrm{i}\nu$, the helicon wave dispersion reads

$$k^2c^2 = \frac{\omega\omega_{pe}^2}{\omega_{ce}\cos\theta - \omega - \mathrm{i}\nu}\,. \tag{2.47}$$

Again, θ is the angle between the wave vector $\boldsymbol{k}$ and the ambient axial magnetic field (cf. Fig. 2.1, $\cos\theta = k_\parallel/k$). The conducting boundary of a cylindrical vacuum vessel with radius R_c introduces two boundary conditions for the axial z-components of the electric and magnetic field fluctuations:

$$\delta E_z(R_c) = 0 \quad \text{and} \quad \frac{\partial}{\partial r}\,\delta B_z(R_c) = 0\,. \tag{2.48}$$

In cylindrical geometry with homogeneous plasma density, the resulting eigenfunctions are Bessel functions. A $k_\perp$ has to be chosen such that the solutions vanish at the plasma boundary $r = R_c$

$$J_n(k_\perp R_c) = 0 \quad \rightarrow \quad k_\perp = \gamma_{nm}/R_c\,, \tag{2.49}$$

where γ_{nm} is the m^{th} root of the n^{th} order Bessel function and m represents the poloidal modenumber of the eigenfunction solution. Rearranging Eq. (2.47) for the frequency yields

$$\omega = \omega_{ce}\cos\theta\frac{k^2c^2}{\omega_{pe}^2 + k^2c^2}\left(1 - \mathrm{i}\frac{\nu}{\omega_{ce}\cos\theta}\right)\,. \tag{2.50}$$

Two approximations of Eq. (2.50) can be derived [Boswell, 1984b; Shamrai and Taranov, 1996]. First, for short wave lengths ($k \gg \omega_{pe}/c = \delta_{skin}$), the dispersion Eq. (2.50) simplifies to

$$\omega = \omega_{ce}\frac{k_\parallel}{k} - \mathrm{i}\nu\,. \tag{2.51}$$

These waves are quasi-electrostatic ($n = k_\parallel c/\omega \gg 1$) and strongly damped. In helicon research they are commonly referred to as slow mode waves (phase velocity $\omega/k_\perp \sim v_{th,i}$) or Trivelpiece-Gould modes, since they were first identified by Trivelpiece and Gould [1959] as eigenmodes of an electrostatic wave in a bounded cylinder. This wave can also be derived from Eq. (2.45) in the limit of $\theta \rightarrow \theta_{\mathrm{res}}$ including collisions. Second, in the limit of long wavelengths ($k \ll \omega_{pe}/c$), one obtains helicon waves. From the dispersion relation it is seen that they are much weaker damped

$$\omega = \omega_{ce}\frac{k_\parallel k c^2}{\omega_{pe}^2} - \mathrm{i}\nu\frac{k^2c^2}{\omega_{pe}^2}\,. \tag{2.52}$$

Both approximations can be related to different points in the polar plot Fig. 2.11. For a given $k_\parallel$ (dotted line), two different $k_\perp$ are possible in the dispersion. One for a large $k_\perp$ (slow mode wave) and one for a small $k_\perp$ (helicon wave). The real part of the helicon

dispersion Eq. (2.52) simplifies further to

$$\frac{k_\parallel k}{\omega} = \frac{ne\mu_0}{B_0}\,. \tag{2.53}$$

This equation relates the wave parameters ω, $k_\perp$, and $k_\parallel$ with the plasma parameters n and B_0 [Komori et al., 1991; Chevalier and Chen, 1993]. In Sec. 6.2 this relation is investigated in detail.

2.4.2 Waves in a Waveguide

In the previous section, the introduction of a boundary condition results in a non-zero perpendicular wave number that changes the dispersion of whistler waves substantially. This leads to a satisfying result only under the assumptions of low frequencies ($\omega \ll \omega_{pe}, \omega_{ce}$) and homogeneous plasma density distribution. A more rigourous treatment of electromagnetic waves in a plasma filled waveguide with axial magnetic field was developed by Uhm et al. [1988]. From the linearised equations of motion and the continuity equation, self-consistently coupled to Maxwells' equations, a set of two coupled eigenvalue equations is obtained, which describes the wave's electric and magnetic fields $\delta E_z(r)$ and $\delta B_z(r)$

$$\nabla_r^2 \delta E_z(r) + \left(T^2 - \frac{m^2}{r^2}\right)\delta E_z(r) + \mathrm{i}U\nabla_r^2\delta B_z(r) = 0\,, \tag{2.54}$$

$$\nabla_r^2 \delta B_z(r) + \left(S^2 - \frac{m^2}{r^2}\right)\delta B_z(r) - \mathrm{i}V\nabla_r^2\delta E_z(r) = 0\,, \tag{2.55}$$

where m is the poloidal modenumber and $\nabla_r^2 = d^2/dr^2 + r^{-1}d/dr$ the radial Laplace operator in cylindrical coordinates. T^2, S^2, U, and V are defined as follows:

$$T^2(r) = \frac{p^2\left(1 - \sum_{j=e,i}\omega_{pj}^2/\omega^2\right)}{1 - q^2(1 - \alpha/(\alpha^2 - \beta^2))}\,, \tag{2.56}$$

$$S^2(r) = \frac{p^2}{\alpha/(\alpha^2 - \beta^2)}\,, \tag{2.57}$$

$$U(r) = \frac{kc\beta/(\alpha^2 - \beta^2)}{\omega[1 - q^2(1 - \alpha/(\alpha^2 - \beta^2))]}\,, \tag{2.58}$$

$$V(r) = kc\beta/\omega\alpha \tag{2.59}$$

with

$$\alpha = 1 - \frac{\omega^2}{c^2p^2}\sum_{j=e,i}\frac{\omega_{pj}^2}{\omega^2 - \omega_{cj}^2}\,, \tag{2.60}$$

$$\beta = -\frac{\omega}{c^2p^2}\sum_{j=e,i}\frac{\omega_{pj}^2}{\omega^2 - \omega_{cj}^2}\varepsilon_j\omega_{cj}\,, \tag{2.61}$$

with $p^2 = \omega^2/c^2 - k^2$ and $q = kc/\omega$. The dispersion relation of the wave is obtained by solving for the two eigenvalues of the two ordinary differential Eqs. (2.54) and (2.55). The dispersion relation $k(\omega)$ is contained implicitly in the parameters T, S, U, and V. Mathematically speaking, this requires solving a non-linear eigenvalue equation of a fourth order ordinary differential equation. Numerically this is quite demanding but can in principle be done using the Ricatti-shooting-method [Scott, 1973; Davey, 1977]. Results from a numerical study with a code adapted from Kleiber [1996] are discussed in Chap. 7. An algebraic expression for the dispersion is only found for the simple case of a flat-top density distribution

$$n_{e,i}^0 = \begin{cases} \hat{n}_{e,i} = \text{const.} & 0 \le r \le R_p\,, \\ 0 & R_p < r \le R_c\,, \end{cases} \tag{2.62}$$

with R_p the plasma radius and R_c the radius of a conducting boundary. The parameters $\omega_p(r)$, $T(r)$, and $S(r)$ are similarly expressed as $\hat{\omega}_p$, $\hat{T}$, and $\hat{S}$ for $r \le R_p$ and as the vacuum terms for $R_p < r \le R_c$. The conducting vessel sets the boundary conditions of Eq. (2.48) and together with the continuity condition at the plasma boundary ($r = R_p$), the dispersion relation finally reads [Uhm et al., 1988]

$$\begin{aligned} &\left[f_m + mq\left((1-\hat{a})\frac{V\xi^2}{\hat{S}^2-\xi^2} - q\hat{b}\right) - \left(1 - q^2(1-\hat{a}) + q\hat{b}V\frac{\xi^2}{\hat{S}^2-\xi^2}\right)\frac{\xi R_p J_m'(\xi R_p)}{J_m(\xi R_p)}\right] \\ &\qquad \times \left(\frac{V\eta^2}{\hat{S}^2-\eta^2}(m\hat{b} - g_m) - mq(1-\hat{a}) + q\hat{b}\frac{\hat{S}^2}{\hat{S}^2-\eta^2}\frac{\eta R_p J_m'(\eta R_p)}{J_m(\eta R_p)}\right) \\ -&\left[f_m + mq\left((1-\hat{a})\frac{V\eta^2}{\hat{S}^2-\eta^2} - q\hat{b}\right) - \left(1 - q^2(1-\hat{a}) + q\hat{b}V\frac{\eta^2}{\hat{S}^2-\eta^2}\right)\frac{\eta R_p J_m'(\eta R_p)}{J_m(\eta R_p)}\right] \\ &\qquad \times \left(\frac{V\xi^2}{\hat{S}^2-\xi^2}(m\hat{b} - g_m) - mq(1-\hat{a}) + q\hat{b}\frac{\hat{S}^2}{\hat{S}^2-\xi^2}\frac{\xi R_p J_m'(\xi R_p)}{J_m(\xi R_p)}\right) = 0\,. \end{aligned} \tag{2.63}$$

Here $\hat{a} = a(r=0)$ and $\hat{b} = b(r=0)$, ξ^2 and η^2 are the independent solutions of X^2 of the biquadratic equation $(X^2 - \hat{T}^2)(X^2 - \hat{S}^2) - UVX^4 = 0$, and the geometrical factors f_m and g_m are defined as

$$f_m(p) = pR_p\frac{N_m(pR_c)J_m'(pR_p) - J_m(pR_c)N_m'(pR_p)}{J_m(pR_p)N_m(pR_c) - J_m(pR_c)N_m(pR_p)}$$

and

$$g_m(p) = pR_p\frac{N_m'(pR_c)J_m'(pR_p) - J_m'(pR_c)N_m'(pR_p)}{N_m'(pR_c)J_m(pR_p) - J_m'(pR_c)N_m(pR_p)}\,.$$

Eq. (2.63) describes the full dispersion for any combination of R_c and R_p and can be used as the starting point for further approximations. For the case of an infinite uniform plasma ($R_c = R_p = \infty$), the whistler wave Eq. (2.42) is recovered. A low frequency approximation is obtained ($\omega \ll \omega_{ce}, \omega \ll kc$) similar to the helicon wave dispersion (2.52). For a

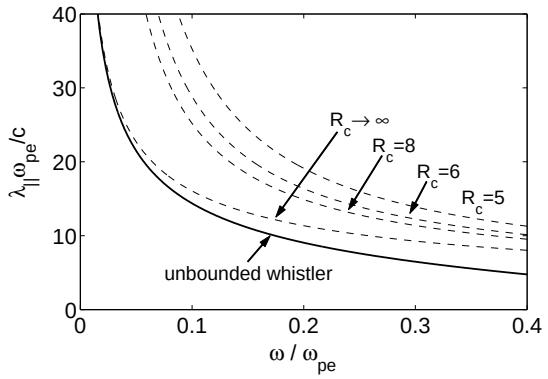

Figure 2.12: Dispersion relation (2.64) is plotted for different radii R_c (dashed lines) together with the dispersion Eq. (2.40) for unbounded plasma geometry [solid line].

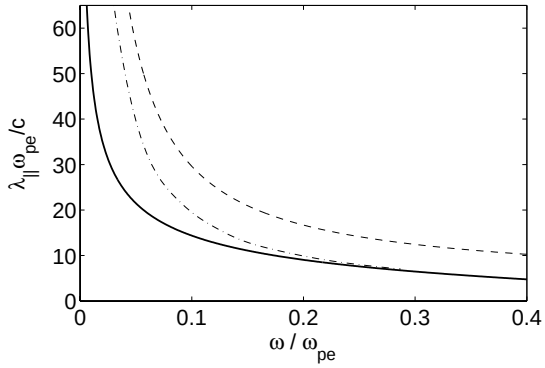

Figure 2.13: Comparison of different theoretical dispersion curves. Shown are the dispersion for unbounded plasma geometry [solid, Eq. (2.40)], the approximation Eq. (2.64) [dashed], and the dispersion Eq. (2.63) [dash-dotted].

completely filled waveguide $R_p = R_c$ it reads

$$\omega = \frac{\omega_{ce} kc/\hat{\omega}_{pe}}{(K_c^2 - 1)^{1/2}} \left(\left[K_c \frac{kc}{\hat{\omega}_{pe}} \right]^2 + 1 \right)^{1/2} . \tag{2.64}$$

In contrast to the simple helicon wave dispersion, two points are noteworthy. First, the parameter $K_c^2 = \hat{\omega}_{pe}^2 R_c^2 / \gamma_{0n}^2 c^2$ needs to be larger than unity for propagating waves (γ_{m0} is again the m^{th} root of the zero order Bessel function). This means that a wave needs a certain minimum density to propagate in a plasma of a certain radius R_c. Second, the influence of the geometry on the wave propagation is clearly be seen from the factor $(K_c kc/\hat{\omega}_{pe})^2$. The low frequency approximation Eq. (2.64) is plotted for different plasma radii R_c in Fig. 2.12 (dashed lines) together with the unbounded whistler wave Eq. (2.40) (solid line). For a given frequency, the parallel wavelength $\lambda_\parallel$ increases for decreasing plasma radius R_c. In the limit of infinite plasma radius $R_c \to \infty$, the dispersion of whistler waves in unbounded plasma geometry is recovered at low frequencies. The low-frequency approximation Eq. (2.64) does not give the correct wavelengths at higher frequencies but overestimates them. Fig. 2.13 shows the full dispersion of Eq. (2.63) for an $m = 0$ mode at $R_c = 0.2\,\text{m}$ (dash-dotted line). Again, for a given frequency, the wavelength increases with decreasing plasma radius. For low frequencies, the limit of Eq. 2.64 (dashed line) is approached. In the opposite limit for high frequencies, corresponding to small wavelengths, the limit of the whistler wave dispersion Eq. 2.40 in unbounded plasma geometry (solid line) is approached.

2.4.3 Wave Field Structure

In order to gain a physical picture of helicon waves or to prove their presence in experiments, it is helpful to understand their magnetic and electric wave field structure. Starting from Maxwells' equations and neglecting again the displacement current (low frequency approximation), the basic wave equation is derived as [Chen, 1991]

$$\nabla^2 \boldsymbol{B} + k^2 \boldsymbol{B} = 0\,. \tag{2.65}$$

The wave number k reads to be

$$k = \frac{k_\parallel}{\omega}\frac{B_0}{e\mu_0 n}\,. \tag{2.66}$$

In general, the plasma density is a function of the radius $n(r)$, but the analysis is simplified with the assumption of radially constant plasma density. Numerical and analytic calculations for a non-homogeneous plasma density have been made for special profiles [Chen et al., 1994; Sudit and Chen, 1994a; Cho and Kwak, 1997]. Using the Laplacian operator in cylindrical coordinates

$$\nabla^2 = \frac{\partial^2}{\partial r^2} + \frac{1}{r}\frac{\partial}{\partial r} + \frac{1}{r^2}\frac{\partial^2}{\partial \theta^2} + \frac{\partial^2}{\partial z^2} \tag{2.67}$$

gives for the z component of Eq. (2.65)

$$B_z'' + \frac{1}{r}B_z' + \left(k_\perp^2 - \frac{m^2}{r^2}\right) B_z = 0, \tag{2.68}$$

where $k_\perp^2 = k^2 - k_\parallel^2$ is the wave number perpendicular to $\boldsymbol{B_0}$. This is Bessel's differential equation of order m. The solution is Bessel's function $J_m(k_\perp r)$. The z-component of the magnetic helicon field is

$$B_z = C J_m(k_\perp r). \tag{2.69}$$

Using the nabla operator in cylindrical coordinates

$$\boldsymbol{\nabla} = \frac{\partial}{\partial r}\hat{\boldsymbol{e}}_r + \frac{1}{r}\frac{\partial}{\theta}\hat{\boldsymbol{e}}_\theta + \frac{\partial}{\partial z}\hat{\boldsymbol{e}}_z \tag{2.70}$$

one can determine the r- and the θ-components of Eq. (2.65)

$$\frac{\mathrm{i}m}{r}B_z - \mathrm{i}k_\parallel B_\theta = kB_r \tag{2.71}$$

$$\mathrm{i}k_\parallel B_r - B_z' = kB_\theta. \tag{2.72}$$

Solving these equations for B_z and B_z' and substituting Eq. (2.69) for B_z yields

$$B_r = \mathrm{i}\frac{C}{k_\perp^2}\left(\frac{m}{r}kJ_m(k_\perp r) - k_\parallel J_m'(k_\perp r)\right) \tag{2.73}$$

$$B_\theta = \frac{C}{k_\perp^2}\left(\frac{m}{r}k_\parallel J_m(k_\perp r) + kJ_m'(k_\perp r)\right). \tag{2.74}$$

Using the recurrence relations for Bessel functions [Abramowitz and Stegun, 1984]:

$$\frac{2m}{k_\perp r} J_m(k_\perp r) = J_{m+1}(k_\perp r) - J_{m-1}(k_\perp r) \tag{2.75}$$

$$\frac{2}{k_\perp}\frac{\partial}{\partial r} J_{m>0}(k_\perp r) = J_{m+1}(k_\perp r) - J_{m-1}(k_\perp r) \tag{2.76}$$

leads to the solutions of the magnetic field of a helicon wave of the form

$$B_r = \mathrm{i}\frac{C}{2k_\perp}[(k+k_\parallel)J_{m-1}(k_\perp r) + (k-k_\parallel)J_{m+1}(k_\perp r)] \tag{2.77}$$

$$B_\theta = -\frac{C}{2k_\perp}[(k+k_\parallel)J_{m-1}(k_\perp r) - (k-k_\parallel)J_{m+1}(k_\perp r)] \tag{2.78}$$

$$B_z = C J_m(k_\perp r). \tag{2.79}$$

Again, the conducting vessel of radius R_c imposes boundary conditions, Eqs. (2.48), and determines thus the perpendicular wave vector $k_\perp$. A plot of the magnetic modestructures in radial direction is shown for mode number $m = 0$ and $m = +1$ in Fig. 2.14 for typical experimental conditions: $B_0 = 50\,\mathrm{mT}$, $f = 13.56\,\mathrm{MHz}$, $k_\parallel = 2\pi/0.15\,\mathrm{m}^{-1}$, and $k_\perp = 3.83/0.05\,\mathrm{m}^{-1}$. A colour-coded plot of the axial magnetic fluctuations in the entire poloidal plane is depicted in Fig. 2.15 for the same experimental conditions. Clearly visible is the great difference between the $m = 1$ mode with a centre minimum (left) and the $m = 0$ mode with a centre maximum (right). Note that there is a principle difference of the modestructure between the previously used cylindrical coordinate system and the cartesian frame used for the measurements. However, both coordinate systems can are related by simple trigonometric formulae and for purely vertical and purely horizontal cuts through the centre, both systems coincide.

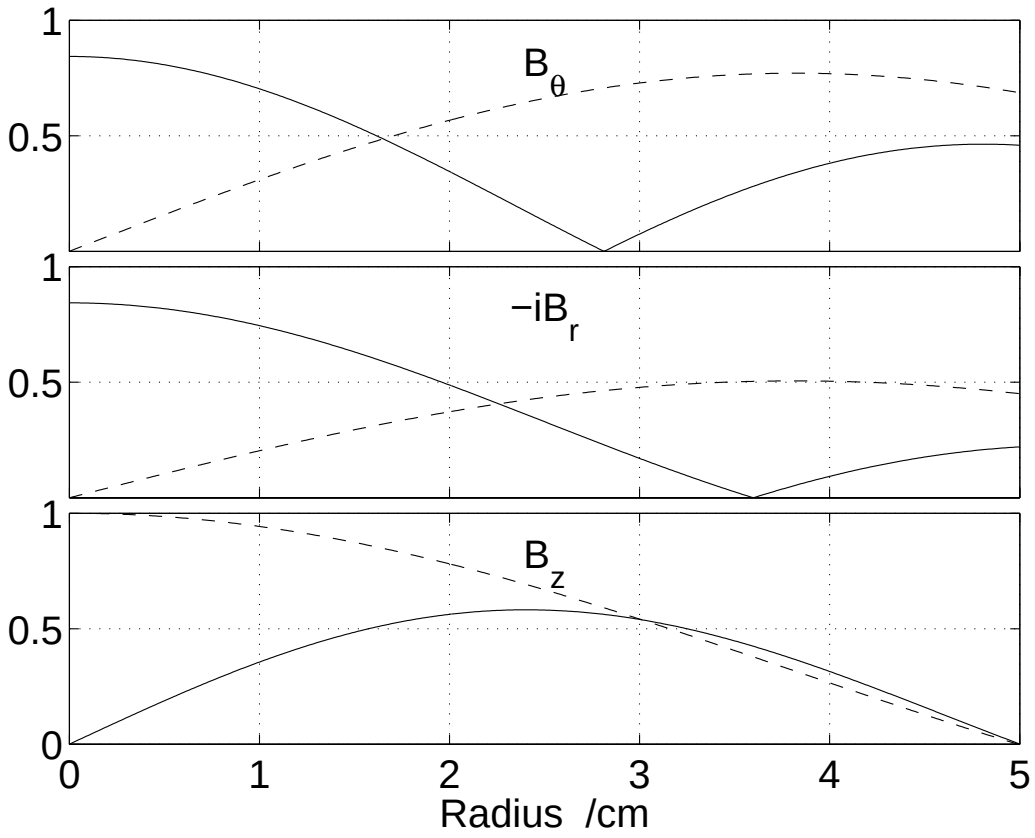

Figure 2.14: Radial profiles of B_z (bottom), B_r (mid) and B_θ (top) calculated for $m = +1$ (solid line) and $m = 0$ (dashed line). The chosen parameters are $B_0 = 50\,\mathrm{mT}$, $f = 13.56\,\mathrm{MHz}$, $k_\parallel = 2\pi/0.15\,\mathrm{m}^{-1}$, and $k_\perp = \gamma_{m0}/0.05\,\mathrm{m}^{-1}$.

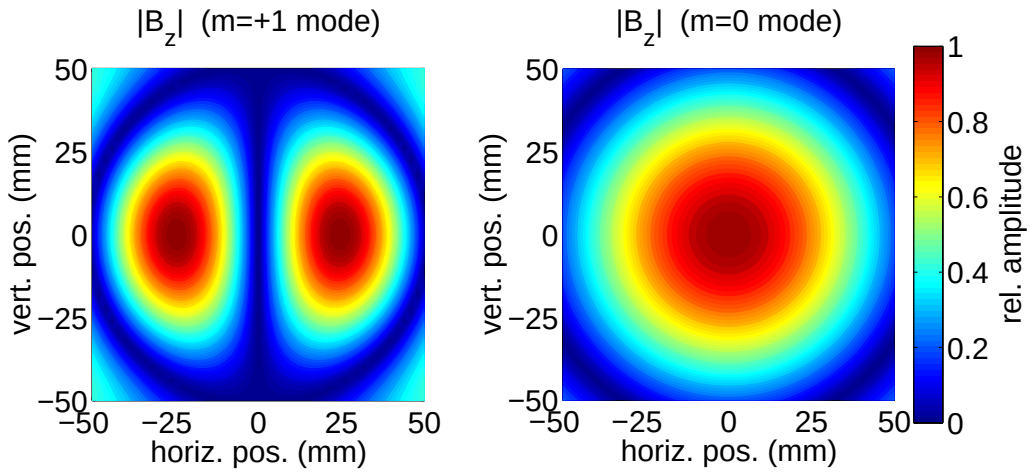

Figure 2.15: Poloidal profile of B_z calculated for an $m = 1$ mode (left) and $m = 0$ mode helicon wave. The parameters are $B_0 = 50\,\mathrm{mT}$, $f = 13.56\,\mathrm{MHz}$, $k_\parallel = 2\pi/0.15\,\mathrm{m}^{-1}$, and $k_\perp = \gamma_{m0}/0.05\,\mathrm{m}^{-1}$

3

RF Discharges

The main plasma source used at the VINETA device is a conventional helicon source. It is made of an rf driven $m = +1$ antenna of length $l = 300$ mm that is placed around a cylindrical glass vacuum extension with 100 mm diameter (see Figs. 4.2 and 4.21). Depending on the input rf power, the discharge operates in three qualitatively different modes, the capacitive, the inductive, and the helicon wave sustained mode. The first two discharge modes are fairly well understood. In Secs. 3.1 and 3.2 a brief introduction is given, following the modelling of Lieberman [1988]; Lieberman and Lichtenberg [1994], and Eckert [1986]. Although helicon sources are used since the mid 1980's, the physical principle of their surprisingly efficient discharge mechanism in the third mode, the helicon wave sustained mode, is still a scientific case. With the theoretical framework of the previous chapter on (bounded) electromagnetic plasma waves in mind, this chapter reviews the literature on helicon sources and discusses the most promising discharge models (Sec. 3.3).

3.1 Capacitive Discharges

A simple and widely used rf source is the capacitive discharge. Its easiest design is shown schematically on the left-hand side in Fig. 3.1. It consists of two parallel electrodes that are driven by an rf source with no applied external magnetic field. It is operated in a frequency range of 1–100 MHz, but mostly at the technical frequency of 13.56 MHz or its higher harmonics. Thin positive ion sheaths form in front of the electrodes as the electron mobility is much higher than that of the ions ($v_{th,e} \approx 100 v_{th,i}$) [Stangeby, 2000; Riemann, 1991]. The electrons are therefore faster lost to the electrodes and the electrodes charge up negative with respect to the plasma (cf. right-hand side of Fig. 3.1). The sheath thickness varies during an rf cycle as the electrons of the bulk plasma between the sheaths are attracted or repelled by either electrode, depending on their instantaneous voltage. The ion inertia is much higher due to the larger ion mass so that the ions cannot react to the changing electric fields during an rf cycle ($f = 13.56\,\text{MHz} > f_{pi} \approx 3\,\text{MHz}$). Their motion is due to time-averaged electric potentials only. The plasma potential ϕ_{pl} ($= V_p$ in Fig. 3.1) establishes to a few $k_B T_e/e$ with respect to the wall potential to confine the electrons. The ion bombardment energy, the energy the ions gain in the potential drop of

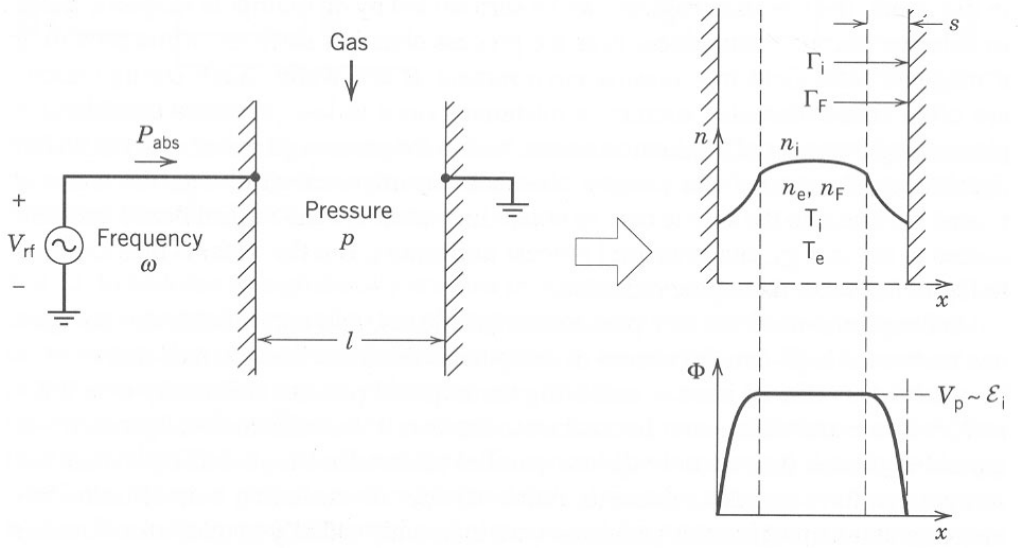

Figure 3.1: Schematic of an asymmetric capacitive discharge with two parallel plates (left). The radial plasma density and plasma potential distribution is depicted on the right. Taken from [Lieberman and Lichtenberg, 1994].

the sheath, on the walls is thus in the order of a few $k_B T_e/e$. In industrial plasma etching applications, the substrate is usually placed on the driven electrode and a blocking capacitor is introduced between the rf source and the electrode. In such discharges, also called rf diodes, the energy of the ions accelerated towards the substrate can be substantially higher, as high as the applied rf voltage.

The energy transfer of rf power is mainly to the electrons, which in turn ionise the neutral atoms by inelastic collisions. The heating mechanism itself it twofold: First, power is absorbed in the bulk plasma by Ohmic heating. The oscillating electrons of the bulk plasma collide with the neutral particles and transfer energy by inelastic collisions. The power deposition per unit area due to Ohmic heating can be derived analytically for a simple symmetric discharge [Lieberman and Lichtenberg, 1994] and reads

$$\bar{S}_{Ohm} = \frac{1}{2}\frac{m_e \nu_{en} d}{e^2 n} j_{\mathrm{rf}}^2 \,. \tag{3.1}$$

Here, d is the bulk plasma length between the electrodes, ν_{en} is the electron-neutral collision frequency, and j_{rf} the rf current density. Secondly, stochastic heating provides a collisionless way of power deposition. Electrons are reflected by the fast moving electric fields in the sheath regions. Assuming a Maxwellian electron energy distribution, there is a net positive energy transfer to the plasma. Again, the power absorption can be given analytically [Lieberman and Lichtenberg, 1994]

$$\bar{S}_{stoc} = \frac{1}{2}\frac{m_e v_{th,e}}{e^2 n} j_{\mathrm{rf}}^2 \,. \tag{3.2}$$

In magnetically enhanced discharges, an external magnetic field is superimposed parallel

to the electrodes [Park and Kang, 1997; Lieberman et al., 1991]. Here, the Lorentz force introduces an anisotropy in the plasma. While the charged particle motion along the magnetic field is not affected, their mobility perpendicular to the magnetic field is strongly reduced. The electrons of the bulk plasma can therefore no longer oscillate freely between the electrodes during an rf cycle. The magnetic field effectively suppresses Ohmic heating. The stochastic process in turn is enhanced by the magnetic field as the electrons close to the sheath can collide several times with the fast moving sheaths; a gyrating electron can now collide again after approximately half a gyro period instead of moving directly into the bulk plasma after the first collision and thus gain considerably more energy [Lieberman and Lichtenberg, 1994]. The plasma density is magnetically mapped along a region parallel to the surface of the electrodes, which yields a maximum plasma density in the sheath edge.

Major disadvantages of capacitive discharges (also magnetically enhanced) are their relatively low plasma density ($n \leq 10^{17}\,\mathrm{m}^{-3}$) and their lack of independent control of plasma potential and plasma density. Controlling plasma density and plasma potential independently from each other is particularly important in etching reactors, where a high ion flux is necessary but high ion energy leads to defects in the etching substrate [Lieberman and Lichtenberg, 1994]. A dielectric material (glass or ceramics) between the electrodes and the plasma reduces the voltage across the sheath and thereby the ion impact energy. A second electrode can control the ion energy if necessary [Schneider et al., 1999a; Aanesland et al., 2001]. The problem of relatively low plasma densities, however, remains.

3.2 Inductive Discharges

The simplest possible inductive discharge consists of a current driven coil placed around a cylindrical dielectric vacuum tube, as shown schematically in Fig. 3.2. It is operated at frequencies in the range of 1–$100\,\mathrm{MHz}$, well below the self-resonance frequency of the coil. Again, no magnetic field is necessary to operate an inductive discharge, but it may help to map the source plasma loss-free to a remote region. With an inductive discharge, plasma densities up to $n \leq 10^{18}\,\mathrm{m}^{-3}$ can be reached, which is one order of magnitude above capacitively coupled discharges. In inductive discharges, the rf power coupling to the plasma is Ohmic and stochastic, as well. But, the oscillating electric fields have now two origins: First of all, the voltage drop over the coil leads to oscillating electric fields between the two ends of the coil like in a capacitive discharge. The voltage drop (and thus the capacitive coupling) can be reduced by using a coil with low winding number (low inductance) or by inserting a Faraday shield between the antenna and the dielectric [Hopwood, 1992]. Secondly, the rf current in the antenna induces an electric field inside the antenna and drives an electron current that heats the plasma via collisions. In contrast to a classical capacitive discharge, where the rf current path is through the plasma, the induced electric fields in an inductive discharge can only penetrate the surface of the

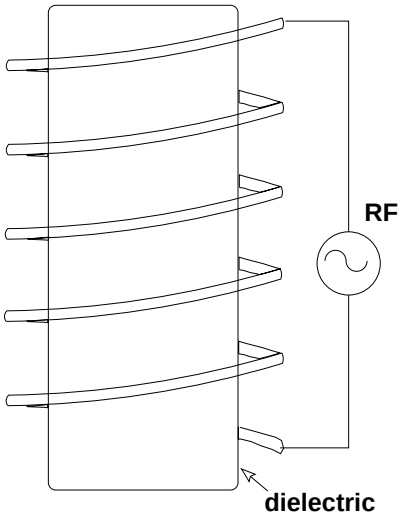

Figure 3.2: Schematic of a simple inductive discharge. Inductive fields are created by an rf coil which is wound around a dielectric.

plasma within the skin depth δ. For a collisionless plasma ($\nu_{en} \ll \omega$) the skin depth reads [Lieberman and Lichtenberg, 1994]

$$\delta_p = \frac{c}{\omega_{pe}} \,. \tag{3.3}$$

Calculating some numbers for the collisionless skin depth and comparing them to the source radius R of the VINETA experiment used in the present work, one can distinguish two different regimes:

1. $n = 10^{16}\,\mathrm{m}^{-3} \rightsquigarrow \delta_p = 53\,\mathrm{mm} \gtrsim R$ (low density, large skin depth)
2. $n = 10^{17}\,\mathrm{m}^{-3} \rightsquigarrow \delta_p = 17\,\mathrm{mm} < R$ (high density, small skin depth).

The skin depth is a measure for the distance within which the electric field inside the antenna has decreased to its $1/e$-value compared to the vacuum case. In other words, currents are induced within the skin depth which shield out the electric fields in the plasma body. These currents become important and contribute significantly to the plasma heating process at higher densities and have maximum efficiency if the skin depth becomes the vessel radius ($\delta_p \approx R$) [Lieberman and Lichtenberg, 1994; Hopwood, 1992]. If a magnetic field is superimposed on the discharge, the skin depth is even increased. The skin depth is directly related to the conductivity of the plasma and the magnetic field introduces an anisotropy that further complicates the calculations. An analytic expression relating only the directly perpendicular and parallel components of the conductivity tensor $\underline{\sigma}$ was given by Bittencourt [1995]

$$\sigma_\perp = \frac{(\nu_c - \mathrm{i}\omega)^2}{(\nu_c - \mathrm{i}\omega)^2 + \omega_{ce}^2}\sigma_\parallel \,, \tag{3.4}$$

where ν_c is the collision frequency and ω_{ce} the electron cyclotron frequency. Thus, the perpendicular conductivity decreases with B_0 and with it, the perpendicular skin depth increases, $\delta_\perp \propto B_0$. In agreement with this, it has been reported for low magnetic fields that a transition from the capacitive to the inductive mode occurs at densities where the skin depth for unmagnetised plasmas, Eq. (3.3), is roughly half of the source radius [Degeling et al., 1996]. Later, a constant $\sigma_\perp/R$ ratio was reported at various magnetic fields for the transition to the helicon mode [Degeling et al., 1998].

With inductive discharge setups, two operational modes can be maintained. At lower densities, where the skin depth is larger than the plasma radius, there is no significant effect of shielding out electric fields. The electric field distribution is almost equal to the vacuum case and the power is transferred via the sheath near the antenna, just like in a capacitive discharge [Ellingboe and Boswell, 1996]. Only at higher rf powers (higher plasma densities) the induced currents are large enough to contribute significantly to the heating process. The low density operational regime of a conventional helicon source is therefore called 'capacitive' mode and the higher density regime 'inductive mode', according to their major rf power absorption mechanism. The highest density regime, where helicon waves sustain the discharge, is called 'helicon mode' and is reviewed in the next section.

3.3 Helicon Discharges

Since their invention in the mid 1980's by Boswell [1984b], helicon sources are widely used because of their ability of very efficient plasmas production with plasma densities up to $n \leq 10^{20}\,\mathrm{m}^{-3}$ with only a few kW of rf power [Boswell and Chen, 1997; Chen and Boswell, 1997]. A simple estimation for a cylindrical discharge (length l and radius R) with axial magnetic field underlines the surprisingly effective ionisation (following Chen [1991]): The axial magnetic field strongly inhibits the radial particle motion due to the Lorentz force. Usually, even the ion Larmor radius is smaller than the device radius ($\rho_e \approx 0.5\,\mathrm{mm} \ll \rho_i \approx 10\,\mathrm{mm} < R$). The plasma is therefore lost predominantly at the grounded axial endplates (wall). As the electrons are much more mobile than the ions, the wall potential is negative with respect to the plasma space charge potential and a positive sheath forms in front of the wall. To maintain such a sheath, the ions have to be accelerated in a pre-sheath according to the Bohm criterion and the plasma is lost by drift with the ion acoustic velocity c_s [Riemann, 1991]. The ion particle loss rate dN/dt to one endplate with surface $A = \pi R^2$ is therefore $dN/dt = Anc_s$. If W is the average energy necessary for a single ionisation process, the power needed to sustain a steady state discharge with constant time averaged density is $P = WdN/dt$. Typical parameters in VINETA for helicon mode discharge are $R = 0.05\,\mathrm{m}$, $c_s = 3460\,\mathrm{m/s}$, $P = 2.5\,\mathrm{kW}$, and $n = 10^{19}\,\mathrm{m}^{-3}$. This leads to an effective ionisation energy of $W = 57\,\mathrm{eV}$. The ionisation energy of argon is $E_{ar} = 15.8\,\mathrm{eV}$ which means that every fourth inelastic collision must

ionise an atom. This has to be compared to other discharges, where only about one in ten to fifteen inelastic collisions ionises, which corresponds to an effective ionisation energy $\approx 200\,\mathrm{eV}$.

Helicon sources are widely used in research laboratories and have been used in material processing [Perry et al., 1991; Chen, 1995; Chen et al., 2001], for plasma production in toroidal devices [Loewenhardt et al., 1991; Tripathi and Bora, 2001], and in thruster experiments [Chang Diaz, 1999, 2000]. Helicon sources can even be bought ready made for material processing applications [HARE© helicon source; MORI© helicon source]. In contrast to capacitive and inductive discharges, helicon discharges require a magnetic field that is typically in the range of $10 - 100\,\mathrm{mT}$. Some sources have also been operated at low magnetic fields $< 10\,\mathrm{mT}$ [Degeling et al., 1996; Kaeppelin et al., 2001]. Helicon sources commonly consist of an rf driven antenna placed around a cylindrical glass vacuum tube immersed in a magnetic field parallel to the cylinder axis. The antenna excites a helicon wave (see Sec. 2.4.1) that is responsible for the plasma production. Many different antenna designs have been tested and used [Balkey et al., 2001; Light and Chen, 1995], but mostly antennae with right-hand helical winding ($m = +1$ antenna, see Figs. 4.2 and 4.21) are used. Experiments measuring the spatial distribution of the magnetic fluctuations of the helicon wave give a detailed understanding of the propagation, damping, and radial mode structure of the helicon wave [Light and Chen, 1995; Light et al., 1995; Ellingboe and Boswell, 1996]. Despite this, the damping mechanism itself is still poorly understood and under intense scientific debate, e.g. during the APS Mini-Conference on Applications of Helicon Plasma Sources [2001]. The three most promising possible explanations are briefly reviewed in the following:

1. It was proposed that *Landau damping* of helicon waves could explain the high damping rate and thus the efficient wave-particle energy transfer [Chen, 1991]. Landau damping is a collisionless kinetic effect, where the wave energy is transferred to particles propagating slightly below the phase velocity of the wave. The Landau damping rate is given by

$$\frac{\mathrm{Im}(k)}{\mathrm{Re}(k)} = 2\sqrt{\pi}\frac{v_{th}3.83}{\omega_{ce}a}\zeta^4 \exp -\zeta^2\,, \tag{3.5}$$

   where a is the plasma radius and $\zeta = \omega/kv_{th}$ [Chen, 1991; Keiter et al., 1997]. Fig. 3.3 shows the Landau damping rate vs electron temperature for different combinations of ω/k. Typical electron temperatures measured in a helicon source are 2–$10\,\mathrm{eV}$. This means, the damping rate is well below $3\,\%$, too small to contribute significantly. For higher temperatures around 25–$50\,\mathrm{eV}$ the damping rate approaches $\lesssim 10\,\%$ for favourable wave phase velocities ω/k and could well contribute to wave damping. Therefore, numerous experimental efforts have been made to find a high temperature electron population in helicon discharges, but the results are ambiguous. In earlier experiments, direct measurements with Langmuir probes [Loewenhardt et al., 1995] and energy analysers [Molvik et al., 1997], as well as

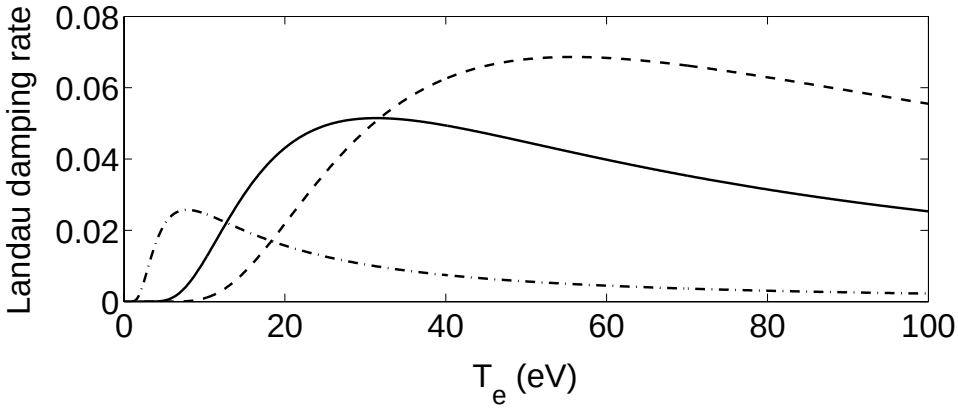

Figure 3.3: Plot of the Landau damping rate [$\mathrm{Im}(k)/\mathrm{Re}(k)$, Eq. (3.5)] for different driving frequencies and wavelengths. $f = 13.56\,\mathrm{MHz}$, $\lambda = 150\,\mathrm{mm}$ (solid), $f = 13.56\,\mathrm{MHz}$, $\lambda = 200\,\mathrm{mm}$ (dashed), and $f = 27.12\,\mathrm{MHz}$, $\lambda = 150\,\mathrm{mm}$ (dash-dotted).

spectroscopic measurements [Ellingboe et al., 1995] showed the existence of high energy electrons. On the other hand, more recent experiments used carefully compensated probes and energy analysers and clearly ruled out the existence of high energy electrons [Chen and Blackwell, 1999; Blackwell et al., 2002].

2. The coupling to *Trivelpiece-Gould (TG) waves* was proposed as another mechanism responsible for the efficient absorption of rf power in helicon discharges [Shamrai and Taranov, 1996]. As already shown in Sec. 2.4.1, the dispersion Eq. (2.47) yields two modes: the weakly damped helicon mode Eq. (2.52) and the strongly damped slow mode Eq. (2.51). If the plasma, and with it the wave, extend up to the conducting boundary vessel, both modes can coexist. If there is a vacuum gap between the plasma and the conducting boundary or if there is an insulating boundary, and this is the case in most helicon experiments, the boundary conditions can only be satisfied by a superposition of both modes [Shamrai and Taranov, 1996]. Both modes couple at the plasma surface and energy may be transferred from the weakly damped helicon mode to the strongly damped slow mode wave. A direct measurement of slow mode waves in conventional helicon sources is extremely difficult as their perpendicular wavelength is very small at commonly used magnetic field strengths. For example for $B_0 = 50\,\mathrm{mT}$, the perpendicular wavelength is obtained from Eq. (2.51) to $\lambda_\perp \approx 1.5\,\mathrm{mm}$ ($\omega_{ce}/2\pi = 2.8\,\mathrm{GHz}$, $\omega/2\pi = 27\,\mathrm{MHz}$, $k_\parallel = 0.01 k_\perp \Rightarrow \lambda_\perp \approx 0.01\lambda_\parallel$; $\lambda_\parallel \approx 150\,\mathrm{mm}$ cf. Chap. 6). As the slow mode waves are strongly damped, they only exist in a small region at the surface of the plasma, too small to be resolved by direct measurements. For much lower magnetic fields, however, the waves extend much deeper into the plasma. For $B_0 = 1\,\mathrm{mT}$, e.g., the perpendicular wavelength is $\lambda_\perp \approx 0.57\lambda_\parallel \approx 86\,\mathrm{mm}$ ($\omega_{ce} = 57\,\mathrm{MHz}$). Due to the experimental difficulties to study the role of slow mode waves in the plasma heating scenario, numerical antenna-plasma-coupling simulations were done to gain insight into the deposition of the wave energy into the plasma. The results, how-

ever, are ambiguous and are strongly influenced by the underlying model. A cold plasma antenna-wave coupling code showed that 'the TG waves do not lead to a significant increase in antenna coupling' [Borg and Boswell, 1998]. A different code that compared the simulation results with analytic expression for the simple homogeneous case in turn showed that the 'TG mode dominates the heating at low magnetic fields and deposits its wave energy near the edge region' [Mouzouris and Scharer, 1998]. Recent experimental evidence for the existence of slow mode waves in a helicon discharge at low magnetic fields was found by comparing measurements of the current profiles using a miniature Rogowski coil with numerical simulations [Blackwell et al., 2002]. An indirect measurement using Laser Induced Fluorescence (LIF) was proposed by Kline et al. [2000] and Franck et al. [2000] and is further discussed in Sec. 4.2.4.

3. Recently, *lower hybrid wave coupling* has regained attention and is thought of as being important for explaining the efficient coupling mechanism. Resonant coupling of lower hybrid waves (Sec. 2.3.1) was used for plasma heating, mainly in fusion applications [Pinsker, 2001; Brambilla, 1976, 1979; Cho and Swanson, 1988] but has long been neglected in the helicon community although Boswell's original paper reported on the 'very efficient plasma generation by whistler waves near the lower hybrid frequency' [Boswell, 1984b]. Recent experiments with varying magnetic field showed a maximum plasma density [Zhu and Boswell, 1989; Kwak et al., 1997; Yun and Chang, 1998; Cho, 2000] and maximum ion temperature [Balkey et al., 2001] to be established always close to the lower hybrid frequency. These experiments are supported by a numerical study using a self-consistent code solving the wave equation together with the balance equations for electron density and temperature. It was shown that the plasma resistance has a maximum near the lower hybrid frequency that could be responsible for the efficient ionisation [Cho, 2000].

4

Experimental Techniques

4.1 The Plasma Experiment VINETA

Figure 4.1: Picture of the linear magnetised plasma experiment VINETA in configuration for rf plasma production. The insets show the helicon discharge mode in argon seen through an optical bandpass filter around (442 ± 5) nm.

The conceptual idea of the VINETA[1] device is to have a flexible and large linear magnetised plasma experiment to study various different aspects of wave dynamics. Fig. 4.1 shows a photograph of the device and a schematic is plotted in Fig. 4.2. In the design, special emphasis is put on the accessibility with diagnostic tools to facilitate optimal measurements. To ensure easy handling and maintenance, the device follows a modular concept and consists of four identical modules. Each module is made up of a stainless

[1]VINETA is an acronym for "**V**ersatile **I**nstrument for studies on **N**onlinearity, **E**lectromagnetism, **T**urbulence, and **A**pplications".

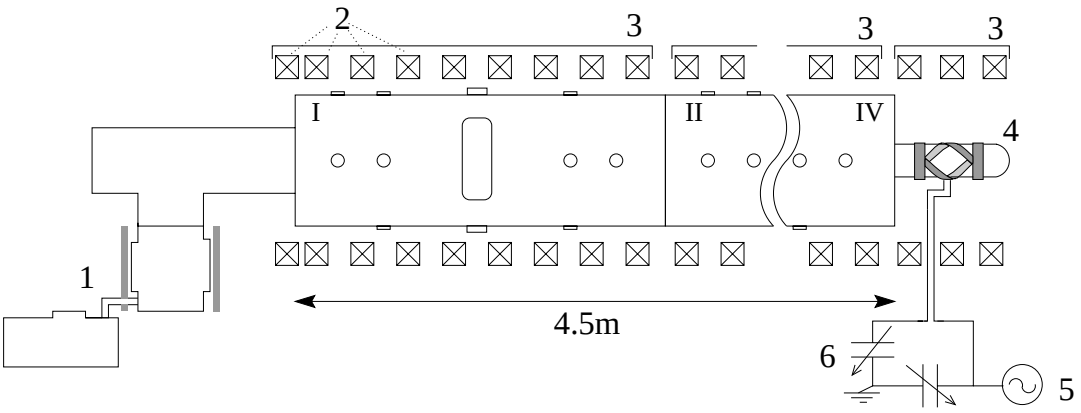

Figure 4.2: Schematic of the VINETA experiment in configuration for rf produced plasma. Shown are the vacuum chambers I-IV, vacuum pumps (1), field coils (2) with their dc power supplies (3), glass vacuum extension with helical antenna (4), rf power supply (5), and matching unit (6).

steel chamber with 400 mm in diameter and 1128 mm in length. The chamber has thirteen CF-40, two CF-60, and two rectangular (250×90 mm^2) flanges and is placed on a trolley.

Each vessel is immersed in an axial linear magnetic field created by eight water cooled coils. Each coil has a diameter of 600 mm and is made up of 45 windings of copper with rectangular profile (5x5 mm^2) and central bore. Additional coils at the end segments ensure a homogeneous magnetic field over the entire device. The maximum magnetic field of 100 mT can be established with a spatial magnetic ripple less than $1\,\%$. The coils of each module are freely positionable along the axial direction and are supplied by a 60 kW dc power supply. This enables the realisation of a large variety of magnetic field configurations, either by adjusting the positions of the coils along the axis or by operating the modules at different coil currents. Fig. 4.3 shows three different example magnetic field configurations. The two graphs (a) and (b) show the magnetic field strength of the standard homogeneous configuration with maximum coil current of 260 A. The vessel dimensions are indicated in both graphs by the dotted lines. The colour-coded graph (a) clearly shows the great homogeneity of the magnetic field over the entire chamber volume. The magnetic field strength along the axis is plotted for different radial positions in graph (b). The magnetic ripple on axis ($r = 0$ mm) is below $0.1\,\%$. With increasing radius ($r = 100$ mm and $r = 150$ mm), the inhomogeneity increases but stays always below $1\,\%$. Fig. 4.3 (c) and (d) show colour-coded the magnetic field strength for two inhomogeneous distributions, (c) with a simple axial gradient and (d) for a 'mirror' configuration. Fig. 4.3 (e) shows the central ($r = 0$ mm) axial magnetic field for all three cases. For the axial gradient configuration (c), the two left modules are operated at 100 A and the two right ones at 260 A. The magnetic field on the left and the right are homogeneous in itself and the transition between both regions happens within ≈ 600 mm. The minimum gradient length of the magnetic field is limited by the coil diameter and cannot be steeper for the VINETA device than shown here. In the mirror configuration (d), the two centre modules are operated at 100 A whereas the two outer modules are run with 260 A, which

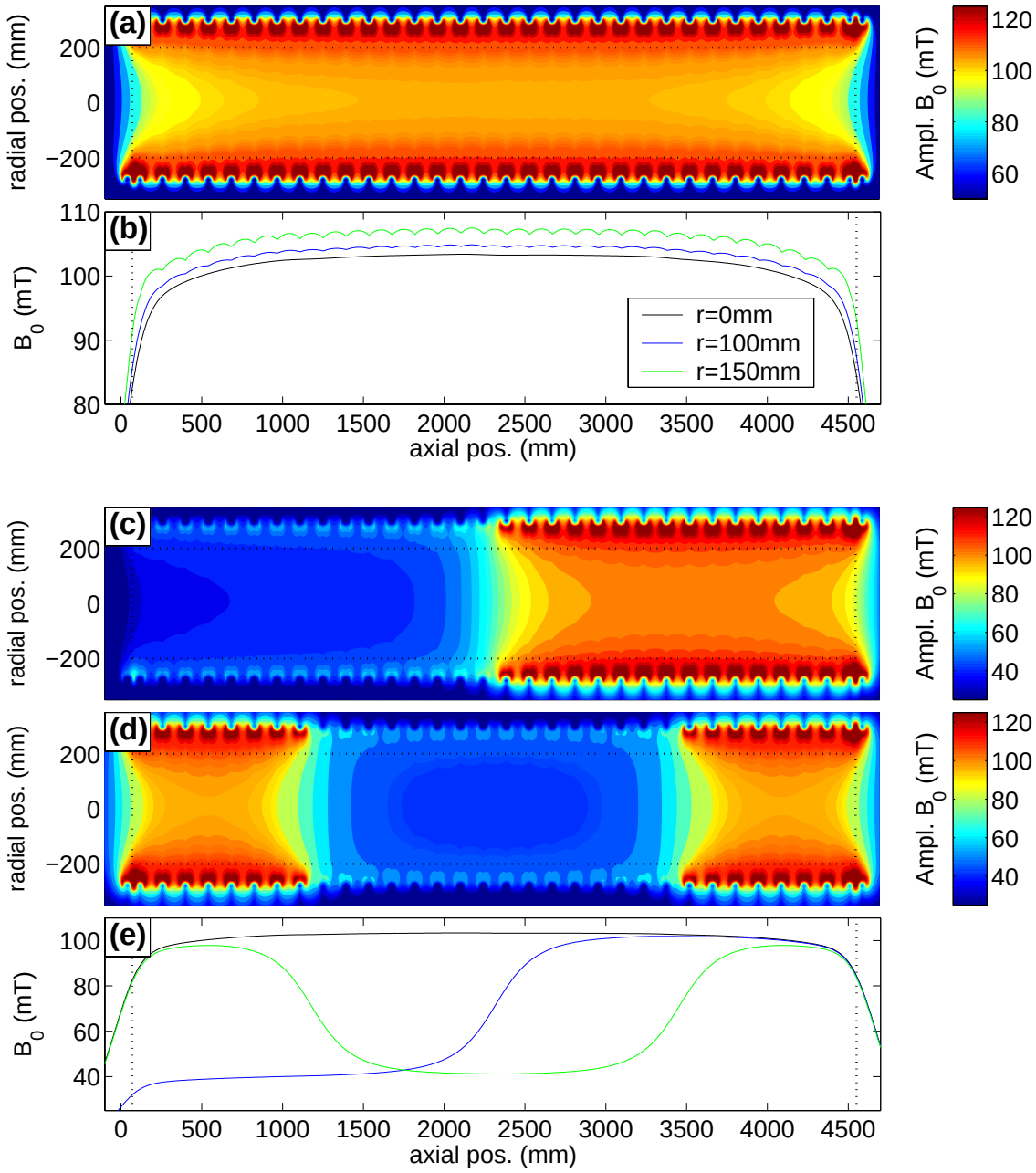

Figure 4.3: Different magnetic configurations at the VINETA experiment. Shown are colour coded a homogeneous distribution (a), a single gradient (c) and a mirror configuration (d). The 1D plots show the magnetic field strength in the homogeneous configuration along the axis for different radii (b) and on axis for all three configurations (e). The coil currents are chosen $I = 260\,\mathrm{A}$ and $I = 100\,\mathrm{A}$ in the regions of high and low magnetic field, respectively.

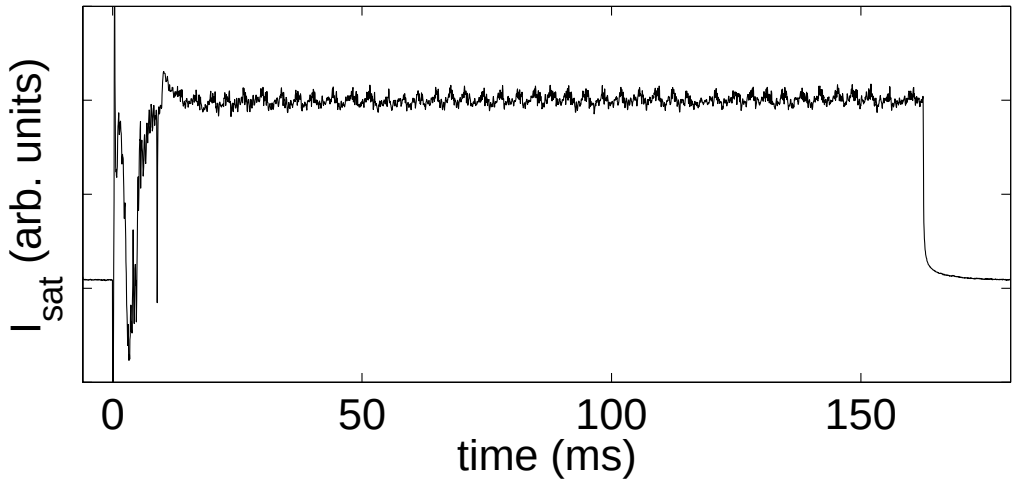

Figure 4.4: Ion saturation current measurement during an rf pulse (input power $2\,\mathrm{kW}$ and length $160\,\mathrm{ms}$). After the rf power is switched on at $t = 0\,\mathrm{ms}$, a stationary discharge is established after $\approx 20\,\mathrm{ms}$ transit time. The typical e^{-1} decay time after switching the rf power off s $\leq 1\,\mathrm{ms}$.

leads to a mirror ratio of $R_m \approx 100/40 = 2.5$. This configuration is called 'magnetic mirror' because some particles are reflected from the axial magnetic field gradients and are confined to the central region of lower magnetic field [Chen, 1984; Goldston and Rutherford, 1995]. This configuration is still used nowadays for plasma confinement in fusion related experiments [Hwang et al., 1999]. Not shown here, but also of practical use are configurations where the position of the coils is changed. Each coil is freely positionable along the axial direction and enable numerous further magnetic configurations like gradients and mirrors with higher ratio of the magnetic fields or configurations with regions of zero magnetic field (null-points).

The vacuum is established by a rotary pump and a turbo pump that are installed on one end of the VINETA device. Both pumps enable a base pressure of $1 \cdot 10^{-4}\,\mathrm{Pa}$ without baking. The plasma source is installed on the opposite end of the machine. It is a standard helicon source and consists of a Pyrex vacuum extension of $500\,\mathrm{mm}$ length and $100\,\mathrm{mm}$ diameter with a right-hand helical copper antenna [Light and Chen, 1995]. An extra set of three coils and an extra power supply extends the magnetic field to the antenna region. The antenna is fed by a high-power rf source/amplifier and is matched with a standard L-matching circuit [Rayner et al., 1996]. The rf source can be operated at frequencies $f = 2$–$30\,\mathrm{MHz}$ and the amplifier yields output powers up to $P = 2.5\,\mathrm{kW}$ (cw) and $P = 6\,\mathrm{kW}$ (pulsed). The rf power is monitored with two Bird© metres, one for forward and one for reflected power. The rf antenna current is measured with a calibrated current monitor. In the homogeneous magnetic field arrangement used in the course of this thesis, the plasma radius is limited by the antenna radius of $50\,\mathrm{mm}$. Magnetic configurations with high magnetic field at the source and lower magnetic field within the chamber enable plasma expansion to a larger diameter (but consequently lower density). Depending on the applied rf power, the plasma density is in the range of $n = 10^{15}$–$10^{19}\,\mathrm{m}^{-3}$. At higher

input powers ($P_{\mathrm{rf}} \geq 1.5\,\mathrm{kW}$, $I_{\mathrm{rf}} \approx 60\,\mathrm{A_{rms}}$) the glass cylinder cannot withstand the plasma heat load and is liable to melt or break. A hollow antenna with water cooling enables a cw operation up to higher powers, but the principle problem remains. The source is therefore typically operated in a pulsed mode with pulse lengths of ≈ 0.2–$2\,\mathrm{s}$ and a duty cycle of 10–$50\,\%$. Fig. 4.4 shows a plasma density measurement during an rf pulse of $160\,\mathrm{ms}$ length at an rf power of $2\,\mathrm{kW}$ (helicon mode). The density increases during the first $20\,\mathrm{ms}$ before it reaches a stationary phase with constant plasma density. Evidently, in pulsed plasma operation, the measurements must be taken in the stationary phase to avoid spurious effects. Measurements on timescales well below $\ll 1\,\mathrm{ms}$ can be made in the plasma afterglow. The plasma in this phase is very quiescent and may improve on signal-to-noise-ratio of sensitive measurements. On the other hand, signal averaging must be done in repetitive pulses and thus, longer measurement times have to be accepted.

Table 4.1 gives an overview of the operational and plasma parameters in VINETA for the experimental conditions in this work. Helicon plasma sources may operate in three distinctively different modes, the capacitive, the inductive and the helicon wave sustained mode (see above). The table compiles the plasma and operation parameters of the three modes. The discharge mechanisms were reviewed in Chap. 3 and investigated thoroughly for the VINETA device in Chap. 6. As mentioned above, one of the strengths of the VINETA device is its accessibility. The numerous ports enable parallel measurements with multiple diagnostics or subsequent measurements without breaking the vacuum. Two two-dimensional positioning systems provide spatial measurements with high resolution. One poloidal positioning system (the plane of the plasma cross section perpendicular to the ambient magnetic field) can be flanged to one of the large rectangular windows. Two computer controlled servo motors enable free positioning in a rectangular plane perpendicular to the axial magnetic field with $\approx 200\,\mathrm{mm}$ in vertical and $\approx 250\,\mathrm{mm}$ in the horizontal dimension (see grey plane in schematic of Fig. 4.20). The probes are fixed on a carriage and connected to up to eight coaxial cables which are tautened in a lever system and soldered to vacuum feedthroughs. Two linear motion vacuum feedthroughs move the carriage independently in vertical and horizontal direction. The positioning accuracy of the system is better than $1\,\mathrm{mm}$. While the poloidal positioning unit is completely mounted outside the VINETA device, the second system is installed in the lower section inside the device. The highest part of the system, the movable carriage, is only $70\,\mathrm{mm}$ in height, enabling the operation of an undisturbed plasma with $260\,\mathrm{mm}$ diameter. This system enables probe positioning in the horizontal plane parallel to the magnetic field with $\approx 3000\,\mathrm{mm}$ in axial and $\approx 200\,\mathrm{mm}$ in radial direction (see grey plane in schematic of Fig. 4.21). Two servo motors, connected to rotational vacuum feedthroughs, move the carriage via two tooth belts. Again, the probe leads are connected to coaxial cables at the carriage and the cables are connected to coaxial vacuum feedthroughs.

Table 4.1: Summary of the typical operational and plasma parameters in the VINETA device for the different discharge modes.

	Argon capacitive	Argon inductive	Argon helicon	Helium helicon
base pressure p_b (Pa)		$\lesssim 10^{-4}$		
magnetic field B_0 (mT)		≤ 100		
gas pressure p (Pa)	10^{-2}–1	0.5–1	> 0.3	2.5
rf power P_{rf} (kW)	< 0.5	0.5–1	> 1	> 3
plasma density n (m^{-3})	10^{15}–10^{17}	10^{17}–10^{18}	10^{18}–10^{19}	10^{18}–10^{19}
ionisation η (%)	0.1–1	1–10	10–100	10–100
electron temperature T_e (eV)	1	3	5	5
ion temperature T_i (eV)	≈ 0.025	≥ 0.025	≤ 0.2	≤ 0.2
Debye length $\lambda_{De}(\mu\mathrm{m})$	24–237	13–41	5–17	5–17
electron gyro radius ρ_e (μm)	25–500	50–900	50–1100	50–1100
ion gyro radius ρ_i (mm)	1–10	1–10	3–30	1–10
electron plasma frequency f_{pe} (GHz)	0.3–3	3–9	9–28	9–28
ion plasma frequency f_{pi} (MHz)	3–11	11–33	33–100	100–330
electron cyclotron frequency f_{ce} (GHz)		≤ 2.8		
ion cyclotron frequency f_{ci} (kHz)		≤ 38		≤ 380
upper hybrid frequency f_{uh} (GHz)	≤ 4	≤ 9.5	≤ 28.5	≤ 28.5
lower hybrid frequency f_{lh} (MHz)	≤ 15	≤ 35	≤ 105	≤ 330
electron thermal velocity $v_{th,e}$ (10^5 m/s)	5.9	10.3	13.3	13.3
ion thermal velocity $v_{th,i}$ (m/s)	≈ 345	≥ 345	≤ 975	≤ 3080
ion acoustic velocity c_s (m/s)	550	2680	3460	10 950
Alfvén velocity v_A (10^5 m/s)	< 100	< 3	< 1	< 3
electron-ion collision freq. ν_{ei} (MHz)	0.04–4	0.7–6	3–28	28
electron-neutral coll. freq. ν_{en} (MHz)	0.02–2	7–40	35	43
ion-neutral collision freq. ν_{in} (kHz)	0.4–40	20–40	100	800

4.2 Diagnostic Instrumentation

Experiments in the VINETA device are done with various diagnostic instruments. A simple and widespread diagnostic tool to measure the basic plasma parameters is the Langmuir probe [Chen, 1965; Hershkowitz, 1989; Demidov et al., 2002]. It is described in Sec. 4.2.1, together with the particularities arising in rf produced and magnetised plasmas.

Magnetic fields are commonly measured with Hall sensors. Standard Hall sensors can measure magnetic fluctuations up to frequencies $f \approx 20\,\text{kHz}$ and may go up to $f < 80\,\text{kHz}$ if specially designed [Mank et al., 2001; Duran et al., 2002]. Magnetic fluctuation probes ($\dot{B}$-probes) are used to measure magnetic fluctuations at higher frequencies $f \geq 100\,\text{kHz}$. Unfortunately, these probes are susceptible to erroneous electrostatic pickup if large electrostatic fluctuations are present, which is always the case in rf produced plasmas. A variety of compensation schemes exist and help to prevent this unwanted, capacitively coupled pickup. Magnetic fluctuation probes and a detailed comparative study of pickup rejection schemes are explained in detail in Sec. 4.2.2.

Probes are always intrusive and have to be build as small as possible to minimise plasma disturbance. Non-intrusive techniques are therefore preferred but often lack spatial resolution. With the Laser Induced Fluorescence (LIF) method ion energy distributions are measured and if the distribution is a Maxwellian one , the ion temperature can be derived. If a coherent perturbation causes a disturbance in the distribution, the perturbed ion energy distribution function may be measured. The LIF-methods used here are explained in Secs. 4.2.3 and 4.2.4.

The absolute line integrated plasma density is measured non-intrusively with a microwave interferometer, which is explained in Sec. 4.2.5.

4.2.1 Langmuir Probes

Due to their technical simplicity, Langmuir probes are widely used to determine the basic stationary plasma parameters such as plasma density n, electron temperature T_e, plasma potential ϕ_{pl}, and floating potential ϕ_{fl}. In the simplest case they consist of a cylindrical or plane electrode that is connected to an electrical circuit measuring current-voltage-characteristics (IU-curves); schematically shown in Fig. 4.5 (a) and (c). Langmuir probes can in principle be used in all sorts of plasmas, their applicability in high density and high temperature plasmas is only limited by the thermal load they can withstand.

- In *unmagnetised plasmas* the probe characteristics are relatively straightforward to analyse and can be divided into three parts [Chen, 1965; Cherry, 2000]: the ion saturation region, the electron start-off region, and the electron saturation region. The floating potential ϕ_{fl} is the point of vanishing net current in the IU-curve. Any floating object immersed into the plasma loads up to this potential. For strongly negative probe bias ($U_p \ll \phi_{fl}$) only ions can reach the probe and all electrons

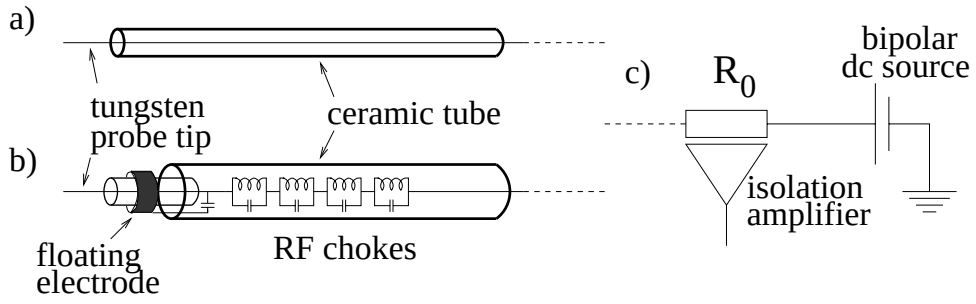

Figure 4.5: Simple Langmuir probe (a), passive rf compensated probe (b), and measuring circuit (c).

are repelled by the potential barrier. The probe current (ion saturation current) is determined by the Bohm-criterion [Riemann, 1991; Allen, 1995] and reads

$$I_{i,sat} = 0.61neA\sqrt{\frac{k_B T_e}{m_i}}, \tag{4.1}$$

where A is the effective surface of the probe. As the dependence of the electron temperature on the ion saturation current is only weak and the temperature fluctuations are usually small, $I_{i,sat}$ is a good measure for the plasma density and is sometimes used in this work to determine relative plasma density profiles. Secondly, in the electron start-off region for probe bias slightly above ϕ_{fl}, electrons start to contribute significantly to the current flow. In a plasma where the electrons are in local thermodynamic equilibrium, the electron energy distribution function is a Maxwellian one. For such a distribution with average velocity $\bar{v}_e$, the electron probe current reads

$$I_e = neA\bar{v}_e \exp\left(-\frac{e(U_p - \phi_p)}{k_B T_e}\right). \tag{4.2}$$

From a best fit of this formula to the electron start-off region in a measured IU-curve, the temperature T_e can be derived. For voltages larger than the plasma potential ϕ_{pl} the current to the probe is carried by the electrons only. This electron saturation current is given by

$$I_{e,sat} = neA\sqrt{\frac{k_B T_e}{2\pi m_e}}. \tag{4.3}$$

The effective surface area A of the probe is only for large plane probes constant. In particular for cylindrical probes the effective area increases due to sheath expansion effects with increasing probe bias [Chen, 1965].

- The long known problems with the use of electrostatic probes in *magnetised plasmas* are twofold [Chen, 1965]. First, the charged particle motion is anisotropic. The particles can move almost freely in direction of the magnetic field whereas

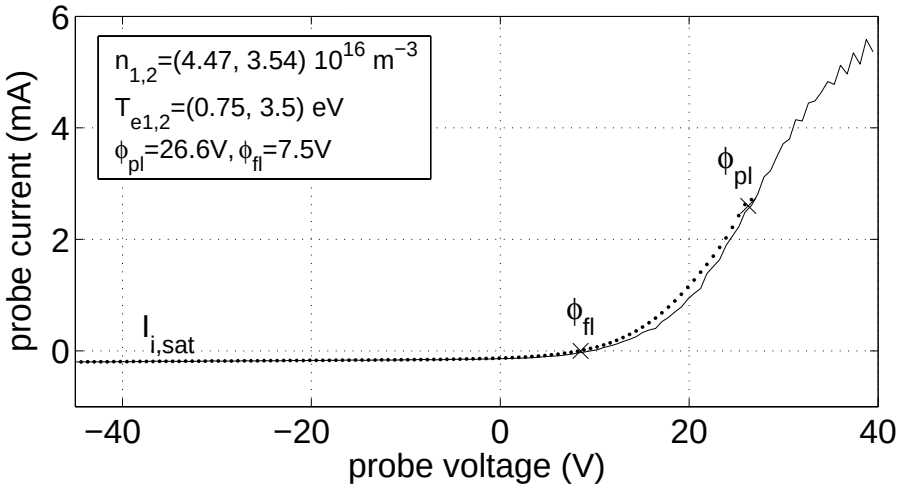

Figure 4.6: Example IU-characteristic. Shown are measurements with a compensated Langmuir probe (solid line) and a two-temperature fit using the theoretical framework presented by Demidov et al. [1999] (dashed line), which provides the plasma densities $n_{1,2}$ and the electron temperatures $T_{e1,2}$ for two superimposed thermalised components.

their motion perpendicular is strongly reduced due to the Lorentz force. Second, the effective mean free path perpendicular to the magnetic field is now given by the Larmor radii (ρ_e, ρ_i) and the way the charged particles, especially electrons, reach the probe is strongly affected. A partially kinetic probe theory was developed by Demidov et al. [1999] for cylindrical probes aligned perpendicular to the magnetic field where electrons are strongly magnetised (ρ_e smaller than the probe dimensions). Starting with the Boltzmann kinetic equation it is then possible to relate the electron energy distribution function $f(eV)$ to the first derivative of the probe current

$$f(eV) = -\frac{3m^2 R \ln(\pi L/4R)}{8\pi e^3 \rho_e V} \frac{\mathrm{d}j_e}{\mathrm{d}V}\,, \tag{4.4}$$

where R and L are the radius and the length of the probe. By fitting a one- or two-temperature Maxwellian function to the measured values the plasma electron temperature (or temperatures) is obtained.

- In *rf produced plasmas*, the probe characteristic is strongly distorted due to the large potential fluctuations in the plasma that lead to fluctuations in the probe sheath voltage. The exponential dependence of the probe current on the probe bias in the electron start-off region leads to an overestimation of the electron temperature. The influence of rf potential fluctuations in the plasma can be compensated by special probe designs. A probe compensation technique suggested by Allen [1995] and Sudit and Chen [1994b] is shown in Fig. 4.5 (b). It employs rf chokes at the source frequency and the second harmonic to block off the rf currents. Moreover, the voltage across a second large surface close to the probe tip is coupled capacitively to the probe to adjust the actual probe bias with respect to the plasma potential.

A typical IU-characteristic measurement for a compensated probe is shown in Fig. 4.6 (solid line). Chokes at the rf frequency and its first harmonic, made of sub-miniature-device (SMD) capacitors and inductors, were placed close to the probe tip. The measurements are fitted reasonably well by the probe theory predictions outlined above [Demidov et al., 1999], using a two-temperature Maxwellian distribution (dotted line).

4.2.2 Magnetic Fluctuation Probes

Magnetic fluctuation probes ($\dot{B}$-probes) are widely used to measure oscillating magnetic fields in plasmas for several years [Hutchinson, 1987]. Magnetic fluctuation probes have been used in many different plasma experiments, e.g. fusion related devices [Equipe TFR, 1978; Bretz, 1997; Edlington et al., 2001; Takechi et al., 1999], mirror machines [Tanaka et al., 1999; Bak et al., 2001], inductively coupled plasma experiments [Godyak and Piejak, 1998], plasma flow generators [Black and Mayo, 1996], and helicon plasma sources [Ellingboe and Boswell, 1996; Light et al., 1995]. In high density and high temperature plasmas, magnetic fluctuation probes are generally located at the outside of the

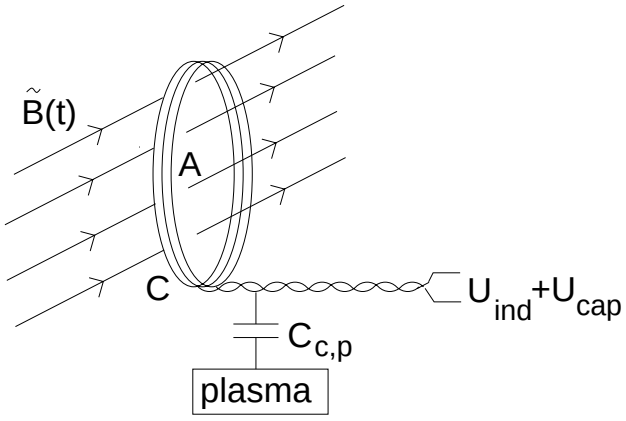

Figure 4.7: Schematic of a $\dot{B}$-probe with area surface A and contour C in a fluctuating magnetic field $\tilde{B}(t)$. The probe loop and leads are capacitively coupled to the electric fields in the plasma.

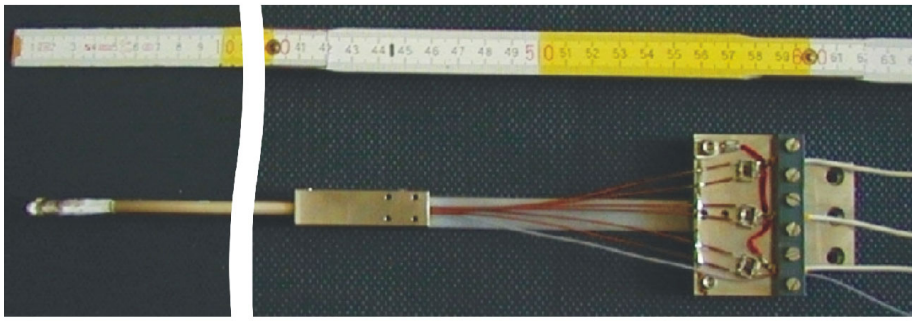

Figure 4.8: Typical $\dot{B}$-probe used in the present work. Shown are the probe tip (three orthogonally aligned loops) on the left and the electric connections on the right. The ruler units are metric.

plasma, which requires additional considerations for data evaluation. Under less demanding plasma conditions, magnetic fluctuation probes can be introduced directly into the plasma for a truly local $\dot{B}$-measurement.

$\dot{B}$-probes consist of a pickup coil of N windings of copper wire enclosing an area A with contour C, as shown schematically in Fig. 4.7. The physical principle of such a probe is based on Faraday's law

$$\oint_C \boldsymbol{dlE} = -\int_A \boldsymbol{ds}\dot{\boldsymbol{B}}\,. \tag{4.5}$$

For a coil with the surface normal parallel to the magnetic field $\boldsymbol{B}(t)$, which is varying in time but constant over the area A, a voltage $U_{ind} = -NA\dot{B}$ is induced in the probe. For a sinusoidal fluctuation $B(t) = B\sin\omega t$ the induced voltage is $U_{ind} = -NBA\omega\cos\omega t$. This means that the sensitivity of the probe increases with increasing frequency ω, with increasing number of windings N, and with increasing enclosed area A. Especially the possibility to increase the probe sensitivity by increasing A is practically not suitable as it contradicts the minimal perturbation requirement that is necessary if the probe is inserted directly into the plasma volume. Moreover, the spatial resolution for measuring field structures is determined by the coil size. It therefore seems beneficial to increase the number of windings N while keeping the area A small. However, the maximum measurable frequency of the coil is of the order of $f = R_0/L$ [Lovberg, 1965], where L is the inductance of the coil and R_0 the resistance terminating its output. The inductance of a coil is proportional to its radius r and to the square of the number of windings $L \propto rN^2$. That means that the upper limit of the frequency response decreases quadratically with the number of windings. Increasing the number of windings is therefore not always practical. As the above conditions are partially in contradiction to each other, there is an optimum value for size and number of windings. These values have to be found in accordance with the individual experimental situations. Magnetic fluctuation probes have been used to detect signals in an intermediate to high frequency range of $10\,$kHz up to a few times $100\,$MHz. For frequencies in the range above $\approx 100\,$kHz relatively small magnetic loops can be designed as a compromise between high spatial resolution and reasonably high induction signal. For the measurements presented in the present thesis, probes of $2.5\,$mm diameter with 6 windings are used to detect waves in the higher frequency range $f > 10\,$MHz. For the wave measurements at lower frequencies 10–$800\,$kHz larger probes of $15\,$mm diameter with 20 windings are used.

Electrostatic pickup rejection

A fundamental problem of $\dot{B}$-probes is their ac-coupling to electrostatic potential fluctuations, the so-called capacitive pickup [Lovberg, 1965]. This is particularly the case in rf generated plasmas, where large potential fluctuations in the order of $100\,$V are usually present. In such a case, precautions have to be taken to reduce the capacitive pickup in comparison to the actual magnetic fluctuation signal. Many different rejection schemes

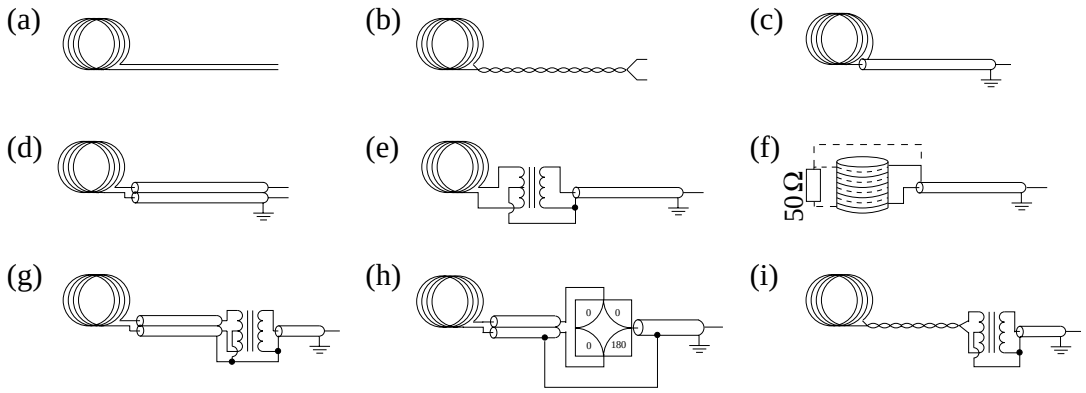

Figure 4.9: Schematic diagrams of nine different connection schemes of the magnetic fluctuation probes with and without compensation for capacitive pickup. Probes (a)-(d) are uncompensated and connected to the measuring circuit by parallel wires, twisted pair, a single coaxial cable, and two coaxial cables, respectively. Compensation methods employ centre-tapped transformers (e, g, i), hybrid combiner (h) or inherent pickup rejection (f).

have already been proposed by Borg and Cross [1987]; Loewenhardt et al. [1991, 1993]; Light and Chen [1995]. Despite their widespread use, the efficiency of these compensation methods is mostly described only on a qualitative level. Therefore, a detailed study was done that compares the relative capacitive pickup of the nine most commonly used magnetic fluctuation probe designs in a well defined test field. In this measurement, the efficiency of the rejection schemes is tested and an optimum $\dot{B}$-probe design for use in rf generated plasmas is identified (this work is also published [Franck et al., 2002b]).

A straightforward approach to reduce capacitive pickup is to use a cable with $R_0 = 50\,\Omega$ impedance at the coil output. The electrostatic voltage coupled into the probe then has to pass through a voltage divider which consists of the capacitance between the coil and the plasma $C_{c,p}$ and the output impedance R_0 of the probe [Lovberg, 1965]. Unfortunately, such coaxial cables are always thicker than simple wires and miniaturising of probes is therefore limited. A different, most commonly used approach to minimise electrostatic pickup makes use of the fact that the inductive signal of the $\dot{B}$-probe changes sign if the probe is rotated by 180° whereas the sign of the electrostatic pickup remains unchanged. Consequently, a subtractor (hybrid combiner) connected to the end of the probe eliminates the electrostatic pickup and yields two times the inductive signal [Loewenhardt et al., 1991; Schneider et al., 1999b; Borg and Jahreis, 1994]. Alternatively, the two signals can be recorded simultaneously and subtracted off-line [Keiter, 1999]. A third approach makes use of a centre-tapped transformer (also called balun). The probe can be coupled balanced to the unbalanced coaxial system of the measuring circuit. A mid-connector of the transformer winding on the probe side is grounded. The capacitive coupling gives rise to currents in the two probe legs that have equal amplitude but opposite sign with respect to ground. Thus, currents in the probe leg cancel out in the primary winding of the transformer and only the induced voltages are passed through to the measurement circuit.

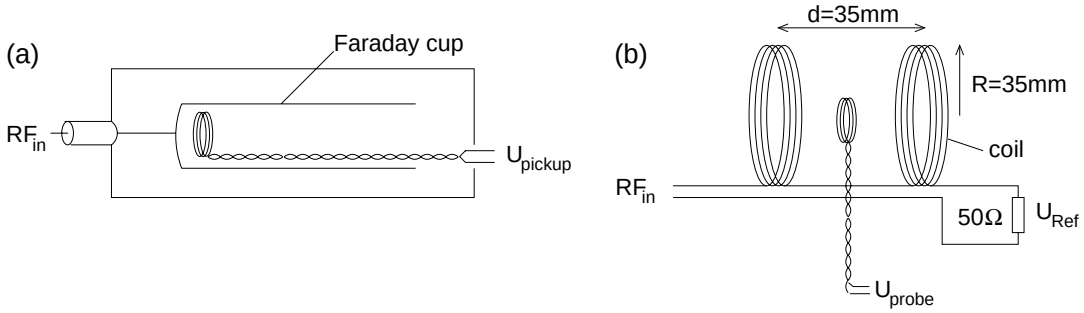

Figure 4.10: Schematic of the test-field for capacitive pickup measurement (a) and the Helmholtz coil arrangement for magnetic sensitivity calibration (b).

Fig. 4.9 shows the nine most commonly used magnetic fluctuation probe designs. The first four are uncompensated $\dot{B}$-probes with connection to the detector by simple wire (a), twisted pair cable (b), inner and outer conductor of $50\,\Omega$ coaxial cable (c), and the inner conductors of two coaxial cables with grounded shields (d). Design (e) directly connects a miniature centre-tapped transformer to the probe and feeds a $50\,\Omega$ coaxial cable. The transformer is electrostatically shielded by grounded copper tape. An inherent pickup rejection using a counter-wound second probe terminated with a $50\,\Omega$ resistor was proposed by Loewenhardt et al. [1993], shown in diagram (f). Probe design (g) and (h) use the inner conductors of two coaxial cables with grounded shield and subtract the electrostatic component via a centre-tapped transformer or a hybrid combiner, respectively, which are installed at the end of the probe. Finally, in design (i) the probe is connected to a centre-tapped transformer by a twisted pair cable.

A quantitative comparison of electrostatic pickup for the different probe designs is done in a test bed. A schematic of the setup is shown in Fig. 4.10(a). A Faraday cup with internal insulation is installed centrally into a grounded box. The inner bore of the cup is $70\,$mm in length and $20\,$mm in diameter. As the electric field inside the Faraday cup is homogeneous, a well-defined electric test-field for capacitive pickup measurements is provided. One coaxial feedthrough is used to drive the voltage on the cup and the probe is connected to two other insulated feedthroughs on the grounded box. The voltage applied to the cup in the present experiments is $U_{cup} = 50 - 100\,\mathrm{V}$ at frequencies $f = 0.25 - 25\,\mathrm{MHz}$. The electrostatic pickup signal U_p at the $\dot{B}$-probe leads is amplified by $+20\,$dB and recorded simultaneously with U_{cup}. The frequency dependence of the ratio U_p/U_{cup}, the so-called relative capacitive pickup, is plotted for the different probe setups in Fig. 4.11. There is a monotonic increase of the relative capacitive pickup with increasing frequency up to $\approx 15\,\mathrm{MHz}$. Above this frequency, resonances disturb the monotonic increase. They are due to probe and transformer inductances as well as the cable and stray capacities and vary with changing setups such as different cable lengths, different loop diameter or number of windings. This changes the quantitative values of the probes' frequency dependence in relative capacitive pickup and magnetic sensitivity but not the qualitative relation between different probe designs. Our comparative study

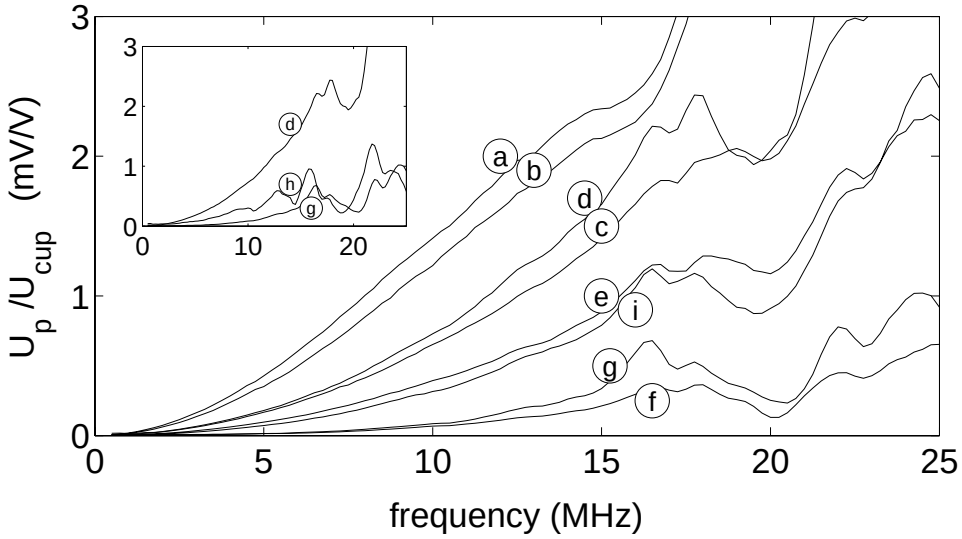

Figure 4.11: Relative capacitive pickup (U_p/U_{cup}) measurement for the nine different probe designs examined. The labelling corresponds to the labels used in the schematic plot of Fig. 4.9.

consequently remains valuable and it is of advantage to calibrate the probe in situ with the exact experimental setup used. From the relative capacitive pickup measurements we come to the following five conclusions:

1. Any of the compensation techniques considered here helps to reduce the relative capacitive pickup if compared to uncompensated probes. Compare probes (e)-(i) with (a)-(d). At a typical rf source frequency of 13.56 MHz the reduction can be up to a factor of twenty.

2. The capacitive pickup is reduced if a $50\,\Omega$-coaxial cable is used as a probe connector rather than simple parallel or twisted pair cable. This statement holds true for the uncompensated probes [(a) and (b) compared to (c) and (d)] as well as for the compensated ones [(g) compared to (i)].

3. The balun directly connected to the probe tip reduces the capacitive pickup signal less efficiently than if it is installed at the end of the probe shaft [compare (e) to (g)]. In any case, it is preferable to have the balun outside the plasma as this allows a smaller probe design.

4. In the inset of Fig. 4.11, the relative capacitive pickup for the probe with two $50\,\Omega$ coaxial cables is shown for the uncompensated probe as well as with compensations using a hybrid combiner and a centre-tapped transformer. Evidently, the electrostatic pickup rejection using a centre-tapped transformer is better than using a hybrid combiner. This is a general outcome and holds true also if the hybrid combiner is compared to the centre-tapped transformer using twisted pair cables or single

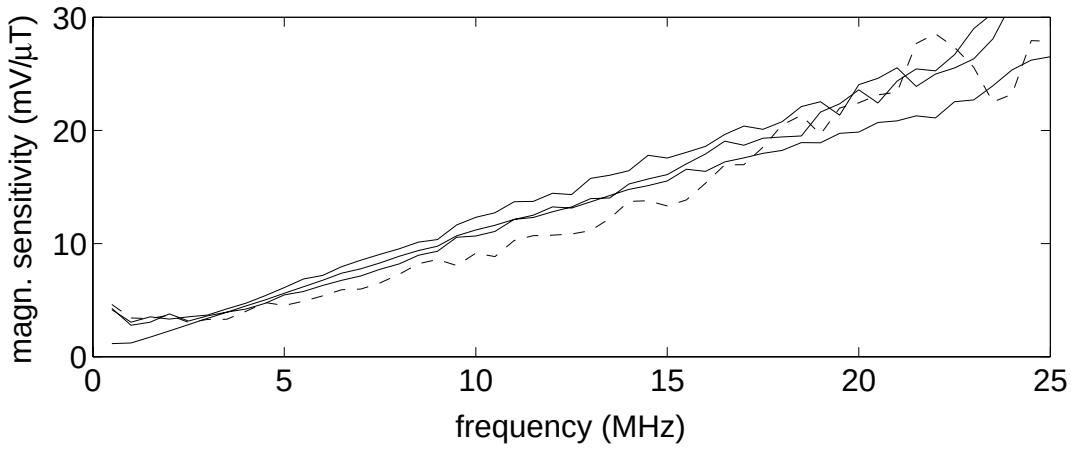

Figure 4.12: Absolute calibration of the magnetic sensitivity of the probes (d), (e), and (g) (solid lines) and the signal of probe (h) divided by two (dashed line).

coaxial lines (measurements not shown). Besides the smaller pickup, the compensation with the centre-tapped transformer is not as susceptible to resonances.

5. The probe with inherent pickup rejection at the probe tip (f) gives a slightly better result than the design with a centre-tapped balun (g). Unfortunately, such a probe is larger at the probe tip and increases the disturbance of the plasma.

From all these measurements and taking the minimum disturbance requirement into account, probe design (g) is the best-choice for magnetic field fluctuation measurements in rf discharge plasmas.

Magnetic sensitivity calibration

The magnetic fluctuation probes are absolutely calibrated for their magnetic sensitivity using two magnetic coils in Helmholtz arrangement [Phillips and Turner, 1965]. The coils consist of four turns of cable with a radius of $R_0 = 35\,\mathrm{mm}$ and are separated $35\,\mathrm{mm}$ from each other [see Fig. 4.10 (b)]. An rf voltage of frequency $0.25 - 25\,\mathrm{MHz}$ and amplitude up to $5\,\mathrm{V}$ is applied to the coils. A $50\,\Omega$ resistor is connected in series with the coils. The current through the coils is calculated from the voltage drop across the resistor and is used to calculate the magnetic test field $B_H = (4/5)^{3/2}\mu_0 nI/R_0$. The magnetic fluctuation signal is measured and is amplified by $+20\,\mathrm{dB}$. Ideally, the magnetic sensitivity of a $\dot{B}$-probe should depend only on the loop tip (size and number of windings) and not on the connecting cables nor the compensation used. As the magnetic loops of all tested probes are manufactured with identical geometry and size, and all probes are tested in the same test field setup using the same connector cables, the magnetic sensitivity from all probes should be exactly the same. Fig. 4.12 shows the measured magnetic sensitivity for the four example probe designs (d), (e), (g), and (h). The frequency dependence of the probe sensitivity is in all four cases identical within $\pm(10\text{–}15)\%$. Note that the hybrid combiner

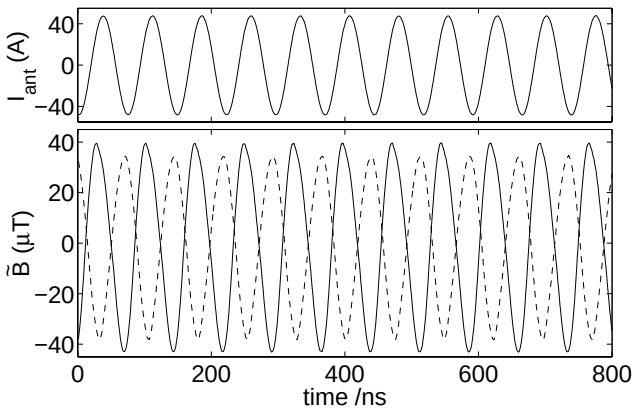

Figure 4.13: Example measurement using the "best-choice" magnetic fluctuation probe of design (g) in an rf produced plasma ($f = 13.56\,\mathrm{MHz}$). Shown are the antenna current I_{ant} (top) and the magnetic fluctuation signal $\tilde{B}$ in axial direction (bottom, solid line). Additionally, the magnetic fluctuation signal $\tilde{B}$ is shown when the probe is rotated by $180°$ (bottom, dashed line).

results in an output signal corresponding to two times the magnetic fluctuation signal. The values of probe (h) are therefore divided by two (dashed line).

Sample Plasma measurement

To demonstrate the operation of the magnetic fluctuation probe, the "best-choice" probe design (g) - using the inner conductors of two semi-rigid $50\,\Omega$ coaxial cables with grounded shield - is introduced into the bulk of an rf produced helicon plasma in the VINETA experiment. Fig. 4.13 shows the probe measurements (bottom, solid line) recorded simultaneously with the antenna discharge current (top). A simple but crucial test for the $\dot{B}$-probe is rotating the probe by $180°$. A probe measuring only the inductive component should simply change the sign in the signal which is indeed the case. The small ($\lesssim 5\,\%$) difference in the two signal amplitudes is two times the remaining capacitive pickup signal amplitude. The excellent capacitive pickup rejection and the small spatial dimensions ($2.5\,\mathrm{mm}$ diameter) of the probes enables reliable, absolutely calibrated rf magnetic field measurements with high spatial resolution.

4.2.3 Laser Induced Fluorescence (LIF)

Laser Induced Fluorescence (LIF) is a non-intrusive method to measure the ion energy distribution function (IEDF) of the plasma [Stern and Johnsen III, 1975; Hill et al., 1983; Severn et al., 1998]. A simpler diagnostic tool for measuring the IEDF is the ion energy analyser [Hutchinson, 1987], but even in a miniaturised version [Conway et al., 1998] of $\approx 15\,\mathrm{mm}$ diameter it disturbs the plasma and is likely to be damaged in the stressing plasma conditions of a helicon discharge. Moreover, it has a poor energy resolution compared to LIF [DeNeef and Theiss, 1979; Donoso and Martin, 1990; Goeckner et al.,

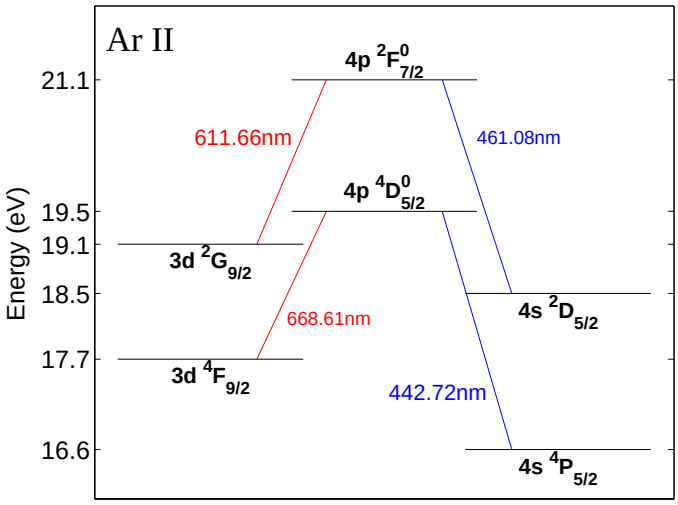

Figure 4.14: Transition schemes used for ArII LIF measurements with dye (top) and diode lasers (bottom). The schemes start from a metastable ion population into an excited state. The fluorescent decay is into a third state of lower energy than the previous metastable state.

1991]. Most LIF experiments use the resonant laser excitation of a metastable ion to a short-lived higher state. These excited atoms partially decay to a third state of lower energy than the previous metastable state, emitting a photon (induced fluorescence). In a thermalised plasma there are far less metastable ions than ions in the ground state. Excitation of ground state ions would therefore give a stronger LIF-signal, but the excitation energy is higher and requires UV-lasers [Tachibana, 2002] or the resonant absorption of two photons [Mazouffre et al., 2001; Amorim et al., 2000]. Two commonly used transition schemes for singly ionised argon are shown in Fig. 4.14 [Severn et al., 1998]. The excitation energy requires red lasers at 611.66 nm or 668.61 nm. The fluorescence signals are in the visible blue region at 461.08 nm and 442.72 nm. The first transition scheme would have higher oscillator strength, but this frequency is not yet available for laser diodes and can only be accessed with dye-laser systems.

Ions moving towards the direction of the incident laser beam with a velocity v are excited by a laser frequency that is shifted by $\Delta\nu$ with respect to the transition frequency due to the Doppler effect

$$\Delta\nu = v/\lambda\,. \tag{4.6}$$

Here, λ is the laser light wavelength. The laser is scanned over the resonance wavelength and the metastable atoms are excited selectively with respect to their velocity parallel to the laser beam. The laser line width, and with it the velocity component of excited metastable ions, is much smaller than the Doppler width of the IEDF (typically diode laser line width 10 MHz $\ll$ Doppler width 5 GHz). Other broadening mechanisms are usually small compared to the Doppler broadening, e.g. pressure broadening, Stark broadening or Stark splitting [Griem, 1997; Goeckner et al., 1991]. Only Zeeman splitting cannot be neglected. If the laser light is aligned perpendicular to the ambient magnetic field, the

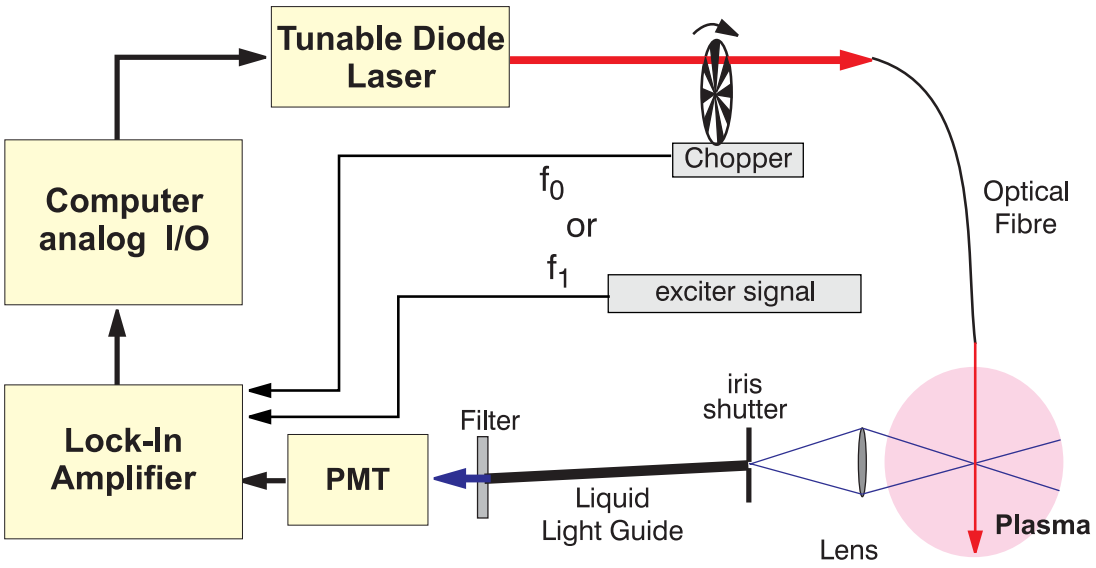

Figure 4.15: Simplified schematic of the LIF-setup at the VINETA experiment.

transverse Zeeman effect leads to a frequency shift of the σ-components by [Born, 1985]

$$\Delta\nu = eB/4\pi m_e \,. \tag{4.7}$$

The π-component remains unshifted.

A schematic of the LIF setup at the VINETA device is shown in Fig. 4.15. The laser light from the tuneable diode laser is coupled into a $50\,\mu$m optical fibre. At the device, the laser light from the fibre is collimated to the centre of experiment. Due to the anisotropy introduced by the magnetic field, the plasma thermalisation (collision processes and losses to the vessel boundary) is different for the direction perpendicular and parallel to the magnetic field. Consequently, the ion temperatures in perpendicular and parallel direction are different (usually $T_{i,\perp} > T_{i,\parallel}$ [Scime et al., 1998]). Depending on which temperature component one desires to measure, the laser beam has to be aligned parallel or perpendicular to the magnetic field. The pickup optics are focussed to the centre of the experiment on the same position as the laser beam, but the line of sight is aligned at a $90°$ angle to the laser beam. The fluorescent light from the intersecting focus positions is focussed onto an adjustable aperture to reduce light from other regions of the plasma before it enters a liquid light guide (fibre optics with large diameter and a high transmission coefficient) and is guided to a remote detection optic. The fluorescent light is passed through an optical bandpass filter ($2\,$nm optical width) to reduce unwanted light components before its intensity is measured with a photomultiplier tube. Besides the laser induced excitation, the ions are excited by inelastic collisions as well and a significant amount of spontaneous background light is the result. To discriminate between these two sources of fluorescence signal, the laser power is modulated with a chopper and the laser induced fluorescence signal is determined via a lock-in technique (see Sec. 4.3). An example measurement

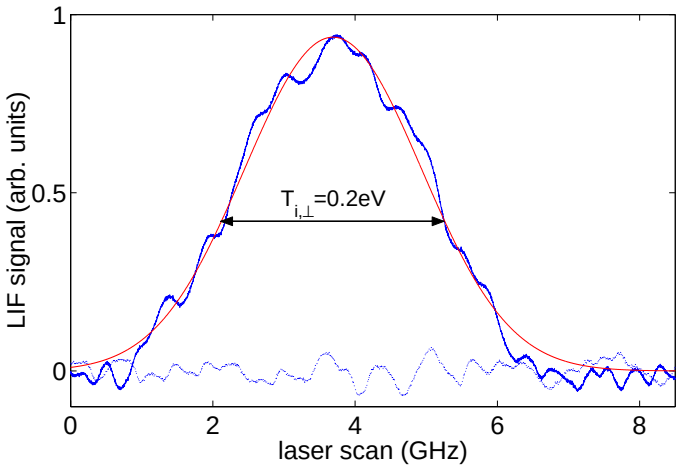

Figure 4.16: Example measurement of the IEDF perpendicular to the magnetic field (solid) and a reference measurement with the laser switched off (dotted). The laser light is unpolarised and the best fit (red) includes Zeeman correction. The ion temperature is determined to $T_{i,\perp} = 0.2\,\mathrm{eV}$.

of the IEDF in a VINETA helicon plasma with argon gas is shown in Fig. 4.16. It is taken with unpolarised laser light (the polarisation is lost in the multi-mode fibre) and is therefore fitted with three Gaussians, one at the centre resonance frequency and two shifted by the Zeeman splitting determined from Eq. (4.7). The resulting perpendicular ion temperature is $T_{i,\perp} = 0.2\,\mathrm{eV}$.

The number of the metastable ions excited by the laser, and thus the amplitude of the LIF signal, depends on both the metastable ion density and the laser light intensity [Goeckner et al., 1991]. The fraction of excited atoms that decay to the third state depends on the branching ratios of this particular transition scheme. The branching ratios are fixed with the choice of a LIF scheme (laser wavelength), the laser power provided by the used tunable laser (dye or diode), and the metastable density on the plasma parameters. These parameters are more or less fixed by technical requirements or resources. Other parameters improving the LIF signal-to-noise-ratio can be chosen freely. First, the collection optics and the laser optics have to be carefully aligned to exactly the same spatial position. Second, the aperture must be opened wide enough to ensure that all induced fluorescence light enters the liquid light guide but closed as far as possible to minimise the spontaneous fluorescence light entering the light guide from other parts of the plasma. Third, the signal-to-noise-ratio can be improved if the chopper is operated at a frequency where the fluctuations of the spontaneous emissions are minimal. Under typical discharge conditions in the VINETA experiment, large optical fluctuations of $1-2\,\mathrm{kHz}$ occurred. At $7\,\mathrm{kHz}$ in turn, these fluctuations are $\approx 14\,\mathrm{dB}$ less and the chopper was therefore operated at that frequency. And, last but not least, the photomultiplier tube should be operated at a voltage not too close to saturation to ensure maximum fluctuation of the small induced signal on top of the large background signal.

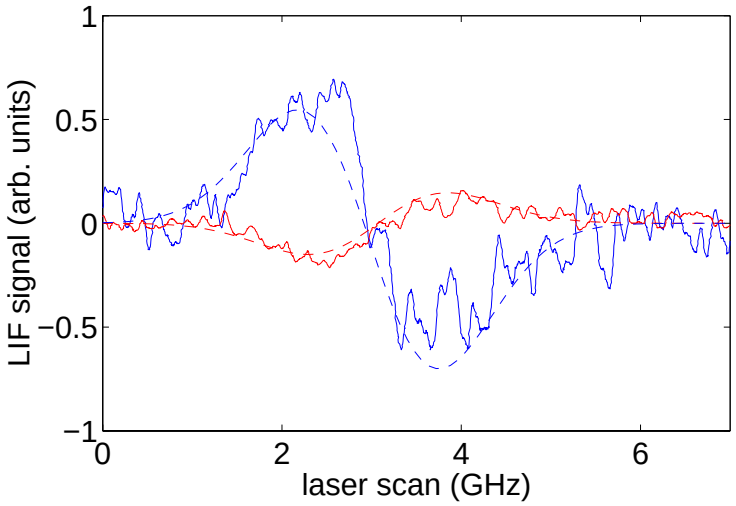

Figure 4.17: Example f_1 measurement (solid lines) at the wave excitation frequency $f_{ex} = 85\,\mathrm{kHz}$. The fits (dashed lines) to the real (blue) and imaginary (red) part resulted in $k_\perp = 17\,\mathrm{m}^{-1}$ and $k_\parallel = 45\,\mathrm{m}^{-1}$. The two ion temperature $T_{i,\perp} = 0.1\,\mathrm{eV}$ and $T_{i,\parallel} = 0.4\,\mathrm{eV}$ have been determined from independent f_0 measurements.

4.2.4 Wave Field Measurement with LIF

The LIF method yields a time-averaged measurement of the IEDF. A wave propagating through the plasma disturbs this distribution function on the timescale of the wave frequency. With only a slight change in the LIF setup it is also possible to determine the parameters of such a perturbing wave. Wave vector, wave amplitude and phase, as well as effective wave damping can be derived from a local measurement of the perturbed IEDF [Skiff and Anderegg, 1987]. Instead of chopping the laser beam and using this as the reference frequency for the lock-in amplifier, the perturbing wave frequency is taken as reference signal (compare Fig. 4.15). The resulting measurement is now the perturbed ion distribution function caused by the reference wave. The underlying idea of this method is that the perturbation of the particle distribution function at the point of observation is linked to all other points in space that lie on the trajectory of the particles. The particles carry the perturbing wave information along their trajectory to the point of measurement. This holds ideally true only for collisionless plasmas but can be applied in weakly collisional plasmas. The usefulness of this method was successfully demonstrated for electrostatic waves by Skiff and Anderegg [1987]; Skiff [1992] and Sarfaty et al. [1996] but can be extended to electromagnetic waves as well [Skiff, 1992; Kline et al., 2000]. The theoretical derivation of the mathematical expression for the perturbed ion distribution function is rather lengthy and just briefly summarised in what follows. In the picture proposed by Vlasov, the plasma is described by a distribution function $f(\boldsymbol{r}, \boldsymbol{v}, t)$ in the seven-dimensional space spanned by position, velocity, and time [Nicholson, 1983]. For only small perturbations of the distribution function, it is suitable to write $f = f_0 + f_1$. Within the framework of the experimental measurements presented in this section, the

perturbed ion distribution function f_1 is calculated by integrating the influence of the perturbing wave field $\boldsymbol{E}_1$ on the background ion distribution f_0 along the unperturbed particle orbits $\boldsymbol{r'}$

$$f_1(\boldsymbol{r},\boldsymbol{v},t) = -\frac{q}{M}\int_{-\infty}^{t} \boldsymbol{E}_1(\boldsymbol{r'}(t'),t')\nabla_v f_0 \mathrm{d}t' \,. \tag{4.8}$$

In a magnetised plasma it is appropriate to model f_0 by a Maxwellian with two temperatures for the directions parallel and perpendicular to the magnetic field. The resulting perturbed IEDF $f_1 = f_1(\boldsymbol{v})$ is a function of all three velocity components. The measurements are done in only one direction, say, perpendicular to the magnetic field in v_y. To meet that situation, $f_1(\boldsymbol{v})$ is integrated over the two other velocity components and the formula for the perturbed ion velocity distribution function perpendicular to the magnetic field reads [Sarfaty et al., 1996]

$$\begin{aligned} f_1(v_y) \;=\; & \int_{-\infty}^{\infty}\mathrm{d}v_x \int_{-\infty}^{\infty}\mathrm{d}v_z f_1(\boldsymbol{v}) = \\ & \left(\frac{-e\Phi_1}{\pi M v_{th,\parallel}}\right) f_0(v_y) \sum_{n,m}\left(1 + Z(\zeta_{n+m})\left(\zeta_0\frac{T_\parallel}{T_\perp} + \left(1-\frac{T_\parallel}{T_\perp}\right)\zeta_{n+m}\right)\right) \\ & \times J_m(k_\perp v_y/\omega_{ci}) e^{\mathrm{i}m\pi/2} e^{\mathrm{i}(m+n)\theta} e^{\mathrm{i}k_x v_y/\omega_{ci}} e^{-a^2/8} e^{-c^2/4} \\ & \times \sum_k I_{(n+k)/2}\left(\frac{a^2}{8}\right) I_k\left(\frac{ac}{2}\right) e^{\mathrm{i}k\pi/2} \,, \end{aligned} \tag{4.9}$$

with,

$$a = \sqrt{2}k_\perp v_{th,\perp}/\omega_{ci} \,,$$

$$c = \sqrt{2}k_y v_{th,\perp}/\omega_{ci} = a\sin\theta \,,$$

$$\zeta_n = (\omega_{eff} - n\omega_{ci} - k_\parallel v_o)/\sqrt{2}k_\parallel v_{th,\parallel} \,.$$

Z the plasma dispersion function [Fried and Conte, 1961], and $\theta = \tan^{-1} k_y/k_x$ the wave vector angle in the laboratory (x,y)-plane perpendicular to the ambient magnetic field. The Bessel functions J and I result from the cylindrical geometry of the problem.

An example measurement of the perturbed ion distribution function, which we made in the HELIX-experiment [Balkey et al., 2001] during my research stay at West-Virginia-University, is shown in Fig. 4.17 (solid lines). For this measurement, a second antenna driven with $200\,\mathrm{W}$ at $85\,\mathrm{kHz}$ excited a wave in a helicon plasma. The fit of Eq. (4.9) to the measurement resulted in $k_\parallel = 45\,\mathrm{m}^{-1}$ and $k_\perp = 17\,\mathrm{m}^{-1}$. It was proposed to use this technique to measure the wave field of a helicon wave [Franck et al., 2000]. This is in principle possible as the measured f_1 signal is frequency limited only by the lifetime of the metastable transition ($7\,\mathrm{ns} \mathrel{\hat{=}} 140\,\mathrm{MHz}$), but naturally the perturbed ion response is weaker with increasing wave frequency. This method is successfully tested and is proposed to be used for non-intrusive measurements of low-frequency waves where $\dot{B}$-probes show significant deficits (cf. Sec. 5.2).

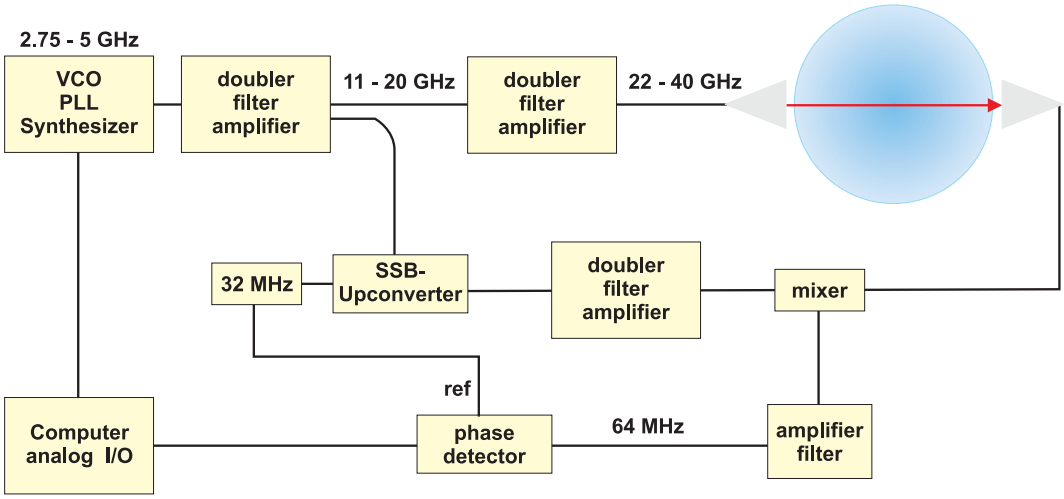

Figure 4.18: Schematic of the heterodyne microwave interferometer setup installed at the VINETA experiment. The microwave signal can be operated at $f_{\rm hf} = 22$–$40\,$GHz. The phase delay of the signal through the plasma is compared to a reference signal. To improve the phase measurement, the signal is down-converted to $64\,$MHz.

4.2.5 Microwave Interferometer

The microwave interferometer technique is a non-intrusive diagnostic tool to measure the line integrated plasma density [Hartfußet al., 1997]. Together with relative plasma density profiles along the line of sight, e.g. using Langmuir probe measurements, or by tomographic reconstruction of interferometer measurements along many paths, the absolute plasma density profile can be determined with high accuracy. The basic physical principle can be understood from the dispersive nature of the plasma. The refractive index n of an ordinary wave (cf. Sec. 2.3.1) is given by Eq. (2.36)

$$n = kc/\omega = [1 - (f_{pe}/f)^2]^{1/2} = [1 - n/n_{co}]^{1/2}\,. \tag{4.10}$$

The cut-off density n_{co} for a given frequency f is defined by $n_{co} = (2\pi f/e)^2\epsilon_0 m_e$. The wave propagates only for frequencies above the plasma frequency. For large frequencies $f \gg f_{pe}$ the refractive index can be approximated by Taylor series expansion

$$n = (1 - n/n_{co})^{1/2} \approx 1 - n/2n_{co}\,. \tag{4.11}$$

Suppose a wave propagating through a plasma with density profile $n(x)$. The phase of the wave is $(kx - \omega t)$ and the phase shift between the case with and without plasma can be expressed as

$$\begin{aligned} \Delta\varphi &= \int (d\varphi_{plas} - d\varphi_{vac}) = \int (k_{plas} - k_{vac})dx \\ &= \frac{2\pi}{\lambda}\int (n(x) - 1)dx \approx \frac{\pi}{\lambda n_{co}}\int n(x)dx\,. \end{aligned} \tag{4.12}$$

Thus, the plasma introduces a phase shift $\Delta\varphi$ that is proportional to the line integrated density $\int n(x)dx$ along the path of propagation. The choice of wavelength is very important. If the frequency is too small, the wave is refracted at density gradients or even reflected at a cut-off. On the contrary, the phase shift is inverse proportional to the wave frequency. Usually, a frequency 5–10 times larger than the cut-off frequency is chosen. Fig. 4.18 shows a schematic of the interferometer setup [Vowinkel, 2000] at the VINETA. The probing hf wave frequency $f_{\mathrm{hf}} = 22$–$40\,\mathrm{GHz}$ is generated from a tuneable voltage controlled phase-locked loop oscillator with $f = 2.75$–$5\,\mathrm{GHz}$ by multiple frequency doubling and subsequent amplification and filtering. Phase shifts in a high frequency signal in the GHz-range are difficult to measure. A heterodyne technique is therefore applied, which up-converts the hf signal with the $32\,\mathrm{MHz}$ signal of a local oscillator (lo) by single-sideband (ssb) modulation. The mixer in the ssb up-converter is phase preserving

$$\begin{aligned}\sin(\omega_{\mathrm{hf}}t + \varphi_{\mathrm{hf}}) \cdot \sin(\omega_{lo}t) &= 1/2\cos([\omega_{\mathrm{hf}} - \omega_{lo}]t + \varphi_{\mathrm{hf}}) \\ &\quad +1/2\cos([\omega_{\mathrm{hf}} + \omega_{lo}]t + \varphi_{\mathrm{hf}}) \qquad (4.13)\end{aligned}$$

and the sharp bandpass filter leaves only the upper sideband. A second mixer multiplies the so-obtained reference signal and the signal that passed through the plasma. A high accuracy phase detector is applied to the resulting low frequency signal and yields a voltage proportional to the line-integrated density [cf. Eq. (4.12)]. The maximum time resolution of the phase detection is 2μs. The interferometer can be operated at a single frequency or swept over the frequency range.

4.3 Signal Analysis

Wave field experiments require spatio-temporal measurements of the amplitude and the phase of the wave. The temporal evolution is easily monitored by using fast digitisers or oscilloscopes. The spatial distribution can either be determined by a simultaneous measurement of several probes or by subsequent measurements of a positionable single probe. The first approach involves several digitisers and disturbs the plasma more than a single probe. For the experiments in this work, a single probe in connection with two two-dimensional positioning systems is used (see Sec. 4.4). The subsequent measurements of the single probe have to be related to a time origin, especially with respect to the relative phase information. A reference signal is therefore recorded from a fixed probe or from the wave exciting antenna current or voltage. For spatially stationary wave fields with a good signal-to-noise-ratio, the amplitudes and phases can be derived digitally from the sampled time series using cross-spectral density estimation [Priestley, 1989; Pécseli, 2000]. Averaging improves the signal-to-noise-ratio. For signals that drift in frequency over the measuring period or with a signal-to-noise-ratio below 10^{-3}–10^{-4}, the lock-in technique can be used. This involves either lock-in amplifiers, or very long time-series with high amplitude resolution have to be recorded and evaluated digitally afterwards. Both techniques, the cross spectral density and the lock-in detection, are used for the experiments within this thesis and explained in the following.

4.3.1 Cross Power Spectrum

The cross-power-spectral density [Priestley, 1989; Smith et al., 1974; Beall et al., 1982] of a measured signal $\phi_s(t)$ and a reference signal $\phi_r(t)$ is defined as the product of the Fourier transforms $\hat{\Phi}$ of the signals

$$P_\times(f) = \hat{\Phi}_r^\star(f)\hat{\Phi}_s(f)\,. \tag{4.14}$$

The relative phase difference Θ and the relative amplitude A of the two signals at frequency f_0 can be derived from the cross-power-spectral density as

$$A = |P_\times(f_0)|\,, \qquad \tan\Theta = \frac{\mathrm{Im}P_\times(f_0)}{\mathrm{Re}P_\times(f_0)}\,. \tag{4.15}$$

This method is only applicable to fluctuations if the phase and frequency are constant during the time of measurement. The Fourier transform of signals with drifting frequency has a broadened spectrum and the cross-spectral density is therefore erroneous.

From the cross spectrum, the wavelength of an axially propagating wave can be determined. The Fourier transform of the wave signal $\phi_s(z,t) = S_0 \exp i(k_\parallel z - \omega_0 t + \phi_s)$ and the reference signal $\phi_r(t) = R_0 \exp i(-\omega_0 t + \phi_r)$ at the wave frequency ω_0 are: $\hat{\Phi}_r^\star(\omega_0) = R_0 \exp\phi_r$ and $\hat{\Phi}_s^\star(\omega_0, z) = S_0 \exp \mathrm{i}(k_\parallel z - \phi_s)$. The phase is determined ac-

cording to Eq. (4.15) to $\Theta = k_\parallel z + \phi_s - \phi_r$. From the axial derivative of the phase information, the parallel wave vector is calculated to be $\partial\Theta/\partial z = k_\parallel$.

4.3.2 Lock-In Detection

The lock-in technique [Horowitz and Hill, 1989; SR830] basically involves the multiplication of a reference signal $U_r \sin(\omega_r t + \theta_r)$ with a measured signal, say $U_s \sin(\omega_s t + \theta_s)$. The product U of the two signals is a superposition of signals at the sum and the difference frequency

$$U = \quad 1/2 U_s U_r \cos([\omega_r - \omega_s]t + \theta_r - \theta_s) \tag{4.16}$$

$$-1/2 U_s U_r \cos([\omega_r + \omega_s]t + \theta_r + \theta_s)\,. \tag{4.17}$$

If the two frequencies match, $\omega_s = \omega_r$, the multiplied signal U contains a dc-component at the output

$$U_{\mathrm{dc}} = 1/2 U_r U_s \cos(\theta_s - \theta_r)\,. \tag{4.18}$$

All other frequency components can be removed with a steep low-pass filter. A good reference signal is therefore essential, i.e. one must have a pure sinusoidal signal with constant phase at exactly the measured signal frequency. Lock-in amplifiers circumvent problems that are due to reference signals with drifting frequency by generating an internal sinusoidal reference signal that is phase-locked to the instantaneous applied external reference signal frequency. Modern lock-in amplifiers generate two internal phase locked signals with a phase difference of $\pi/2$ between each other. Both are multiplied with the measured signal, and the two low-pass filtered outputs result in

$$X = U_s \sin\theta_s \qquad Y = U_s \cos\theta_s\,. \tag{4.19}$$

Without loss of generality, it was assumed that $\theta_r = 0$ and $U_r = 1$. The amplitude U_s and phase θ_s of the measured signal are calculated from

$$U_s = \left(X^2 + Y^2\right)^{1/2} \qquad \theta_s = \tan^{-1}(Y/X)\,. \tag{4.20}$$

Again, the parallel wave vector can be determined from the phase information at different axial positions as was shown in the previous Sec. 4.3.1.

4.3.3 Wavelength Measurements

To obtain the dispersion relation $\lambda(\omega)$ of a wave experimentally, waves are excited with different frequencies. Their respective wavelength is determined from wave field measurements at different distances to the exciter antenna. A typical measurement of the spatiotemporal evolution of a whistler wave at a frequency of $250\,\mathrm{MHz}$ is shown in Fig. 4.19.

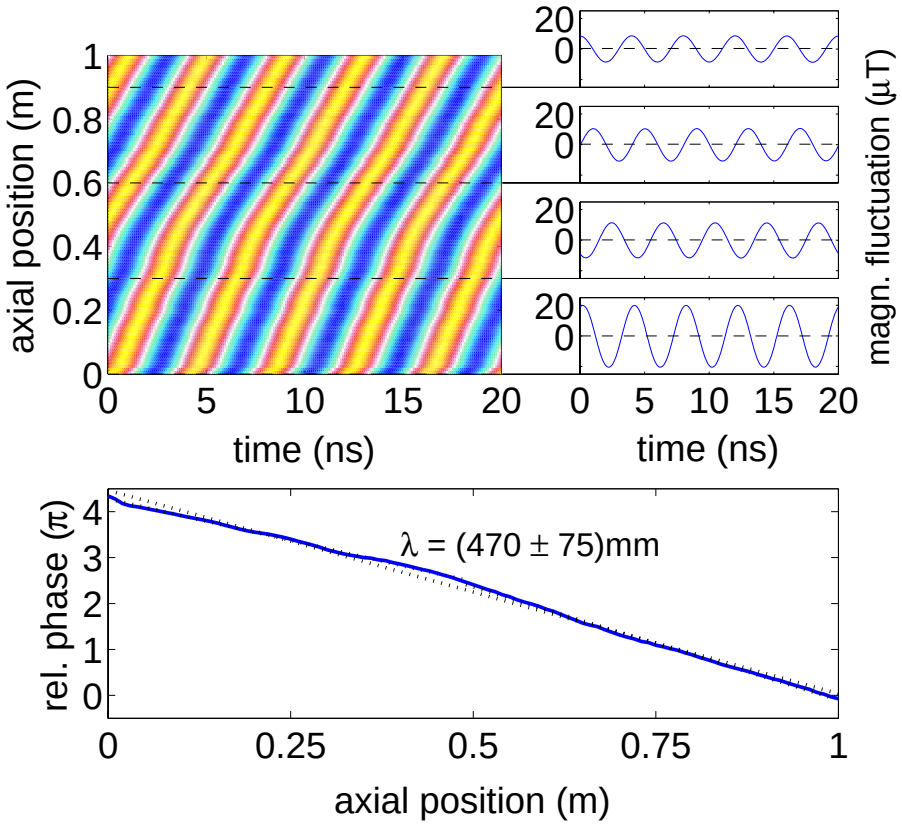

Figure 4.19: Typical spatiotemporal measurement of the propagation of a whistler wave with $250\,\mathrm{MHz}$. The wave amplitude in the colour-coded representation (top left) is normalised to its standard deviation. Four example time series at $z = 0$, 300, 600, and $900\,\mathrm{mm}$ show the propagation and the damping of the wave (top right). From the relative phase at each position (bottom), the wavelength is determined to $(470 \pm 75)\,\mathrm{mm}$.

On the left-hand side, the amplitude of the receiver signal is shown for increasing axial position. The amplitude is normalised to its standard deviation for better visual presentation and depicted as a colour-coded plot. The recording of the time series is triggered by the exciter signal in order to keep the relative phase between the magnetic fluctuations and the driver signal fixed. The observed $\dot{B}$-signal undergoes a clear and unique phase shift if followed in axial direction. Such a sloped stripe pattern is typical for propagating waves. Also shown in Fig. 4.19 (top right) are the non-normalised magnetic fluctuations at four different axial positions. Besides the phase shift, a damping of the wave is observed. The relative phase and amplitude for each axial position are determined by the cross-spectral density or the lock-in technique, as introduced in the previous sections. In the bottom graph of Fig. 4.19, the relative phase is shown as a function of the axial position (blue solid line). From the linear best fits (dotted lines) to the entire set of measurements, the wavelength is determined to be $\lambda_\parallel = (470 \pm 75)\,\mathrm{mm}$.

4.4 Experimental Setup

The experiments on whistler waves presented in this thesis can be distinguished in two parts. For the investigations of *helicon waves* excited by the external antenna, the principal experimental setup is shown in Fig. 4.20. The plasma is generated by a helicon antenna which is driven by an rf source in the frequency range 3–30 MHz with rf powers up to 6 kW. The rf power is matched to the antenna with two variable capacitors in standard L-matching configuration [Rayner et al., 1996]. A current monitor measures the rf antenna currents which is mostly used as a reference signal for the wave analysis. The magnetic fluctuations from the waves generated by the rf plasma source are measured with three $\dot{B}$-probes arranged perpendicular to each other (cf. Sec. 4.2.2). The measured signals are usually quite large and need no further amplification but are bandpass filtered to remove unwanted higher harmonics. The wave amplitude and phase with respect to the rf current signal are determined at each spatial position using a lock-in amplifier (cf. Sec. 4.3.2). The wave propagation and modestructure are not only analysed in the perpendicular plane but also in the horizontal parallel plane, using both two-dimensional positioning systems.

For investigations of *whistler waves*, a separate excitation setup is applied, based on a loop antenna inserted into the plasma. The loop antenna is fed with the amplified signal from an hf source that is matched with a stub tuner as shown schematically in Fig. 4.21. As the frequencies ($f = 100$–800 MHz) are usually too high for conventional current monitors, the voltage signal applied to the antenna is usually taken directly as the refer-

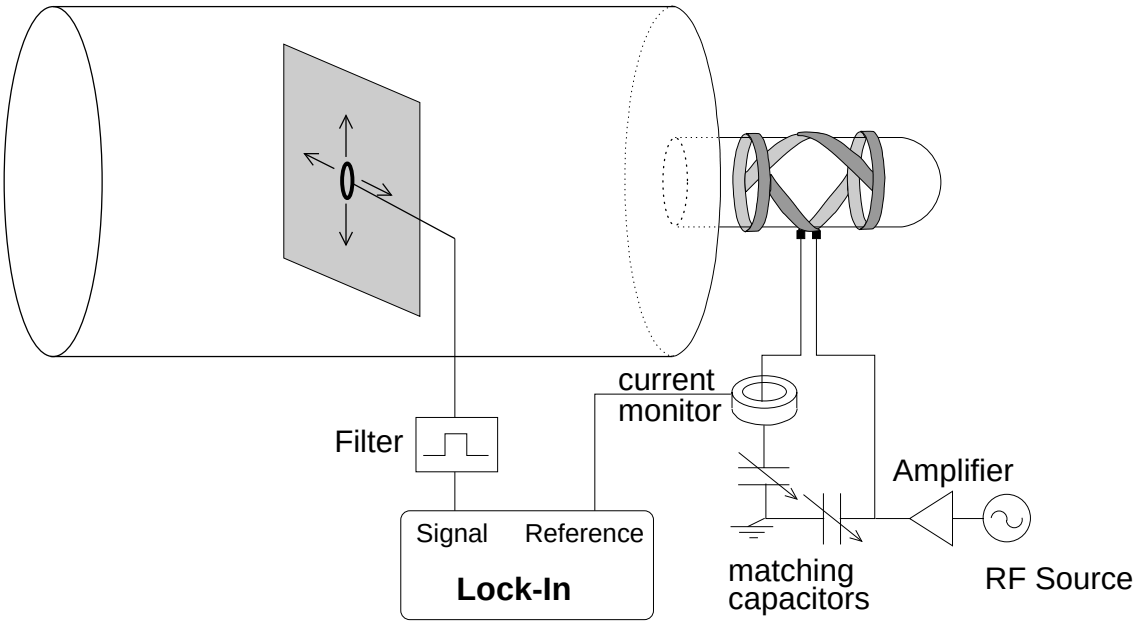

Figure 4.20: Schematic of the setup for experiments analysing the poloidal modestructure of the waves excited by the rf source. A two-dimensional positioning system enables the probe positioning in a rectangular plane perpendicular to the axial magnetic field with ≈ 250 mm horizontal and ≈ 200 mm vertical dimension.

ence signal. The magnetic fluctuations associated with the launched waves are measured with $\dot{B}$-probes and the fluctuation signal is again bandpass filtered; this time primarily to remove the rf plasma source signal. As the exciter signal amplitude is kept below $\approx 1\,\mathrm{W}$ to minimise the plasma disturbance, and the detected signals are amplified. At these high frequencies, there are no lock-in amplifiers available and the measured signals are digitised simultaneously with the reference signal. The wave amplitude and phase are obtained digitally by the cross-power-spectral density analysis (cf. Sec. 4.3.1).

The actual excitation mechanism of whistler waves by loop antennae is schematically depicted in Fig. 4.22, following Stenzel et al. [1993]. The rising current $I(t)$ during the first half of a current cycle induces an azimuthal electric field E_i, which is antiparallel to the current in the plasma. As the associated timescale is too fast for the ions to follow ($\omega \gg \omega_{ci}, \omega_{pi}$), only the electrons respond to this electric field by drifting radially inwards with the $E \times B$-velocity $v_{E\times B} = E_i/B_0$. A surplus of negative charge accumulates inside the loop and a surplus positive charge remains outside. This space charge produces a radial electric field E_{sc}, which in turn causes the electrons to drift azimuthally and generate a current $J_\theta = -neE_{sc}/B_0$. This current is in opposite direction to the antenna current and produces the axial magnetic wave field component B_z, which can be measured with $\dot{B}$-probes. Naturally, the surplus space charge is nonuniform along the magnetic field B_0 as the induced electric field E_i decreases with increasing distance to the loop antenna. This gives rise to an axial current J_z, which is in opposite direction inside and outside the loop. As before, the current J_θ induces an electric field but now in opposite direction

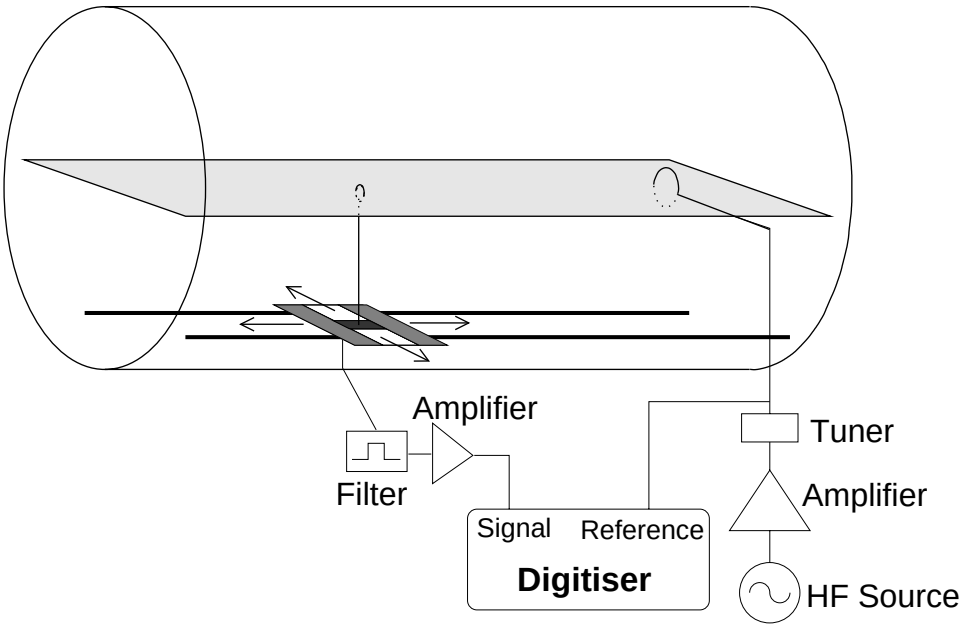

Figure 4.21: Schematic of the setup for experiments analysing the propagation behaviour of waves excited by a small loop antenna. A two-dimensional positioning system allows one to do measurements in a rectangular horizontal plane parallel to the axial magnetic field with $\approx 3000\,\mathrm{mm}$ axial and $\approx 200\,\mathrm{mm}$ radial dimension.

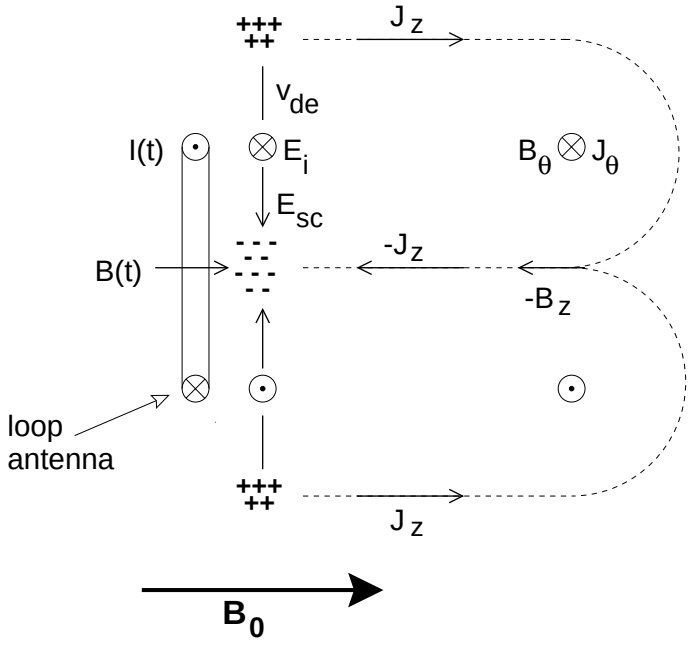

Figure 4.22: Schematic of the currents, fields and drifts associated with the wave excitation in a linear magnetised plasma (adapted from Stenzel et al. [1993]).

with respect to the antenna and the drifting space charge (now in the opposite direction) closes the current path across the magnetic field at the wave front. For the second half of the current cycle, for decreasing current, all induced fields, currents and space charges change their sign.

5

Basic Wave Experiments

Since their first observation in the late 19th century and their explanation by Barkhausen [1930] and Eckersley [1935], ionospheric whistler waves have been intensely studied (see review articles by Al'pert [1980] and Stenzel [1999]). The first laboratory study followed in the 1960's with the experiments from Gallet et al. [1960]. Many subsequent laboratory experiments investigated various aspects of the wave propagation such as excitation, dispersion, damping, and ducting, to name only a few. Laboratory plasmas are naturally always bounded and the wave dispersion is consequently altered. Most commonly, large laboratory plasma devices are used to minimise finite size effects [Stenzel, 1976; Mattoo et al., 2001; Stenzel I-IX]. So far, the influence of the plasma boundary on the wave propagation was treated only theoretically [Klozenberg et al., 1965; Uhm et al., 1988]. In Sec. 5.1 the basic whistler wave dispersion is measured under conditions where the boundary is expected to play only a minor role and compared to the theory described in Sec. 2.3.3. In Sec. 5.2 the first laboratory experiments on ion whistler waves are reported. We note that ion whistler wave have been only studied in ionospheric plasmas so far. In contrast to electron whistler waves, the influence of the plasma boundary on the ion whistler wave propagation has not yet been addressed, neither theoretically nor experimentally. Therefore, the infinite plasma dispersion theory derived in Sec. 2.3.4 is used for comparison in these first reports. Although their large wavelengths indicate that the boundary would most likely have to be considered in a correct analysis there is still a good qualitative agreement between simple theory and observation.

5.1 Whistler Waves

Whistler waves are excited by an exciter loop antenna which is positioned centrally into the VINETA experiment. The antenna is made of two windings of copper wire with a diameter of $30\,\mathrm{mm}$ and is shielded from the plasma with ceramics. The loop ends are connected to the inner and outer conductor of a semi rigid-cable to ensure a wave excitation at the loop only and to minimise magnetic fluctuations excited from the support. The exciter antenna is supplied with sinusoidal currents of frequencies in the range of $f_{ex} = 100\text{–}800\,\mathrm{MHz}$. The high frequency generator output signal is amplified and

impedance matched to the antenna by a triple stub tuner. The maximum power of the driver signal is kept below $1\,\mathrm{W}$ to ensure only weak plasma disturbance. The whistler waves are detected by a set of three orthogonal $\dot{B}$-probes. They are movable in the direction parallel to the magnetic field, carefully compensated for electrostatic pickup, and absolutely calibrated (see Sec. 4.2.2). From the measured axial wave field, the wavelength is determined by the cross-power-spectral density analysis (cf. Secs. 4.3.1 and 4.3.3). A dispersion relation $\lambda_{\|}(\omega)$ is obtained by measuring the wavelength at a number of different excitation frequencies. Besides determining the wavelength from the phase information, it is possible to estimate wave damping and polarisation from the amplitude information in the cross spectrum. A typical axial evolution of the wave amplitude is shown in Fig. 5.1 for the two components perpendicular to the axial magnetic field ($\dot{B}_x$, $\dot{B}_y$). The $\dot{B}_y$ signal has a maximum at those axial positions where $\dot{B}_x$ has a minimum and vice versa. This is a clear indication of a circular polarised wave and proves that indeed an R-wave is excited.

Fig. 5.2 shows the first set of dispersion measurements performed under two different sets of plasma conditions, for which the influence of the plasma boundary is only small. The theoretical analysis of Sec 2.4 showed that the boundary effects are less the smaller the wavelength to chamber size ratio is. Moreover, the wavelength decreases for increasing frequencies, increasing plasma densities, and decreasing magnetic fields. The waves are therefore excited in a high density plasma in helicon and inductive mode operation. The plasma density and electron temperature are derived from Langmuir probe characteristics [Demidov et al., 1999] and the magnetic field is measured with a calibrated Hall sensor. The first set of measurements was done in a helicon plasma with peak density $n = 3.3 \cdot 10^{18}\,\mathrm{m}^{-3}$ and electron temperature $T_e = 2$–$5\,\mathrm{eV}$ at an ambient magnetic field strength $B_0 = 56\,\mathrm{mT}$ (top Fig. 5.2). The measured wavelengths are below $50\,\mathrm{mm}$ and increase with decreasing frequency. The measurements are highly reproducible and the errorbars are usually smaller than the marker size. For comparison, the whistler wave dispersion (2.42) for unbounded plasmas is plotted in the diagram (solid line) based on the independently measured parameters $n = 3.3 \cdot 10^{18}\,\mathrm{m}^{-3}$ and $B_0 = 56\,\mathrm{mT}$ without

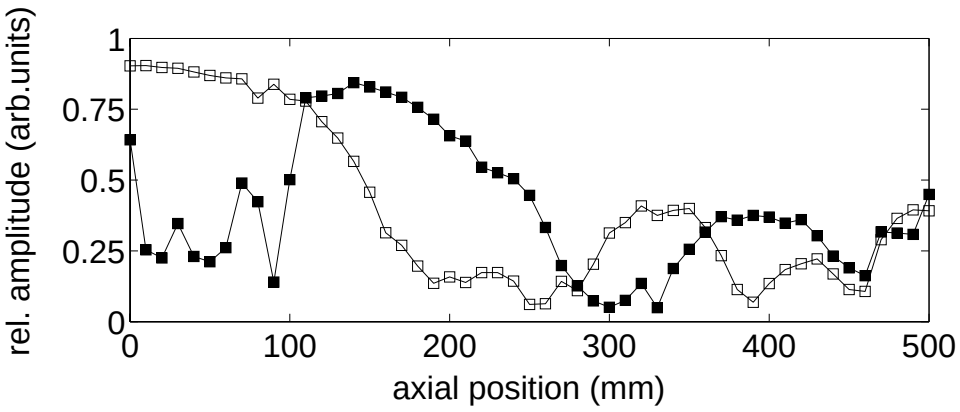

Figure 5.1: Relative amplitudes of the two signal components [$\dot{B}_x(\square)$, $\dot{B}_y(\blacksquare)$] along the axial direction z.

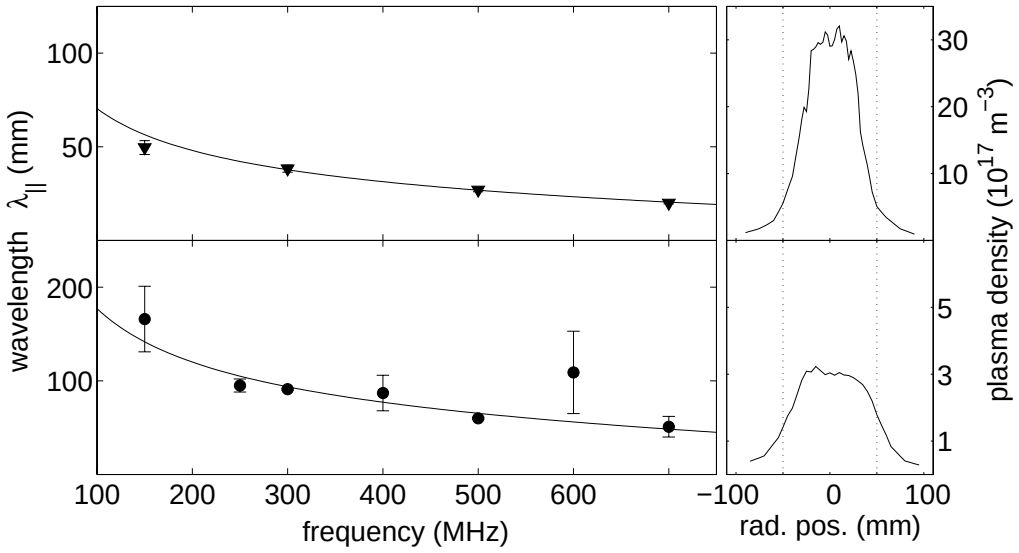

Figure 5.2: Whistler wave dispersion measurements in a helicon mode discharge (top, $n = 3.3 \cdot 10^{18}\,\mathrm{m}^{-3}$, $B_0 = 56\,\mathrm{mT}$) and in an inductive mode discharge (bottom, $n = 4.5 \cdot 10^{17}\,\mathrm{m}^{-3}$, $B_0 = 49\,\mathrm{mT}$). Shown are the measured data points (markers) and the theoretical curve for wave dispersion in unbounded plasmas (solid lines). On the right-hand side, the relative plasma profiles of the two discharge modes measured by Langmuir probes are shown.

any free fit parameter. The measurements are in very good agreement with the whistler wave theory for unbounded plasmas. A second set of measurements was done in the inductive mode plasma with lower plasma density $n = 4.5 \cdot 10^{17}\,\mathrm{m}^{-3}$ and $B_0 = 49\,\mathrm{mT}$ (bottom of Fig. 5.2). The wavelength decreases with increasing excitation frequency and the wavelengths are below $200\,\mathrm{mm}$. Again, the measurements are highly accurate and reproducible, except only the measured value at $600\,\mathrm{MHz}$. The wavelengths are larger than in the previous case of higher plasma density, but again, the dispersion is well described by whistler wave propagation in unbounded plasma geometry (solid line). The radial profiles of the relative plasma density are shown on the right-hand side of Fig. 5.2 with peak density of $n = 3.3 \cdot 10^{18}\,\mathrm{m}^{-3}$ in the helicon mode and $n = 4.5 \cdot 10^{17}\,\mathrm{m}^{-3}$ in the inductive mode. The dotted lines indicate the radial positions of the helicon antenna edge. The plasma density profiles show the typical centre peaked density maximum in the helicon mode and an almost flat-top profile inside the entire antenna region in the inductive mode (cf. Sec. 6.1). The measurements presented in these cases agree reasonably well with the whistler wave dispersion in unbounded plasmas. The measured parallel wavelengths are smaller than the perpendicular experimental dimensions ($\lambda_{\|} \leq R_c = 0.2\,\mathrm{m}$) and boundary effects play only a minor role in the wave propagation.

5.2 Ion Whistler Waves

With essentially the same experimental setup as described in the previous section, waves are excited at frequencies around the ion cyclotron frequency. As the wave excitation as

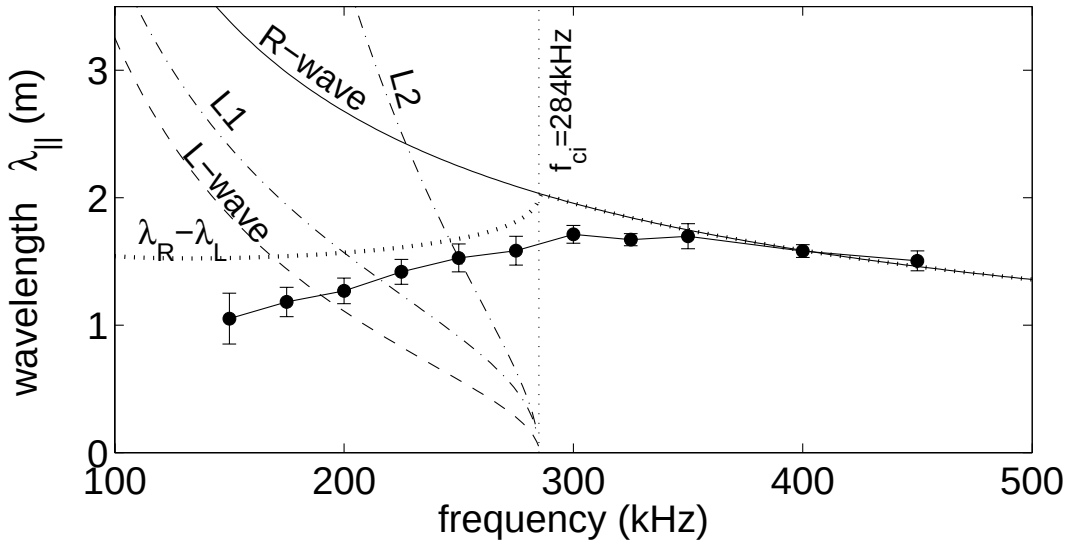

Figure 5.3: Ion whistler wave dispersion measurements in a helicon mode discharge in helium ($n = 4 \cdot 10^{18}\,\mathrm{m}^{-3}$, $B_0 = 75\,\mathrm{mT}$). Shown are the measurements (markers) and the theoretical dispersion for a R-wave (solid line) and a L-wave (dashed line). The dash-dotted lines represent the two solutions of the simple superposition of the waves ($L1, L2 = 2\pi/(k_L \pm k_R)$) and the dotted curve is the difference wavelength ($\lambda_R - \lambda_L$).

well as the detection are proportional to the frequency ($U_{ind} \propto f$, cf. Sec. 4.2.2), helium is chosen as a working gas for the experiments in this section ($f_{c,He} = 10 f_{c,Ar}$). The plasma parameters of this helium helicon discharge are $B_0 = 75\,\mathrm{mT}$, $p = 2.5\,\mathrm{Pa}$, $P_{\mathrm{rf}} = 5\,\mathrm{kW}$, $n \approx 4 \cdot 10^{18}\,\mathrm{m}^{-3}$, and $T_e \approx 5\,\mathrm{eV}$. To ensure reliable measurements with magnetic fluctuation probes even at such low frequencies in the range of 150–$450\,\mathrm{kHz}$, the exciter loop antenna is fed with a sinusoidal signal of $P = 50\,\mathrm{W}$ and the $\dot{B}$-probe loop consists of 25 windings of teflon insulated copper wire with a diameter of $25\,\mathrm{mm}$. For capacitive pickup rejection, the probe leads are connected to an active differential amplifier instead of a centre-tapped (high frequency) transformer. The rest of the experimental setup and the data evaluation technique remain the same. Fig. 5.3 shows the measurements of the wave dispersion (markers). The increasing errorbars at small frequencies are related to the above mentioned problems of wave excitation and detection. The vertical dotted line at $f_{c,He} = 284\,\mathrm{kHz}$ indicates the ion cyclotron frequency. For increasing exciter frequencies above $f_{c,He}$, the measured wavelengths decrease. Such a quantitative behaviour was observed already in the previous set of experiments (Sec. 5.1) and the measurements agree reasonably well with the conventional R-wave dispersion (solid line), calculated for the present set of plasma parameters. The situation completely changes for frequencies below $f_{c,Ar}$. Here, the measured wavelength decreases with decreasing frequency. This cannot be explained by the L-wave or the R-wave dispersion, which are plotted dashed and solid in Fig. 5.3. (Note that the excitation scheme does not prescribe a polarisation direction.) The exciter antenna is not designed to excite only one wave component, the excitation mechanism presented (Sec. 4.4) excites both R-wave and L-wave. And so is the measuring $\dot{B}$-probe; it is sensitive to magnetic fluctuations only and measures both

wave modes with different circular polarisation. For this reason, it is suggested that the measured wavelengths are results from a combination of both waves which could propagate below f_{ci}. The observed wavelengths cannot be explained from linear superposition alone:

$$\sin(k_R z) + \sin(k_L z) = 2\sin\left(\frac{k_R + k_L}{2} z\right)\cos\left(\frac{k_R - k_L}{2} z\right) . \tag{5.1}$$

The wavelengths from both dispersion curves, $L_1 = 2\pi/(k_L + k_R)$ and $L_2 = 2\pi/(k_L - k_R)$ are plotted dash-dotted in Fig. 5.3. The measurements do not match this behaviour, and especially, there is no wavelength jump observed at $\omega_{c,He}$. A more reasonable agreement between theory and measurement is seen if compared to the difference wavelength ($\lambda_R - \lambda_L$, dotted line). So far, this well-matching comparison is only heuristic but will be analysed in detail in future investigations. To our knowledge, this is the first experimental evidence of L-wave propagation in laboratory plasmas [Franck et al., 2002a], but for a complete treatment, the finite size effects of the plasma and the antenna excitation as well as wave damping effect will have to be taken into account, especially around the resonance frequency.

6

Helicon Wave Experiments

In this chapter, the other extreme of boundary condition in R-wave dispersion is considered. Having studied wave propagation in infinite plasma geometry in the previous chapter, strongly bounded waves are investigated in this chapter. The rf helicon source produces a plasma and excites propagating waves at the driving frequency. As reviewed in Chap. 3, the standard rf helicon source can be operated in three qualitatively different discharge modes. The equilibrium plasma profiles suggest where the plasma production and heating takes place and with it, they give insight into the discharge mechanism itself. They are measured and discussed in Sec. 6.1. Since the spatial distribution of the plasma parameters depends on the local power deposition, the magnetic modestructure is measured and compared for the capacitive and the helicon wave sustained mode in Sec. 6.2. The transition between the discharge modes is not gradual but occurs in sudden jumps. The detailed mechanism of the transition physics to the helicon mode is currently subject of intense scientific research (e.g. on the APS Mini-Conference on Applications of Helicon Plasma Sources [2001] or [Chen, 1991; Shamrai and Taranov, 1995; Balkey et al., 2001]). In Sec. 6.3, experiments on the transition behaviour between the three discharge modes in the VINETA experiment are shown. These measurements stand in contrast to some existing models that are based on the plasma density as the critical parameter (this work is also published in [Franck et al., 2003]).

6.1 Discharge Characterisation

The equilibrium plasma parameter profiles reflect the fundamental discharge mechanisms of the three different discharge modes. Langmuir probe measurements yield detailed information on the spatial structure of plasma density, plasma potential, and electron temperature. They are recorded in the poloidal plane perpendicular to the axial magnetic field. The measurements are done $\approx 0.5\,\mathrm{m}$ downstream from the plasma source. Each poloidal profile consists of at least 400 measurements with a high spatial resolution up to $\Delta \approx 5\,\mathrm{mm}$ within the antenna region and lower resolution of ≈ 10–$20\,\mathrm{mm}$ outside the antenna region, which is filled by cross field diffusion only [Perry et al., 2002]. The actual heating mechanism takes place only inside the antenna region and the resulting plasma is

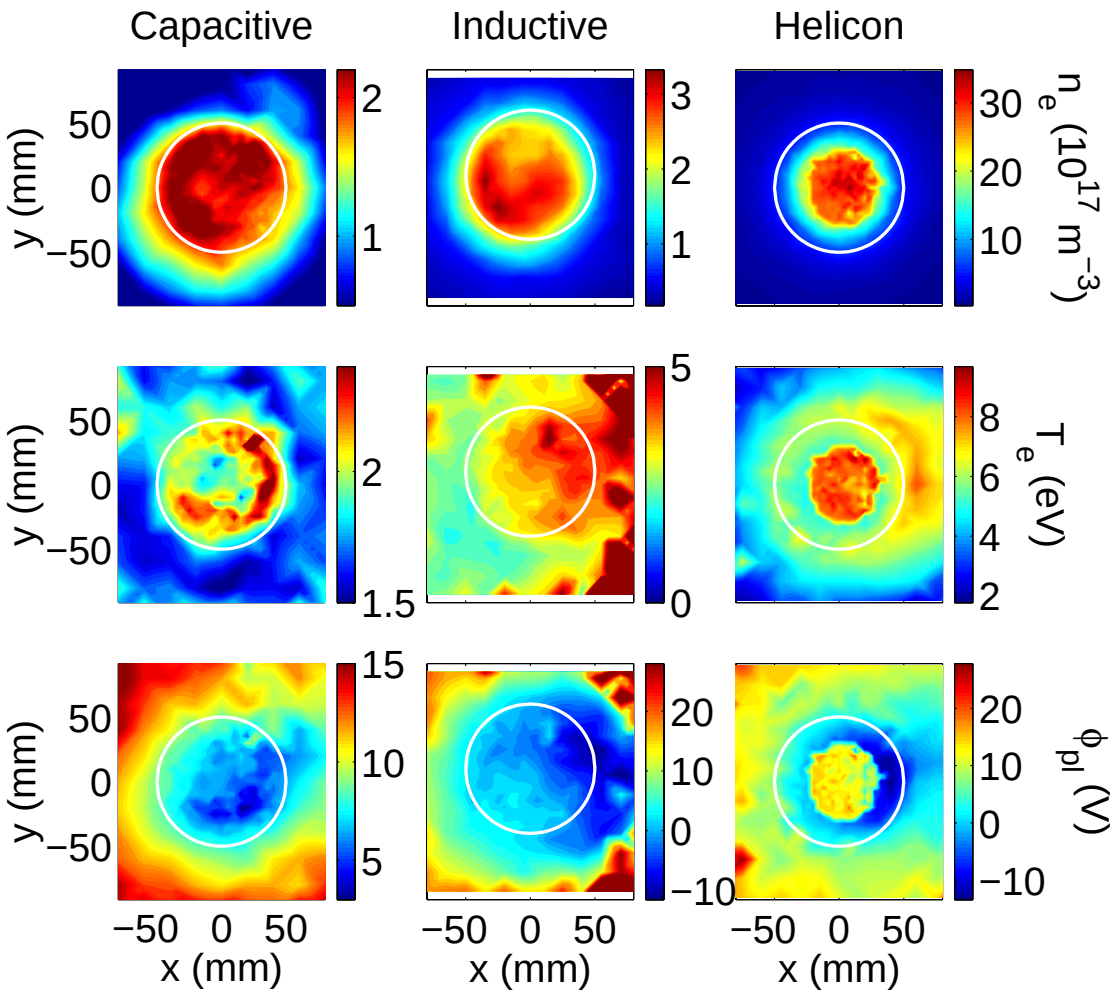

Figure 6.1: Equilibrium plasma parameter profiles taken in the poloidal xy-plane perpendicular to the ambient magnetic field. Shown are the plasma density (top row), electron temperature (middle row), and plasma potential (bottom row) for all three discharge modes. The white circles indicate the position of the antenna edge.

mapped downstream to the measuring position. Fig. 6.1 shows the colour coded plots of the poloidal profiles of plasma density n, electron temperature T_e, and plasma potential ϕ_{pl} in capacitive, inductive and helicon wave sustained mode, respectively. The poloidal position of the rf source antenna is indicated by a white circle. The first obvious difference between the discharge modes are the well separated plasma parameter regimes. The peak plasma density varies by more than an order magnitude and the centre plasma temperatures vary from 1–$8\,$eV. The second obvious finding is the varying degree of deviation from cylindrical symmetry in these measurements. These may well be due to parameter drifts while the measurements took place (typically $100\,$min). A systematic deviation can be seen particularly in the electron temperature and the plasma potential profiles in the region on the right-hand side outside the antenna (horizontal position $\mathrm{x} > 50\,$mm but vertical position $-50 < \mathrm{y} < 50$). At these positions, the probe measures characteristics in very thin plasma densities with the probe shaft extending maximally through the plasma

(cf. Fig. 4.20). The probe characteristics at these spatial positions are found to be distorted due to rf pickup effects at the probe leads. This distortion is largest in the strongly nonlinear electron start-off region and around the plasma potential (cf. Sec. 4.2.1). The almost linear saturation regions are less sensitive and consequently, the plasma density profiles have almost perfect cylindrical symmetry. However, major differences of the three discharge modes can be seen in the profile topologies and will be analysed subsequently.

The profiles of the *capacitive mode* are measured for a neutral gas pressure of $p = 0.08$ Pa, an rf power of $P_{\mathrm{rf}} = 400$ W, and an ambient magnetic field of $B_0 = 56$ mT. The plasma density has a hollow profile with a density hole in the centre and a fairly pronounced maximum extending from the sheath edge of the antenna. The maximum plasma density is $n = 2 \cdot 10^{17}\,\mathrm{m}^{-3}$, which is about the maximum density that can be reached in the capacitive mode in the VINETA experiment. Typical plasma densities in the capacitive mode are 10^{16}–$10^{17}\,\mathrm{m}^{-3}$. The electron temperature profile is hollow as well. Electron temperature peak values are found at the antenna sheath edge, matching fairly well the density profile. The temperature varies between 2.5 eV at the sheath edge of the antenna and 1.5 eV in the other regions. The plasma potential is always positive and has a flat profile with $\phi_{pl} = 4$–7 V in the bulk of the plasma. The plasma potential is determined by the potential drop of the sheath at the plasma boundary (grounded vessel walls) and is usually $\sim 2T_e$ above the wall potential [Riemann, 1991]. Close to the antenna position, the plasma potential rises rapidly up to 9 V. It is important to note that the sheath thickness in such a 'magnetically enhanced capacitive rf discharge' [Lieberman and Lichtenberg, 1994] is for our set of parameters predicted to be in the sub-millimetre range [Park and Kang, 1997], which is barely resolvable by our measurements. It is thus reasonable to interpret the rise of the plasma potential at roughly 5–10 mm distance from the antenna as the magnetic pre-sheath [Kim et al., 1995]. Its width is given by the simple expression $\delta_m = c_s/\omega_{ci}$ and calculates for typical capacitive mode conditions in the VINETA device (cf. Tab. 4.1) to $\delta_m \approx 2$–10 mm. To summarise, the profiles confirm the characteristic feature of a (magnetically enhanced) capacitive coupled plasma (Sec. 3.1). The plasma production by ohmic and stochastic heating is restricted to the antenna sheath edge, where the power density is highest. The centre (bulk) plasma column is mainly filled by cross field diffusion [Perry et al., 2002]. Downstream the source, the region outside the antenna cross section is also filled by cross field diffusion.

The plasma equilibrium profiles of the *inductive mode* are measured for $p = 0.6$ Pa, $P_{\mathrm{rf}} = 600$ W, and $B_0 = 56$ mT. The plasma density has an almost flat-top profile with strong gradients at the inner antenna region, which means a full-width-at-half-maximum (fwhm) diameter of $d_{\mathrm{fwhm}} \approx R_{ant} = 100$ mm. The peak plasma density is found to be $n = 4 \cdot 10^{17}\,\mathrm{m}^{-3}$. This density is typical for the inductive discharge mode operation in the VINETA experiment. The electron temperature follows the flat-top profile of the density and has a peak value of ≈ 4 eV. The plasma potential is fairly constant as well over the entire antenna cross section and shows, particularly in contrast to the capacitive discharge mode, no sheath structure close to the antenna. The observed poloidal profiles

are consistent with the commonly accepted models for inductive discharges (Sec. 3.2), where the induced current in the skin layer heats the plasma. The collisionless skin depth in the present operation are on the order of the antenna radius, which means that the skin layer expands from the antenna to the centre, thereby leading to flat-top profiles of the plasma parameters.

For the measurements in the *helicon wave sustained mode*, the device is operated at $p = 0.5\,\mathrm{Pa}$, $P_{\mathrm{rf}} = 3.5\,\mathrm{kW}$, and $B_0 = 75\,\mathrm{mT}$. The plasma production now seems to be completely detached from the antenna edge region. Plasma density, electron temperature and plasma potential are strongly peaked in the centre of the discharge. The fwhm-diameter of the plasma column is $d_{\mathrm{fwhm}} \approx 60\,\mathrm{mm}$, which means a clear reduction of the plasma diameter compared to the capacitive and the inductive mode operation. The peak density is $n = 3 \cdot 10^{18}\,\mathrm{m}^{-3}$ and with it an order of magnitude larger compared to the previous discharge modes. This value is again typical for helicon mode discharges in the VINETA. The peak electron temperature value is $T_e = 8\,\mathrm{eV}$ and the plasma potential rises from $0\,\mathrm{V}$ at the antenna edge to $15\,\mathrm{V}$ in the centre.

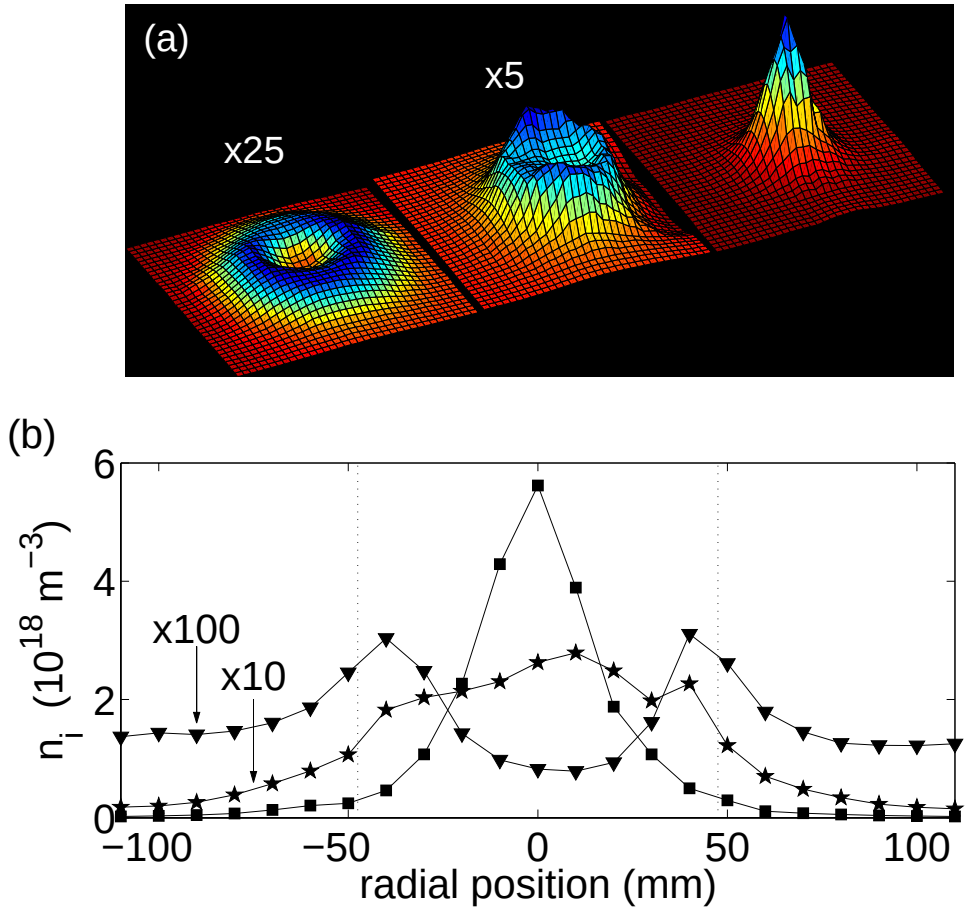

Figure 6.2: Plasma density measurements in the three discharge modes (capacitive, inductive, and helicon from left to right) shown for a poloidal plane perpendicular to the magnetic field (a) and for radial cuts (b). The dotted lines mark the source glass tube diameter and the density in the capacitive and inductive modes is enlarged. Published in [Franck et al., 2003].

In summary, the observed poloidal equilibrium plasma profiles in the capacitive and in the inductive mode of operation can be explained by standard discharge models as reviewed in Secs. 3.1 and 3.2. The plasma production in the capacitive mode mainly occurs in the antenna sheath region, where the electric fields are largest. In the inductive mode, the rf antenna currents become large enough to induce electric fields, resp. and induced current, that heat the plasma. The heating takes places within the skin depth layer. The physical mechanism of the helicon mode discharge is still a scientific case and only little insight into the formation mechanism of plasma profiles is currently available. The plasma profile measurements suggest, however, that the power deposition is located in the plasma centre.

The above reasoning is supported by an additional set of measurements. Fig. 6.2 (a) shows density measurements in the three discharge modes (from left to right: capacitive, inductive, and helicon) taken in a poloidal plane perpendicular to the magnetic field at a distance of 1 m from the antenna centre. Radial cuts for the three different discharge modes (▼ capacitive, ★ inductive, and ■ helicon wave sustained) are shown in Fig. 6.2 (b). The dotted lines indicate the source glass tube diameter. The profiles are taken for $B_0 = 85$ mT at an argon gas pressure of 0.3 Pa. The matching circuit capacitors are adjusted to minimise the reflected power in each mode. The density profiles are determined from ion saturation measurements, which are much faster than full probe characteristics. This enables profile measurements with considerably higher spatial resolution. Up to 1000-2000 points are taken in the poloidal plane and the parameter drift is also much less in this shorter time span. Absolute values are found from comparison with full characteristics at some spatial positions. The measurements shown in Fig. 6.2 fully support the above mentioned explanations. In particular, they confirm the antenna sheath heating in the capacitive mode, the bulk heating from induced currents in the inductive mode and the centre peaked heating in the helicon wave sustained mode.

6.2 Modestructure

The measurements of the equilibrium plasma profiles in the previous section showed that the plasma production in the helicon mode is completely decoupled from the antenna edge region and restricted to the centre volume. In contrast to that is the plasma production in the capacitive and inductive mode, where the plasma production takes place in the antenna sheath and by induced currents in the skin layer of the plasma, respectively. It was suggested from previous radial wave profile measurements by Light and Chen [1995] and low resolution measurements in the poloidal plane by Ellingboe and Boswell [1996] that the detachment from the antenna edge is associated to the power deposition from a propagating wave, the helicon wave. Therefore, we focus on measuring the waves' magnetic fields in the discharge. In particular, the difference between the capacitive and the helicon mode with respect to their magnetic eigenmode structure is highlighted. The experimental setup is shown in Fig. 4.20 and explained in Sec. 4.4.

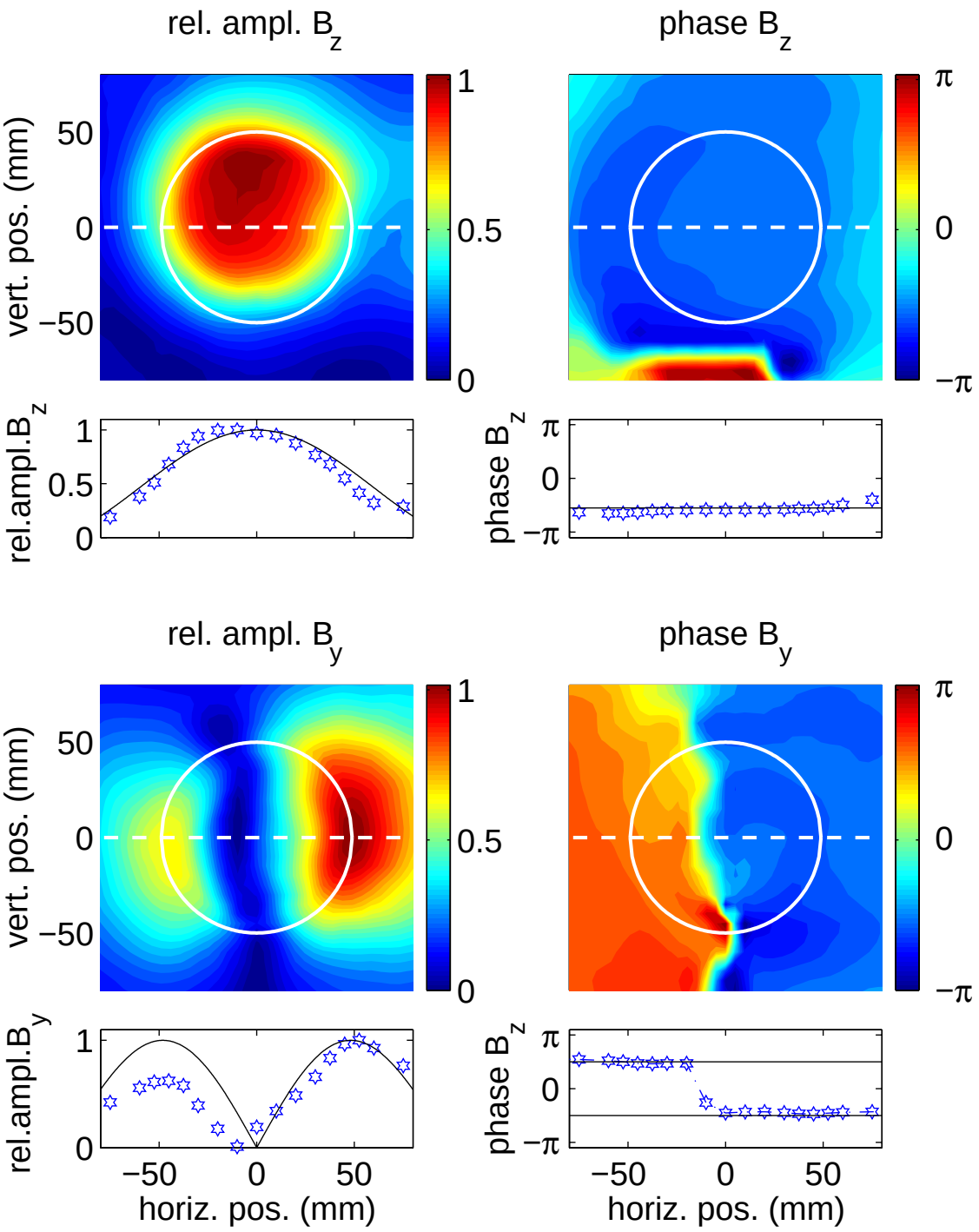

Figure 6.3: Poloidal profiles of the wave magnetic structure in a capacitive mode discharge. Shown are the poloidal measurements of the amplitude (left) and the phase (right) of the parallel ($\dot{B}_z$, top) and perpendicular ($\dot{B}_y$, bottom) components. The white circles indicate the antenna edge positions and a horizontal cut is made through the centre (dashed lines) to compare the measurements (markers) to the theoretical profiles (solid lines) of an $m = 0$ mode wave in a bounded plasma (1d plots).

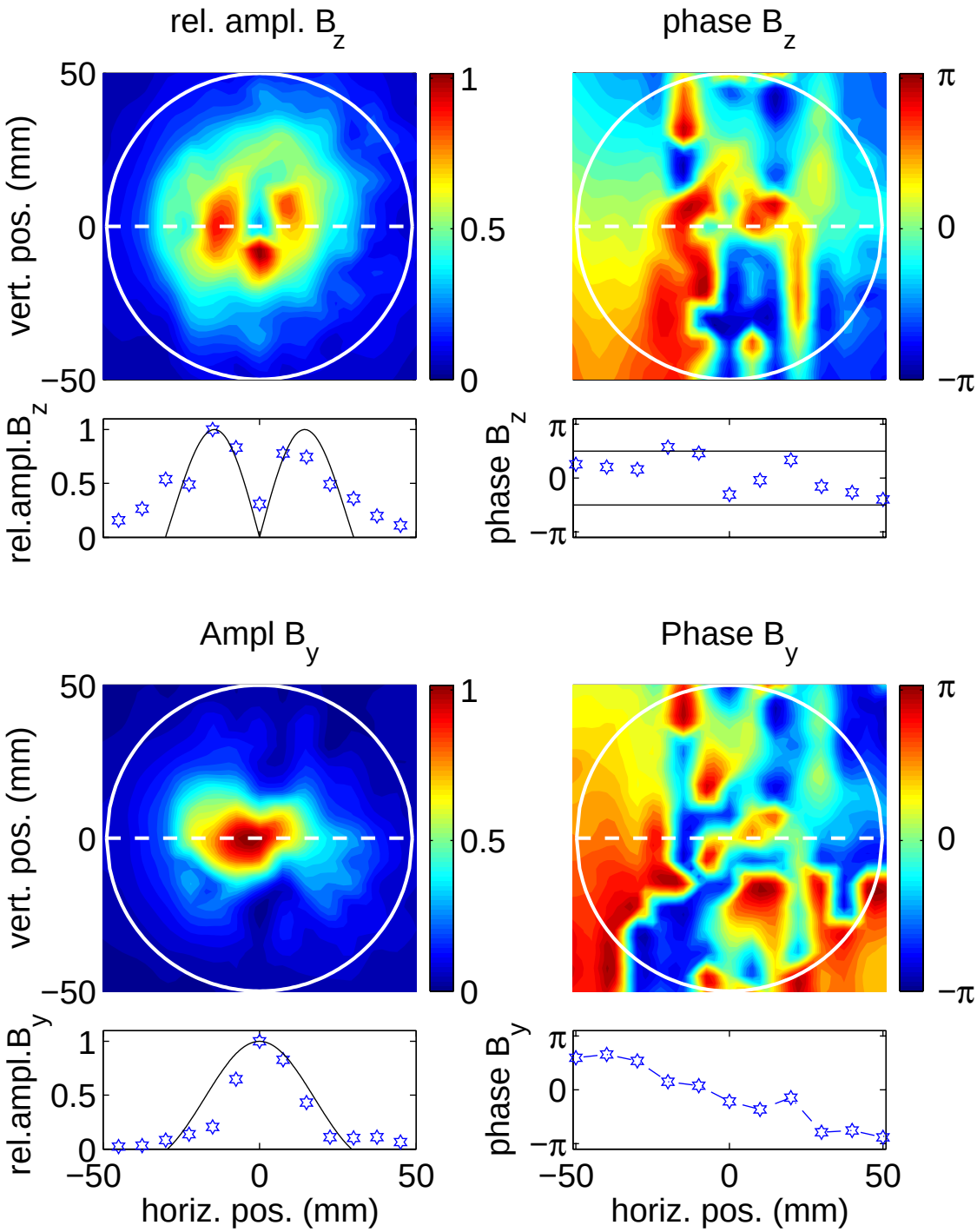

Figure 6.4: Poloidal profiles of the wave magnetic structure in a helicon wave sustained discharge mode. Shown are the poloidal measurements of the amplitude (left) and the phase (right) of the parallel ($\dot{B}_z$, top) and perpendicular ($\dot{B}_y$, bottom) components. The white circles indicate the antenna edge positions and a horizontal cut is made through the centre (dashed lines) to compare the measurements (markers) to the theoretical profiles (solid lines) of an $m = 1$ mode wave in a bounded plasma (1d plots).

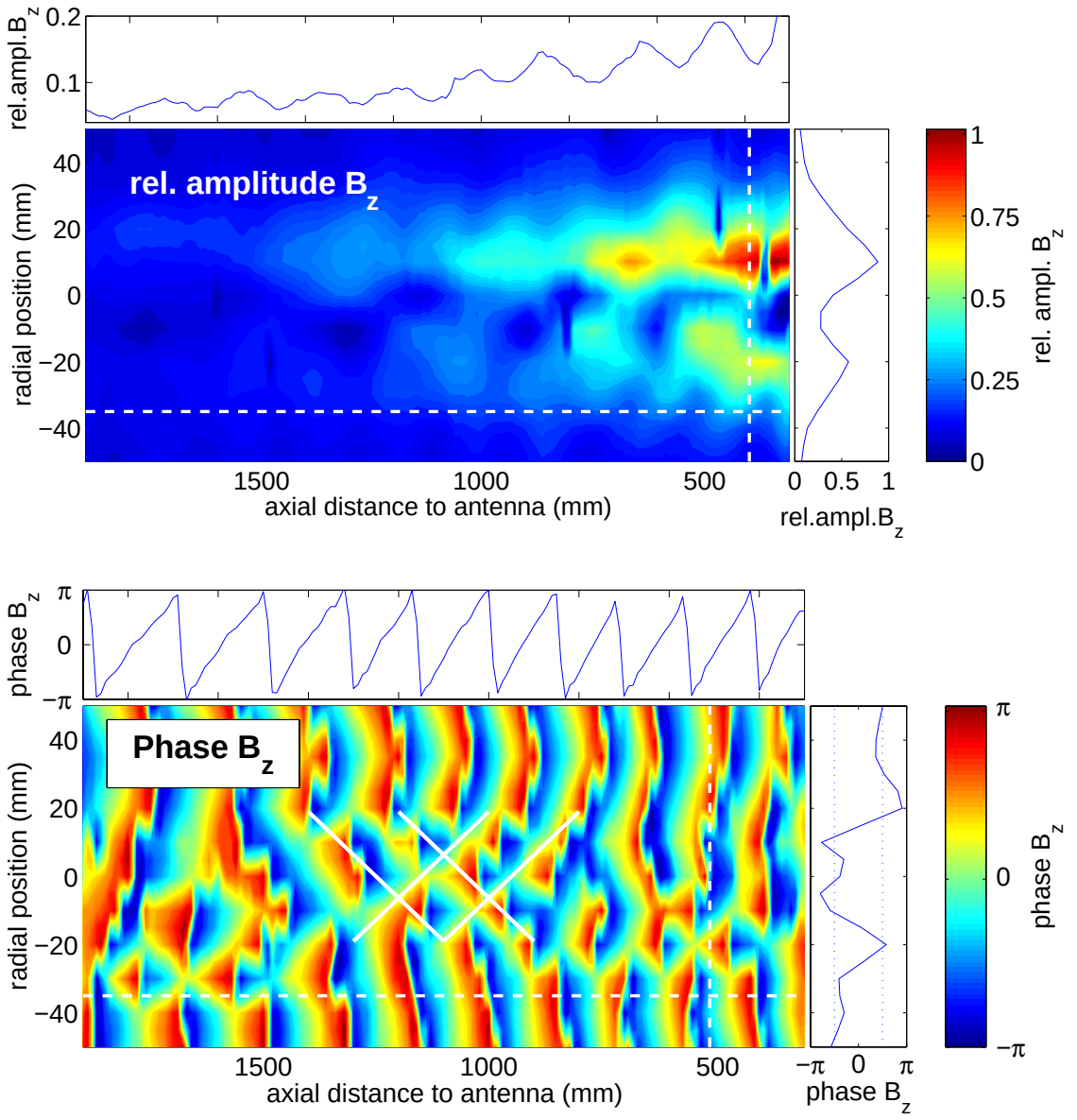

Figure 6.5: Measurements of the magnetic fluctuations in the axial direction parallel to the ambient magnetic field $\dot{B}_z$ in a helicon mode discharge. Shown are the amplitude (top) and phase (bottom) in the horizontal plane parallel to the magnetic field. The 1D plots are made along the cuts indicated by the white dashed lines. The solid white lines in the phase plot underline the clearly visible phase fronts.

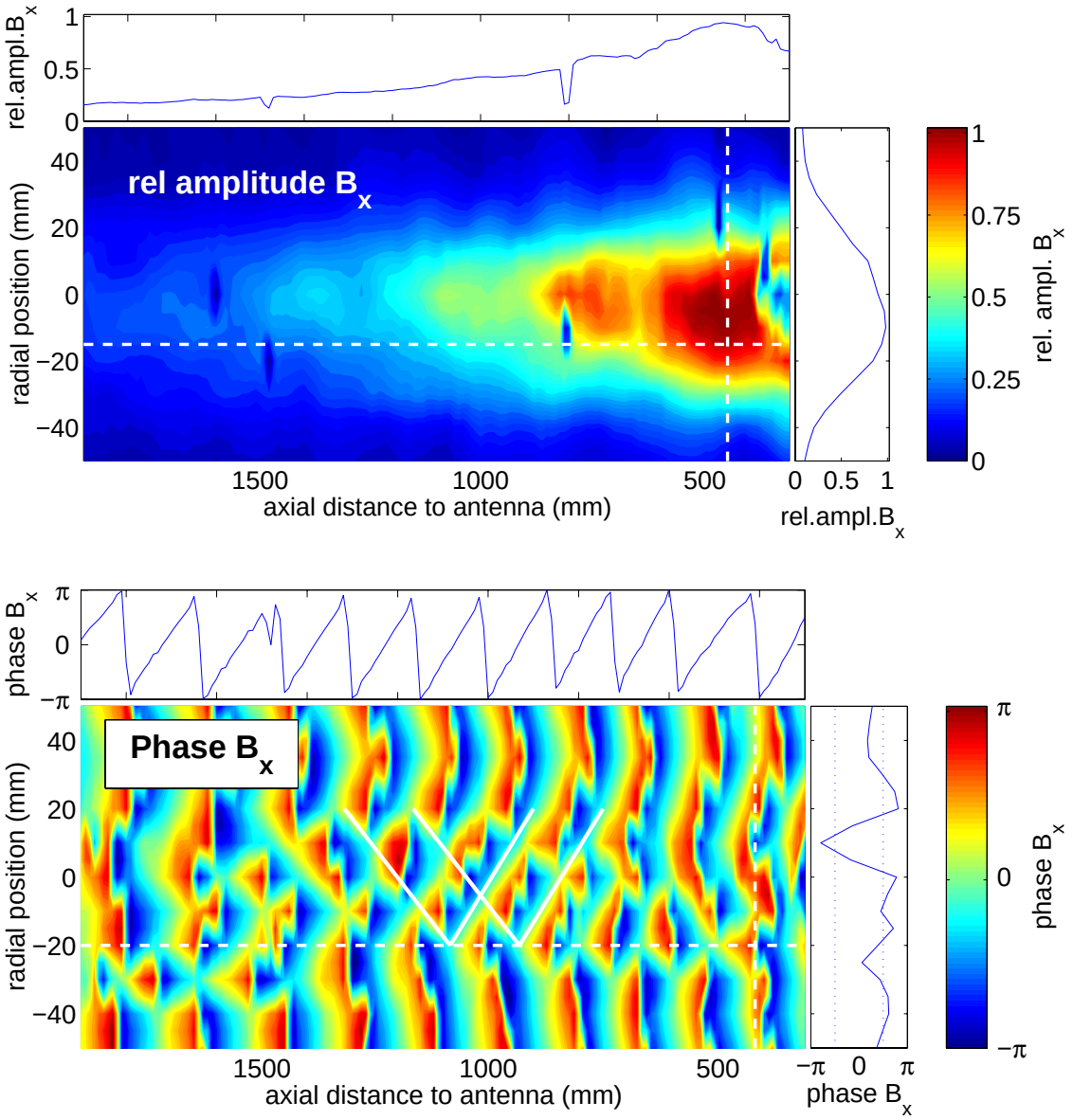

Figure 6.6: Measurements of the magnetic fluctuations in the direction perpendicular to the ambient magnetic field $\dot{B}_x$ in a helicon mode discharge. Shown are the amplitude (top) and phase (bottom) in the horizontal plane parallel to the magnetic field. The 1D plots are made along the cuts indicated by the white dashed lines. The solid white lines in the phase plot underline the clearly visible phase fronts.

Fig. 6.3 shows measurements of the poloidal structure of the wave magnetic fields in the capacitive discharge mode with $p = 0.7\,\text{Pa}$, $P = 500\,\text{W}$, and $B_0 = 56\,\text{mT}$. The plots show the amplitude and the phase of the wave magnetic field components parallel $\dot{B}_z$ and perpendicular $\dot{B}_y$ to the ambient magnetic field in colour-coded representation. Again, the poloidal location of the antenna edge is indicated by a white circle. A radial cut through the centre (dashed white line) is made for better visual inspection (lower half diagrams). Moreover, the measurements (markers) are compared with the theoretical wave field profiles (solid lines), cf. Sec. 2.4.3. The amplitude profile of the axial component $\dot{B}_z$ shows a maximum in the centre and drops off towards the edges whereas the phase is constant over almost the entire poloidal cross section. This is in very well agreement with the theoretical prediction (cf. Fig. 2.15, right). The radial section of the wave amplitude is plotted together with the theoretically predicted profile of a $m = 0$ mode wave Eq. (2.79) with radial wave number $k_\perp = 3.83/0.1\,\text{m}^{-1}$. Phase shift measurements in the parallel direction yield a parallel wave number $k_\parallel \approx 2\pi/4\,\text{m}^{-1}$. The measurements of the amplitude and the phase of the perpendicular component $\dot{B}_y$ fully support this picture. The wave field amplitude shows two maxima and a minimum in the centre. The phase changes sign in the centre, showing that the two maxima are in fact maximum and minimum in wave field amplitude. The radial cut shows a good agreement with the theoretically expected profile of an $m = 0$ mode wave Eq. (2.78) with radial wave number $k_\perp = 3.83/0.1\,\text{m}^{-1}$.

In contrast to the capacitive discharge, a different mode structure is obtained in the helicon discharge, although the helicon wave excitation setup remains the same. Fig. 6.4 shows plots of the poloidal structure of the wave magnetic fields in the helicon wave sustained discharge mode with $p = 0.7\,\text{Pa}$, $P = 2.4\,\text{kW}$, $B_0 = 56\,\text{mT}$. The measurements are done in pulsed mode operation to prevent the sensitive probes from being damaged under the stressing plasma conditions. Again, the amplitude and the phase of the parallel $\dot{B}_z$ and perpendicular $\dot{B}_y$ components of the wave magnetic fluctuations are shown. Two main differences to the capacitive mode can be seen right away. First of all, the wave amplitude is constrained to a much smaller poloidal region (within radius $\lesssim 35\,\text{mm}$) inside of the antenna cross section. The measurements in this centre region are made with maximum spatial resolution of $5\,\text{mm}$, which is about the probe size plus ceramic shielding. The radial cut shows a clear minimum of the wave amplitude for the parallel magnetic fluctuation $\dot{B}_z$ in the centre and two maxima at $r \approx 25\,\text{mm}$, accordingly. The corresponding phase changes sign in the centre. Again, the poloidal plot is in well agreement with the theoretical prediction (cf. Fig. 2.15, left). The amplitude of the perpendicular fluctuations $\dot{B}_y$ in turn shows a maximum in the centre and decreases with increasing radius r. The phase shows a gradual change from left to right. Plotted with solid lines in the radial cuts are the theoretical amplitude profiles of an $m = 1$ mode Eqs. (2.78) and (2.79) with perpendicular wave number $k_\perp = 3.83/0.05\,\text{m}^{-1}$. This wave number corresponds exactly to the antenna radius. The measurements agree reasonably well with theory. The only noticeable deviation is that the phase for $\dot{B}_y$ should be constant. Another difference with regard to the measurements in the capacitive mode is the quite strong scatter in the phase

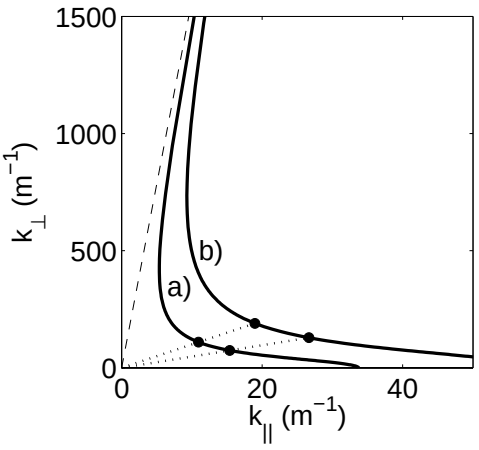

Figure 6.7: Polar plot of the wave vector (index surfaces) at $f = 10\,\mathrm{MHz}$, $B_0 = 56\,\mathrm{mT}$ and two different plasma densities: a) $n = 5 \cdot 10^{18}\,\mathrm{m}^{-3}$ and b) $n = 1.5 \cdot 10^{19}\,\mathrm{m}^{-3}$. The dotted lines indicate the angles $\theta = 84°$ and $\theta = 78°$, and the dashed line indicates the resonance cone angle $\theta_{\mathrm{res}} = 89.5°$.

measurements. These irregularities can be attributed to parameter drifts in the discharge during the measurements which last for up to 2 hours.

For the helicon wave sustained discharge, Figs. 6.5 and 6.6 show horizontal profiles of the parallel $\dot{B}_z$ and perpendicular $\dot{B}_x$ magnetic wave fluctuation amplitude and phase in a plane parallel to the ambient magnetic field. Again, the measurements are averaged at each position to improve the signal-to-noise-ratio. The radial resolution is $\Delta r = 7.5\,\mathrm{mm}$ and the axial resolution is $\Delta z = 20\,\mathrm{mm}$. This sums up to a total of more than 1300 averaged data points to cover the plane. Axial and radial cuts along the white dashed lines are also shown. The experimental conditions are $B_0 = 56\,\mathrm{mT}$, $f = 10\,\mathrm{MHz}$, $p = 0.5\,\mathrm{Pa}$, and $P_{\mathrm{rf}} = 2\,\mathrm{kW}$. In the top graph of Fig. 6.5, the radial amplitude profile of the parallel $\dot{B}_z$ fluctuations shows again the structure of an $m = 1$ mode wave with a minimum in the centre of the discharge and two maxima at $r \approx \pm 25\,\mathrm{mm}$. The axial amplitude profile, obtained here by the cut slightly off-centre ($\approx 35\,\mathrm{mm}$), shows an amplitude modulated structure with $\lambda_{\parallel} \approx 150\,\mathrm{mm}$ wave length. The amplitude is damped away almost completely over the measuring distance of $2\,\mathrm{m}$. In the bottom graph of Fig. 6.5, the diagram of the axial evolution of the relative phase shows a 2π phase shift every $\approx 150\,\mathrm{mm}$. This parallel wavelength is exactly half the antenna length and is considerably smaller than in the capacitive mode. The radial cut shows that the phase changes sign in the centre. Besides this main structure in the phase, a fine structure of crossed phase fronts is observed as well and will be treated in more detail below. The perpendicular $\dot{B}_x$ fluctuations, shown in Fig. 6.6, correspondingly show all features expected for an $m = 1$ mode wave. The radial profile of the wave amplitude has a maximum in the centre and the amplitude decreases away from the centre. The axial distribution does not display an axial modulation like the $\dot{B}_z$ fluctuations but is gradually damped over the measured $2\,\mathrm{m}$ as well. The general structure of the phase shows almost almost constant values in radial direction, again with some fine structure features in the centre. The parallel wavelength determined from the axial 2π phase shifts is again $\lambda_{\parallel} \approx 150\,\mathrm{mm}$, which is consistent with the $\dot{B}_z$ measurements.

Inspecting the phase diagrams Figs. 6.5 and 6.6 more carefully, a rather complex substructure of the phase planes becomes evident which suggest interference effects to be

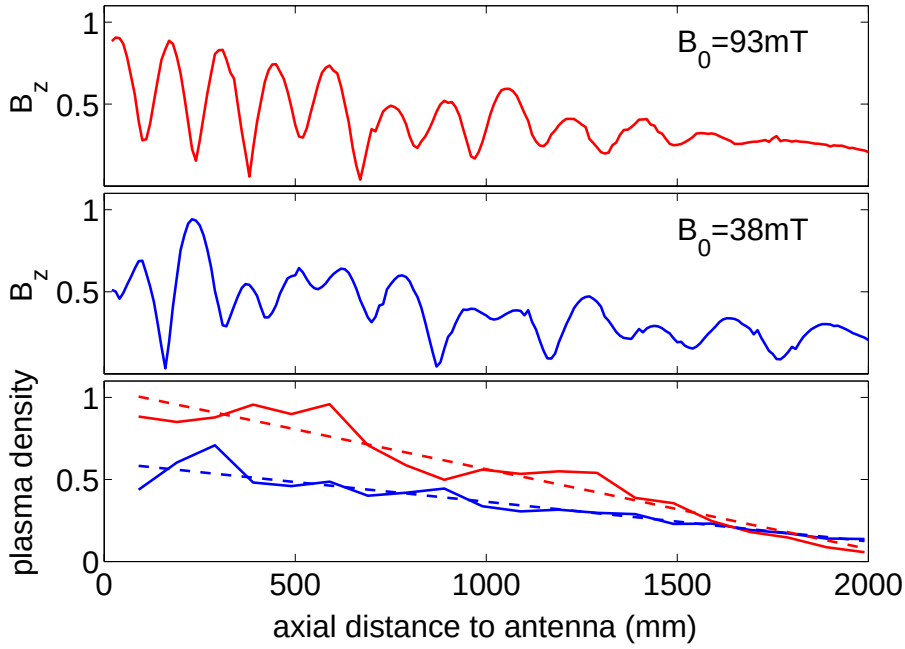

Figure 6.8: Axial measurement of the amplitude of $\dot{B}_z$ for two different ambient magnetic field strengths: $B_0 = 93\,\mathrm{mT}$ (top, red) and $B_0 = 38\,\mathrm{mT}$ (middle, blue). The axial plasma density for the two configurations is shown in the bottom graph with the corresponding colours.

of importance. The propagation of bounded plasma waves can also be discussed from the point of view of geometrical optics, in particular if the eiconal assumption is justified [Landau and Lifschitz, 1977]. The waves propagate oblique to the magnetic field and are reflected at the boundary, similar to the physics of an fibre optical light guide [Jackson, 1999]. The present measurements partially support this picture. In the two phase plots of Figs. 6.5 and 6.6, phase fronts of reflected waves are clearly visible and are emphasised by solid white lines. The angle of the normals of these fronts with respect to the ambient magnetic field can be calculated to be $\cot^{-1}(40/385) \approx 84°$ in Fig. 6.5 and $\cot^{-1}(40/185) \approx 78°$ in Fig. 6.6 (note the different scales on the r- and z-axis). Fig. 6.7 shows the polar plots of the wave vector for the present experimental situation ($f = 10\,\mathrm{MHz}$ and $B_0 = 56\,\mathrm{mT}$) at two different plasma densities: a) $n = 5 \cdot 10^{18}\,\mathrm{m}^{-3}$ and b) $n = 1.5 \cdot 10^{19}\,\mathrm{m}^{-3}$. The two different plasma densities are the typical density range within the measuring plane. The dotted lines indicate the two experimentally determined phase front angles $\theta = 84°$ and $\theta = 78°$. Since the phase front angle can only be determined from the measurements to be within a certain range, only a range of wave vectors can consequently be evaluated: $k_\parallel = 11$–27 and $k_\perp = 75$–200. These wave vectors are on the right order of magnitude if compared to theoretically derived values or the previously measured ones. The accuracy and the limits of this will be discussed in detail in Chap. 8.

So far, the axial and parallel wave numbers have been determined in the helicon mode for one set of parameters. The measurements have shown that $k_\parallel = 2\pi/0.2\,\mathrm{m}^{-1}$ and $k_\perp = 3.83/0.05\,\mathrm{m}^{-1}$ are determined by the antenna geometry. It is now revealing to analyse their dependence on the plasma and discharge parameters, especially the ambient

magnetic field B_0. Fig. 6.8 shows the axial profiles of the parallel magnetic fluctuations $\dot{B}_z$ measured slightly off centre ($\approx 30\,\mathrm{mm}$), where the fluctuation amplitude has a maximum. The measurements are made for two different magnetic field strengths: the red curve (top) shows the measurements at $B_0 = 93\,\mathrm{mT}$ and the blue curve (middle) at $B_0 = 38\,\mathrm{mT}$. The wavelength determined from the phase shifts of both measurements yield the same value of $\lambda_\parallel = 150\,\mathrm{mm}$ within the small errorbars ($\leq 10\,\%$). The parallel wave number is thus independent from the ambient magnetic field. Measurements of the perpendicular wave number (not shown here) yield the same result, the perpendicular wave number is independent from the ambient magnetic field. With respect to the simplified helicon dispersion relation (2.53) this implies that for fixed wave numbers and fixed driving frequency, the plasma density is proportional to the magnetic field. The normalised axial density distributions (solid lines) are shown together with linear best fits (dashed lines) for the two measurements in the bottom graph of Fig. 6.8. And, indeed, the measurements agree qualitatively well with the scaling given by the simple helicon dispersion (2.53), i.e. the density increases with increasing magnetic field. The quantitative agreement is not as good: the ratio of the magnetic field strengths ($93/38 \approx 2.42$) and the ratio of the densities close to the antenna ($1.05/0.6 \approx 1.73$) only agree within $\approx 30\,\%$.

6.3 Transitions between Discharge Modes

The transition between the three different discharge modes is not continuous but occurs via sudden jumps at certain rf power levels [Perry et al., 1991; Chen, 1992; Shoji et al., 1993] or magnetic field strengths [Boswell, 1984b]. So far, measurements with varying rf power or magnetic fields have only been made step-by-step under fully established conditions. This procedure allows the measurement of discontinuous plasma parameter evolutions but cannot resolve dynamical or hysteresis phenomena. High resolution density measurements are made in the VINETA device during an rf power ramp [Franck et al., 2003]. The source was operated continuous wave (cw) and the rf power was varied in $2.5\,\mathrm{s}$ from 200–2000 W. During this ramp all other discharge parameters were kept constant: argon gas pressure $0.6\,\mathrm{Pa}$, magnetic field $38\,\mathrm{mT}$, and constant matching capacitor settings (for minimum reflected power in the inductive mode). The relative plasma density is recorded slightly off centre ($\approx 35\,\mathrm{mm}$) inside the helicon source tube by the ion saturation current of a Langmuir probe. The rf power and the plasma density are recorded simultaneously with $100\,\mathrm{kSamples/s}$. Fig. 6.9 shows the results of density measurements during such a power ramp. The measurements show a qualitative difference during the power-up and power-down ramp. During the power up ramp, the discharge remains in the capacitive mode with relatively low densities $n \approx 4 \cdot 10^{16}\,\mathrm{m}^{-3}$ up to rf powers of $1.2\,\mathrm{kW}$. For further increased rf power up to $1.8\,\mathrm{kW}$ the capacitive mode is maintained. Between $1.5\,\mathrm{kW}$ and $1.8\,\mathrm{kW}$ the density at the probe position even decreases. At $1.8\,\mathrm{kW}$ rf power level, a sudden density jump by more than a factor of twenty to $n \approx 9 \cdot 10^{17}$ occurs within a power interval of $10\,\mathrm{W}$, which can be identified as a transition between

the capacitive mode (low density) and the helicon mode (high density). The latter can be easily identified via the 'blue core', a luminous bright zone in the discharge centre [Blackwell and Chen, 1997] and via the poloidal discharge profiles and modestructure, shown in the previous Secs. 6.1 and 6.2. Further increase of the rf power leads to a small increase of the plasma density only. The inset of Fig. 6.9 shows the temporal evolution of the density in the time interval around the transition from the capacitive mode to the helicon mode. The density measurement shows a short (≤ 0.8 ms) step at an intermediate density level which might suggest a transient appearance of the inductive mode. A fairly different scenario is observed if the rf power is ramped down, starting at a power level with an established helicon mode. At exactly the same power level at which previously the jump from capacitive to helicon mode occurred, a sudden drop of plasma density is observed, but remains at an intermediate level of $n \approx 7 \cdot 10^{17}\,\mathrm{m}^{-3}$. This intermediate state is identified as the inductive discharge mode. The plasma density then decreases gradually with decreasing rf power. At 1.2 kW, another sudden density drop is observed, the transition from the inductive mode to the capacitive mode. This difference in transition behaviour for increasing and decreasing rf power ramp, and in particular, the direct transition from the capacitive mode to the helicon mode is of great importance as it contradicts transition models based on the plasma density as the critical parameter for the transition to the helicon mode [Kaeppelin et al., 2001]. The measurements rather suggest that the rf power density is the important parameter as the transition from the capacitive to the helicon mode as well as the transition from the helicon mode to the inductive mode occur at exactly the same forward rf power level and will be discussed in Chap. 8.

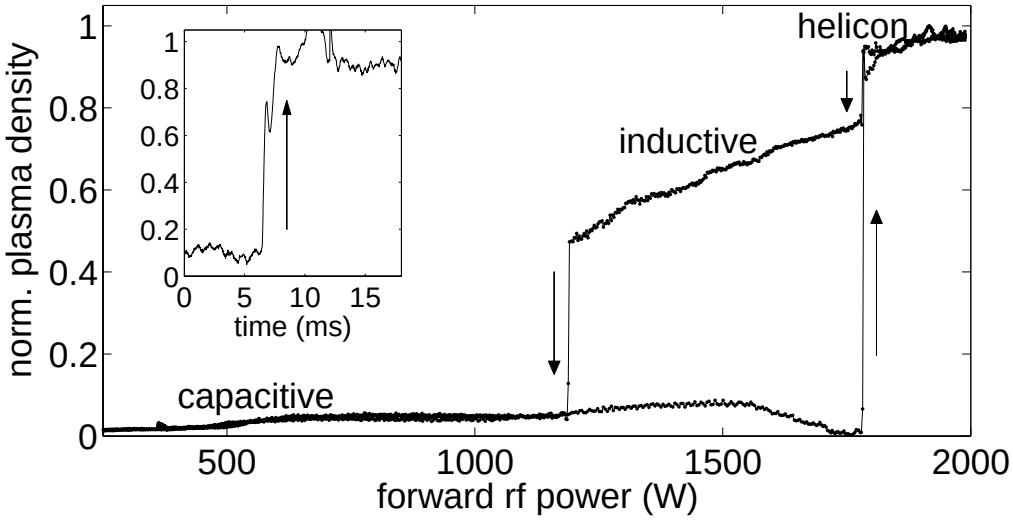

Figure 6.9: Density vs rf power during a 2.5 s power ramp. The density is normalised to the maximum density. For increasing rf power, the discharge transits from the capacitive mode into the helicon wave sustained mode directly (arrow up). For decreasing rf power, the discharge goes through an intermediate density mode, the inductive mode (arrows down). The inset shows the non-averaged density evolution during the power-up ramp at the transition from the capacitive mode to the helicon mode. Published in [Franck et al., 2003].

7

Whistler Wave Dispersion from Unbounded to Bounded Plasma

The two extreme approximations for R-waves, unbounded whistler waves and strongly bounded helicon waves, were studied separately in the previous two chapters to some detail. Within this chapter, the transition between both cases, the transition from an unbounded to a bounded plasma whistler wave dispersion is investigated (partly published in [Franck et al., 2002c]). As shown in Sec. 2.3.3, the parallel wavelength of an R-wave is a function of the excitation frequency, the ambient magnetic field strength, and the plasma density. All three parameters are controllable within the VINETA experiment and the plasma density can even be varied by four orders of magnitude. Particularly easy to vary is the excitation frequency. To study the transition from unbounded to bounded plasma wave propagation, the wavelength to vessel radius ratio $\lambda_\parallel/R_c$ is gradually increased from values < 1 to values $\gg 1$ by setting the appropriate plasma parameters and exciting waves at different frequencies. Fig. 7.1 shows wave dispersion measurements (markers) in the capacitive discharge mode at low plasma density $n \approx 2 \cdot 10^{16}\,\mathrm{m}^{-3}$ (average value) at two different magnetic fields: $B_0 = 20\,\mathrm{mT}$ (top graph) and $B_0 = 38\,\mathrm{mT}$ (bottom graph). The measurements are mostly very accurate with errorbars sometimes smaller than the marker size; only the measurements at $300\,\mathrm{MHz}$ are quite erroneous. Included in the two plots are the whistler wave dispersion curves (2.42) for unbounded plasmas (solid lines) and the simple analytic approximation for bounded plasma geometry Eq. (2.64) with $R_c = 0.2\,\mathrm{m}$ (dashed lines). Within these plots, two regimes are clearly distinguished: First, at higher frequencies ($f > 300\,\mathrm{MHz}$), corresponding to small wavelengths ($\lambda_\parallel/R_c \lesssim 1$), the wave dispersion behaviour is well described by unbounded plasma whistler wave dispersion. Second, at lower frequencies, corresponding to wavelengths that are in the range of the experimental dimensions $\lambda_\parallel/R_c \gtrsim 1$, the parallel wavelengths are always larger than expected for unbounded plasma whistler waves. This is an indication that in this region the waves no longer remain unaffected by the plasma boundary and a more appropriate theory has to be used. The theoretical dispersion relation (2.63) for bounded plasmas quantitatively reproduces the larger measured wavelengths for lower frequencies. Nevertheless, it does not resolve the exact shape of the measured dispersion over the entire frequency range. This is reasonable as Eq. (2.64) is derived under two approximations which are

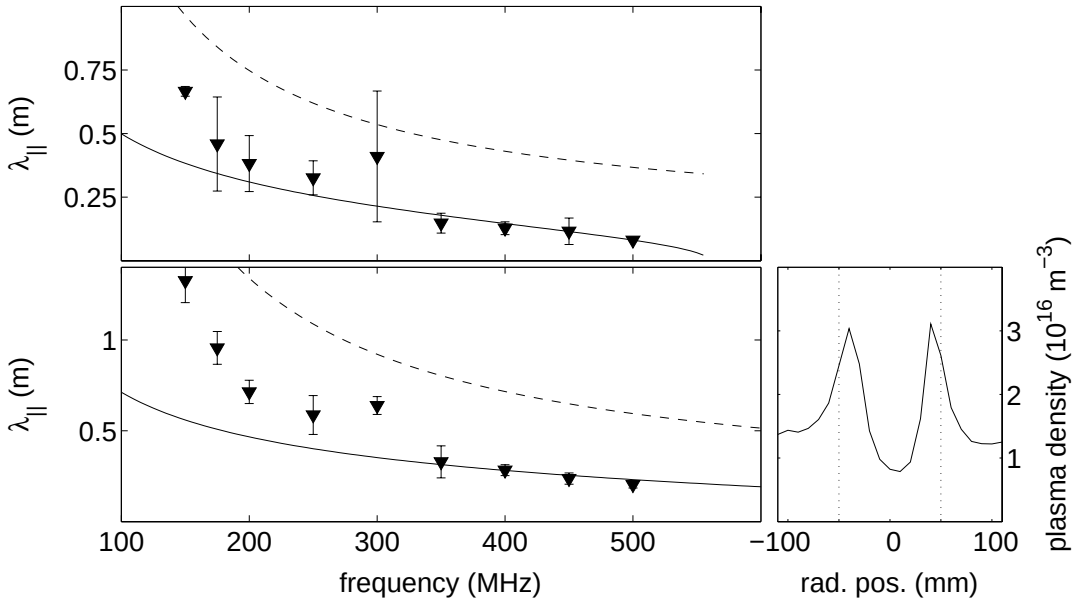

Figure 7.1: Whistler wave dispersion measurements in the low density capacitive discharge mode for $n \approx 2{\cdot}10^{16}\,\mathrm{m}^{-3}$ at two different magnetic fields, $B_0 = 20\,\mathrm{mT}$ (top) and $B_0 = 38\,\mathrm{mT}$ (bottom). Shown are the measurements (markers), the theoretical curve for the R-wave dispersion (2.40) in unbounded plasmas (solid lines), and curve from Eq. (2.64) for whistler waves bounded in a homogeneous plasma cylinder with radius $R_c = 0.2\,\mathrm{m}$ (dashed lines). On the right-hand side, the radial plasma density is shown.

not completely satisfied in the present experimental conditions. First, the low frequencies approximation ($\omega \ll \omega_{pe}$) prohibits a correct description for all used wavelengths. The excitation frequencies used in this set of measurements are only a factor 4–10 smaller than the plasma frequency $f_{pe} \approx 2\,\mathrm{GHz}$. Second, a completely filled waveguide with homogeneous plasma density is assumed in theory. The density profile of the plasma in the capacitive mode used for these measurements is shown on the right-hand side of Fig. 7.1. It clearly deviates from a homogeneous situation. The measured profile is indeed inhomogeneous with density maxima at the antenna edge ($R_{ant} = 50\,\mathrm{mm}$). Moreover, the plasma density decreases towards the boundary and a 'vacuum gap' with very low plasma density is established between the plasma and the conducting vessel wall. However, the used theoretical description already explains the increase in wavelength in the regime where the boundary influences the wave propagation.

In a next step, experiments with a more homogeneous density distribution are done. In the discharge, a parameter regime is chosen to minimise the hollow profile structure of the plasma. Unfortunately, the well suited inductive mode, which has an almost flat-top profile, cannot be established in the VINETA at densities below $10^{17}\,\mathrm{m}^{-3}$. At those densities, wavelengths are too small ($\lambda_\parallel / R_c < 1$) to see a significant effect of the plasma boundary (cf. Fig. 5.2). Dispersion measurements are done in the capacitive discharge mode with $B_0 = 56\,\mathrm{mT}$ and $p = 0.2\,\mathrm{Pa}$ for three different rf powers. The resulting radial plasma profiles are shown on the right-hand side of Fig. 7.2 with $n = 1.75 \cdot 10^{16}\,\mathrm{m}^{-3}$

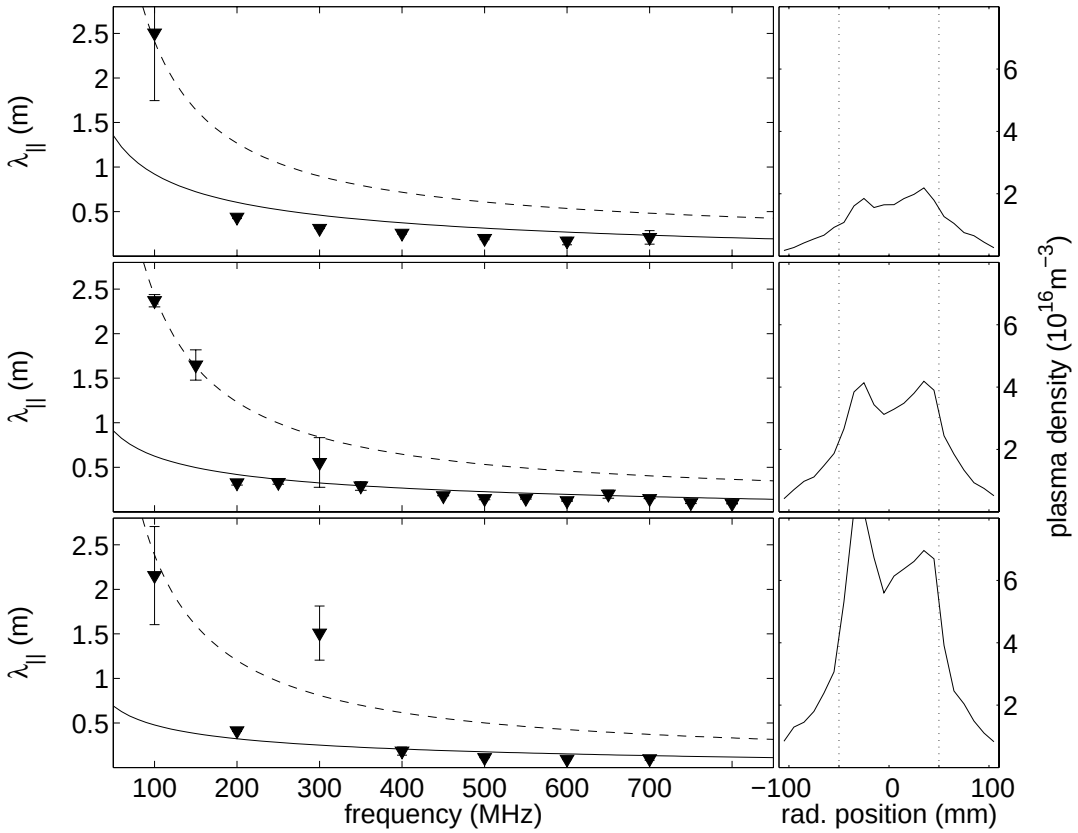

Figure 7.2: Whistler wave dispersion measurements in the capacitive mode with $B_0 = 56\,\mathrm{mT}$ and three different plasma densities. Shown are the measurements (markers), the theoretical curve for the R-wave dispersion (2.40) in unbounded plasmas (solid lines), and the curve from Eq. (2.64)(dashed lines) for whistler waves bounded in a homogeneous plasma cylinder with radius $R_c = 0.3\,\mathrm{m}$ (top), $R_c = 0.15\,\mathrm{m}$ (middle), and $R_c = 0.1\,\mathrm{m}$ (bottom). On the right-hand side, the three radial plasma density profiles are shown.

(top), $n = 4 \cdot 10^{16}\,\mathrm{m}^{-3}$ (middle), and $n = 7 \cdot 10^{16}\,\mathrm{m}^{-3}$ (bottom). On the left hand sides, the dispersion measurements in the three discharges are shown (markers). Again, the measurements are mostly very accurate with small errorbars and only the measurement at $300\,\mathrm{MHz}$ drops out. The frequency range of the measurements is covering the range of 100–$800\,\mathrm{MHz}$. Also plotted in Fig. 7.2 are the dispersion curves for unbounded whistler waves (solid lines) and for bounded waves using Eq. (2.64) with $R_c = 0.3\,\mathrm{m}$ (top), $R_c = 0.15\,\mathrm{m}$ (middle), and $R_c = 0.1\,\mathrm{m}$ (bottom). Once again, two regimes can be distinguished: For higher frequencies above $200\,\mathrm{MHz}$, the measurements are well described by the whistler wave dispersion curve for unbounded plasmas. For smaller frequencies, the unbounded dispersion curve is always below the measured values. The transition between both regions is very steep, covering the small frequency range of ≈ 100–$200\,\mathrm{MHz}$. In this set of experiments, again, the bounded wave expression (2.64) can only describe the increase in wavelength but not resolve the exact shape. However, from these measurements in the more homogeneous plasma, two new unexpected but interesting points emerge: First, inspecting carefully the unbounded whistler wave dispersion (2.40) at high

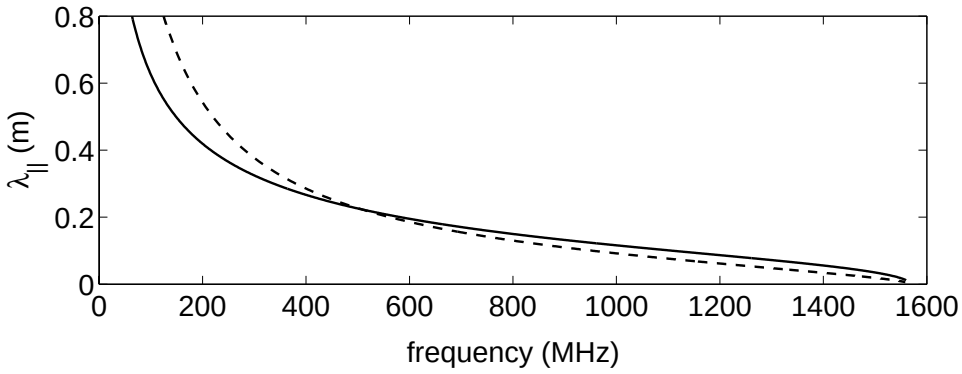

Figure 7.3: Whistler wave dispersion for $B_0 = 56\,\mathrm{mT}$ and $n = 4 \cdot 10^{16}\,\mathrm{m}^{-3}$. Shown are the results from a numerical simulation (dashed line) and the curve for unbounded R-waves (2.40) (solid line).

frequencies shows wavelength measurements that are systematically below the theoretical prediction. This becomes evident as the density is now more exactly determined. For the previous hollow profiles, the density range was too large to assert this and only an average density value was taken. Second, the radius R_c is used as a fit parameter to get a quantitative agreement between the measurements at low frequencies and the bounded wave theory. It turns out that the radius has to be chosen differently for each dispersion measurement. Physically, the radius R_c in Eq. (2.64) can be seen as the inverse of a perpendicular wave number $k_\perp$ (Sec. 2.4.1) that is determined by the boundary conditions at the conducting vessel walls. A change in R_c from experiment to experiment with values between 0.1–$0.2\,\mathrm{m}$ raises the question if the vessel walls really present the important boundary. To clarify these two points, the dispersion is numerically calculated by solving the ordinary differential Eqs. (2.54) and (2.55) given in Sec. 2.4.2. As mentioned above, this is very demanding and a previously evaluated code [Kleiber, 1996] is adapted to the present mathematical problem. Fig. 7.3 shows the whistler wave dispersion for $n = 4 \cdot 10^{16}\,\mathrm{m}^{-3}$ and $B_0 = 56\,\mathrm{mT}$ for the approximation Eq. (2.40) for R-waves in unbounded plasmas (solid line) and the numerically solved dispersion (dashed line). For the numerical calculation, a conducting cylindrical boundary with $R_c = 0.2\,\mathrm{m}$ and a homogeneous step-like plasma density distribution with $n = 4 \cdot 10^{16}\,\mathrm{m}^{-3}$ at $r \leq R_p = 0.05\,\mathrm{m}$ are assumed. For $R_p < r \leq R_c$ a vacuum gap is postulated. Although the plasma profile is quite unrealistic, the results are qualitatively correct and meaningful. In principle density distribution without discontinuous density jumps can be treated with the code as well, but the simple step-like profile is used for consistency with Uhm et al. [1988]. For frequencies below $\approx 500\,\mathrm{MHz}$, the numerically calculated dispersion relation yields wavelengths that are significantly larger than those from the unbounded whistler wave dispersion. This is consistent with the experimental observations discussed above. The influence of the boundary leads to an increase in the parallel wavelength. For frequencies above $\approx 500\,\mathrm{MHz}$, the numerically derived dispersion yields wavelengths that are slightly smaller than those from the unbounded whistler wave. This is as well consistent with the experimental obser-

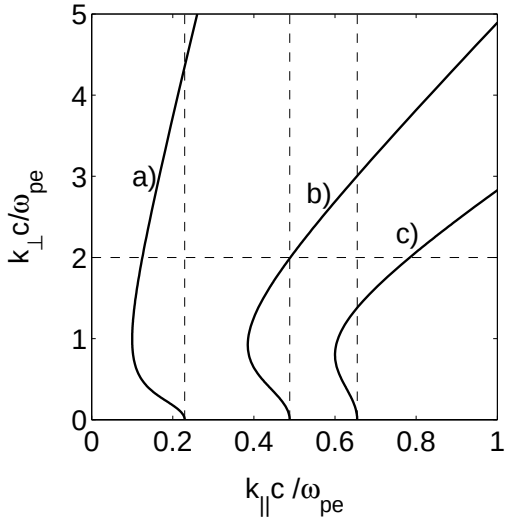

Figure 7.4: Normalised wave vector in a polar plot for three different normalised frequencies: a) $\omega = 0.01$, b) $\omega = 0.04$, and c) $\omega = 0.06$. Here, $\omega_{pe} = 2\omega_{ce} = 1$.

vations and can be understood physically from the polar plots of the wave vector ($k_\perp$ vs $k_\parallel$) in Fig. 7.4. Here, the normalised plasma and cyclotron frequencies are chosen to be $\omega_{pe} = 2\omega_{ce} = 1$. Shown are the polar plot diagrams at three different normalised frequencies: a) $\omega = 0.01$, b) $\omega = 0.04$, and c) $\omega = 0.06$. On the x-axis ($k_\perp = 0$) are the values for $k_\parallel$ that correspond to the case of the unbounded whistler waves (vertical dashed lines). We assume a boundary that introduces a constant perpendicular wave vector $k_\perp = 2$ (horizontal dashed line). At small frequencies, situation a), the parallel wave vector derived from this plot is smaller than expected for unbounded waves. This means, the parallel wavelength is larger than expected for unbounded wave propagation, consistent with the measurements and the approximate dispersion relations shown in Fig. 7.2. For high frequencies, situation c), the parallel wave vector derived for a bounded wave propagation is larger than for the unbounded wave. Thus, the wavelengths are smaller if a boundary is introduced. This is consistent with the results from the experiments and the numerical calculation. At one particular frequency, situation b), both parallel wavelengths, derived for bounded and unbounded waves, are identical. A perpendicular boundary thus not only leads to an increase in wavelength at low frequencies but also to a decrease in wavelength at higher frequencies. Having clarified this unexpected behaviour, the question of the exact value of the perpendicular wave vector is addressed. As mentioned above, a different perpendicular wave vector had to be postulated for each set of measurements to match the measured values at low frequencies quantitatively. The values are in a range between the conducting vessel radius $R_c = 0.2\,\mathrm{m}$ and the plasma radius $R_p = 0.05\,\mathrm{m}$. The radial profile of the amplitude of the magnetic fluctuations is therefore derived numerically for four different plasma radii and plotted in Fig. 7.5. The vessel radius is kept constant at $R_c = 0.2\,\mathrm{m}$ and the plasma profile is again step-like with $n = 4 \cdot 10^{16}\,\mathrm{m}^{-3}$ and radius $R_p = 0.2\,\mathrm{m}$ (solid line), $R_p = 0.15\,\mathrm{m}$ (dashed line), $R_p = 0.1\,\mathrm{m}$ (dash-dotted

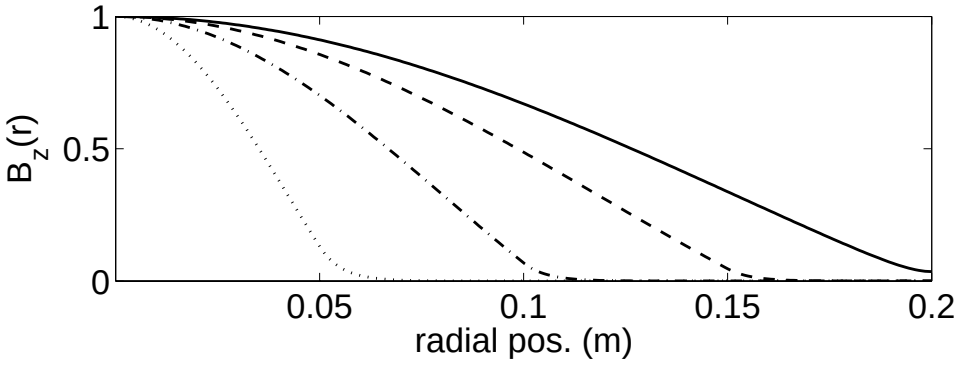

Figure 7.5: Numerically derived radial profile of the magnetic fluctuation amplitude B_z for different plasma radii: $R_p = 0.2\,\mathrm{m}$ (solid line), $R_p = 0.15\,\mathrm{m}$ (dashed line), $R_p = 0.1\,\mathrm{m}$ (dash-dotted line), and $R_p = 0.05\,\mathrm{m}$ (dotted line). The vessel radius is kept constant at $R_c = 0.2\,\mathrm{m}$.

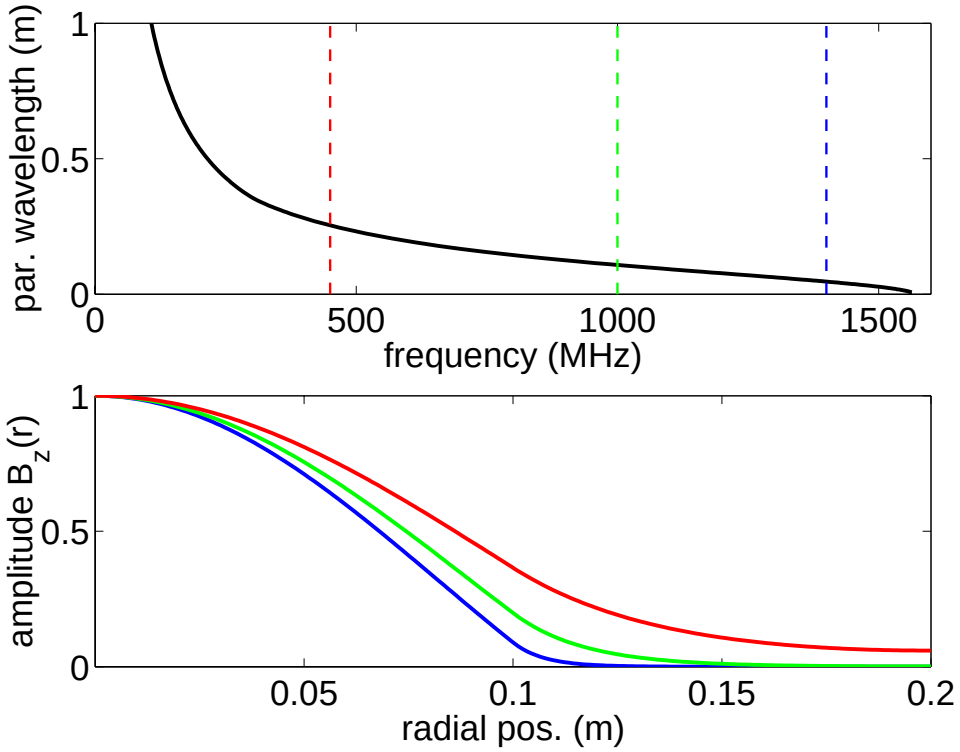

Figure 7.6: Numerically derived dispersion (top) and the respective radial profiles of the magnetic fluctuations (bottom) at the frequencies indicated by the coloured lines. The plasma parameters are: $B_0 = 56\,\mathrm{mT}$, $n = 4 \cdot 10^{16}\,\mathrm{m}^{-3}$, $R_c = 0.2\,\mathrm{m}$, and $R_p = 0.1\,\mathrm{m}$.

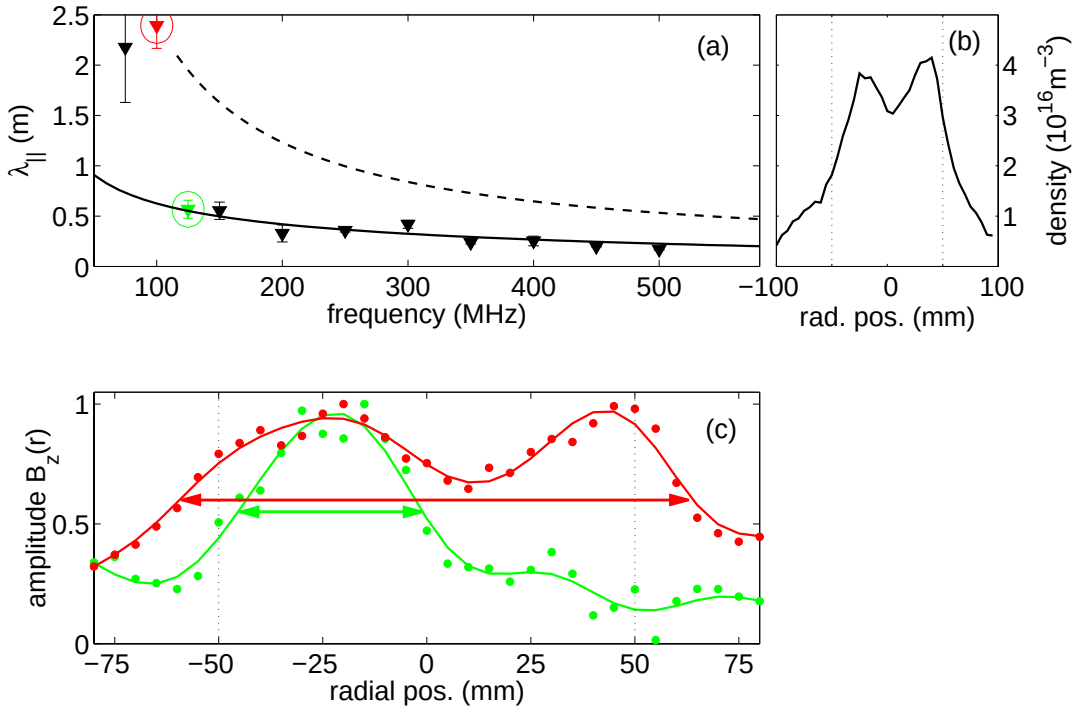

Figure 7.7: Whistler wave dispersion measurement for $n = 4 \cdot 10^{16}\,\mathrm{m}^{-3}$ and $B_0 = 56\,\mathrm{mT}$. Shown are the parallel wavelengths (a) and the radial fluctuation amplitude for two example cases ($100\,\mathrm{MHz}$ red, $125\,\mathrm{MHz}$ green) with significantly different parallel wavelengths (c). The radial plasma density profiles are shown in (b).

line), and $R_p = 0.05\,\mathrm{m}$ (dotted line). The parallel wave number is always kept constant at $k_\parallel = 175\,\mathrm{m}^{-1}$. It is clearly visible that it is the plasma radius rather than the vessel boundary that determines the radial wave number. Fig. 7.6 (top) shows the numerically derived dispersion relation with $R_c = 0.2\,\mathrm{m}$, $R_p = 0.1\,\mathrm{m}$, $n = 4 \cdot 10^{16}\,\mathrm{m}^{-3}$, and $B_0 = 56\,\mathrm{mT}$. The radial magnetic profiles at three different frequencies (indicated by the coloured vertical lines) are shown below. The radial profile is mainly determined again by the plasma radius rather than the vessel radius. But, the radial profiles are different for each frequency: The profile is wider for low frequencies than for high frequencies. This implies that the perpendicular wave number is not a constant for all frequencies along the dispersion curve and is smaller at smaller frequencies. Therefore, any theoretical approximation for bounded waves using constant $k_\perp$, like in Eq. (2.64), does not give a correct description. The effect of increasing parallel wavelength for decreasing frequency is even amplified by this. A $k_\perp$ smaller (a value below the dashed line in Fig. 7.4) for low frequencies (a) leads to a smaller $k_\parallel$. For high frequencies (c) an increasing $k_\perp$ leads to a larger $k_\parallel$, respectively. The slope of the dispersion curve is therefore steeper than calculated, just as observed for the parallel wavelengths in Fig. 7.2. This finding, so far only shown numerically, should be validated experimentally. Fig. 7.7 (a) shows a third set of dispersion measurements at $B_0 = 56\,\mathrm{mT}$ and $n \approx 4 \cdot 10^{16}\,\mathrm{m}^{-3}$. In addition to the parallel wavelengths, the radial modestructure is measured for each frequency at several axial positions. Two example measurements of the radial magnetic fluctuation profiles are shown in Fig. 7.7 (c) for two

different frequencies: $f = 100\,\text{MHz}$ (red) and $f = 125\,\text{MHz}$ (green), corresponding to a large (red) and a small (green) parallel wavelength. It is evident that at low frequencies the radial profile extends further to the plasma edge (red curve). In particular, it extends into the region outside of the antenna whereas it is restricted to the plasma region inside the antenna for the case of small parallel wavelength (green curve). The experimental and numerical results agree: The radial modestructure is not constant for all points on the dispersion curve and not solely determined by the conducting vessel boundary but varies and has to be determined for each frequency on the dispersion curve.

8

Discussion

Basic Wave Experiments

Whistler waves are excited in a magnetised plasma column and their dispersion is measured in two different discharge modes with high plasma density. The waves are identified by their right-hand polarisation (R-wave) and their dispersion behaviour. In this first set of measurements, a plasma parameter regime is chosen where the influence of the boundary is expected to be small. The measurements agree very well with the approximated theoretical dispersion of whistler waves in unbounded plasma geometry that is commonly used in ionospheric research (cf. Fig. 5.2). It is demonstrated that the approximation for wave dispersion in unbounded plasma geometry can be used in laboratory experiments if the perpendicular vessel dimension is much larger than the measured parallel wavelength ($\lambda_\parallel / R_c \ll 1$). This is in agreement with previous observations in other large volume plasma sources [Stenzel, 1976; Mattoo et al., 2001].

With almost the same experimental setup, waves are excited at frequencies around the ion cyclotron frequency $f_{c,He}$ in a helium plasma. For frequencies above $f_{c,He}$, the dispersion behaviour is in agreement with the expected R-wave. A gradually increasing deviation from the R-wave dispersion is observed for frequencies below $f_{c,He}$. This may be explained by taking the ion motion into account as well. Below $f_{c,He}$, there is also an L-wave propagation and the observed deviation is most likely due to a superposition or an interaction of the R-wave and the L-wave mode. First of all, the antenna excites both wave modes as the excitation scheme of the antenna is not selective to either polarisation. Moreover, both wave modes are linear polarised at a certain frequency in multi-species plasmas (cf. Sec. 2.3.4 for crossover frequency) and mode conversion can occur [Yeh and Liu, 1972; Ruud, 2000]. It is shown, however, that linear superposition of the waves alone cannot explain our measurements. Nonlinear effects might be of importance due to the high power used for wave excitation ($\approx 50\,\mathrm{W}$). In addition, the measurements with $\dot{B}$-probes at such low frequencies are very demanding and large size probes are used which possibly disturbed the wave propagation. To gain detailed information, the process must be analysed on a more basic level. Observations of the ion response give of course a much deeper insight into the mechanisms than collective behaviour as reflected in the magnetic fluctuation profiles. This suggests the use of LIF technique to measure the perturbed ion

distribution function (cf. Sec. 4.2.4 and [Sarfaty et al., 1996; Franck et al., 2000]). In addition, a more appropriate theoretical analysis will have to include the plasma boundary and the finite size effects of the antenna excitation scheme, as the measured wavelengths are rather long ($\lambda_\parallel = 1$–$3\,\mathrm{m}$). Nonetheless, these measurements are a first step towards a complete wave description including the ion motion. To our knowledge, this is the first experimental evidence of L-wave propagation in laboratory plasmas.

Whistler Wave Dispersion from Unbounded to Bounded Plasma

In a second experimental campaign, whistler waves are excited and their dispersion behaviour is investigated in a plasma with lower density. In contrast to the previous measurements, the plasma parameter regime is chosen to show a gradually increasing influence of the plasma boundary. The measurements are supported by numerical calculations to solve the nonlinear eigenvalue problem describing the wave propagation in a plasma filled waveguide. In the measured dispersion basically two different regimes could be distinguished. First, for high excitation frequencies, corresponding to parallel wavelengths smaller than the radial experimental dimensions ($\lambda_\parallel / R_c \lesssim 1$), the waves can be described reasonably well by unbounded wave theory, similar to the measurements in a high density plasma. In slight contrast to that, owing to the high accuracy of the wave measurements, it is observed that the wavelengths are systematically below the values predicted for unbounded plasma waves. This new and unexpected finding is consistent with the corresponding numerical calculations. A physical picture to explain this from bounded wave theory is the following: The polar plot of the wave vector (Fig. 7.4) shows that a large perpendicular wave number (corresponding to relatively small plasma extend in the radial direction) leads to an increase of the parallel wave number at higher frequencies. The parallel wavelength is therefore smaller than expected for unbounded plasma waves. This deviation decreases for increasing perpendicular plasma dimensions and approaches the unbounded limit for large experimental dimensions. This physical picture explains the measurements and supports the numerical simulations. In the second regime of the dispersion, at low excitation frequencies, the measured wavelengths are always larger than expected for unbounded plasma waves. Helicon wave theory as well as the more basic theoretical approach to describe waves propagating in a plasma-filled conducting vessel both predict the increase in wavelength for decreasing vessel radius. The approximation for low frequency waves in a completely filled waveguide with homogeneous plasma density distribution is able to reproduce the measured wavelengths quantitatively but cannot reproduce the exact shape of the entire dispersion curve. The perpendicular boundary must be introduced as a fit parameter for the quantitative explanation. It turns out that the perpendicular wave number is the key to the understanding of the wave propagation. Quantitative agreement was achieved for values of the perpendicular wave numbers that are in the range between the small plasma radius and the larger vessel radius. But the values are of course not constant for the different $k_\parallel$ measurements. Therefore, numer-

ical simulations were carried out to study the influence of the experimental conditions and of the plasma parameters on the radial mode structure. The numerical results reveal that it is rather the plasma dimensions (plasma radius) than the device dimension (vessel radius) that determines the radial modestructure. Moreover, the radial structure depends on the parallel wavelength and thereby on the excitation frequency as well. The numerics show that the radial modestructure extends further outside for large parallel wavelengths. While the radial profile for a small parallel wavelength is restricted to the plasma region, it extends further outside for long parallel wavelength, as shown in radial measurements of the magnetic fluctuations. These findings stand in contrast to any model or approximation that uses a fixed perpendicular wavenumber [Uhm et al., 1988; Chen, 1991]. These models are therefore not suitable to explain the full wave dispersion behaviour and can only be used for the limiting cases of unbounded whistler waves ($k_\perp \to 0$, shown above) or strongly bounded whistler waves ($k_\perp \approx 3.83/R_c$, shown below). Within these limiting cases however, both approximations are satisfactory. In summary, the investigations presented here give a complete picture of the wave propagation in bounded plasma geometry and delimit the regions in which common approximations are valid.

Helicon Wave Experiments

As a third aspect of whistler waves, strongly bounded helicon waves are investigated. Here, the boundary is essential for the dynamics of waves as they are, mathematically speaking, eigenfunctions of the plasma-boundary system. Helicon sources are widely used in laboratory experiments but the discharge mechanism of the high density mode is still a scientific case. This part of the work aims to contribute by investigating the equilibrium plasma parameters and the magnetic fluctuation profiles with high spatial resolution. Langmuir probe characteristics are recorded in the plane perpendicular to the magnetic field. Plasma parameter profiles reflect to some extend the fundamental discharge mechanisms (Fig. 6.1). The plasma production in the capacitive discharge mode occurs mainly in the antenna sheath region, where the power deposition due to ohmic and stochastic heating is largest. This is in full agreement with the simple model of magnetically enhanced capacitive discharges [Lieberman and Lichtenberg, 1994]. The discharge mechanism in the inductive mode was shown to be due to the electric fields induced by the large antenna currents within the skin depth layer of the plasma, again in agreement with simple discharge models [Lieberman and Lichtenberg, 1994]. In contrast to that, the plasma production in the helicon mode is completely detached from the antenna, which can be seen e.g. in the plasma density profile. This finding supports the assumption that the power deposition in the centre is mainly due to a propagating wave, the helicon wave [Light and Chen, 1995; Ellingboe and Boswell, 1996].

Detailed measurements of the poloidal mode structure of the wave magnetic fluctuations were made to gain insight in the difference of the heating mechanism between the capacitive and the helicon mode operation. In the capacitive mode, an $m = 0$ mode wave

was measured with a radial wave number $k_\perp = 3.83/0.1\,\mathrm{m}^{-1}$ and a parallel wave number of $k_\parallel = 2\pi/4\,\mathrm{m}^{-1}$. The perpendicular wave number is smaller than expected from the source tube diameter. This fact supports the physical picture that a helicon wave is driven and propagates in the plasma but has no significant impact on the plasma production. It is rather such that plasma is produced in the antenna sheaths and spreads out in the volume via cross field diffusion [Perry et al., 2002]. The helicon wave is excited by the rf fields of the antenna and propagates in the plasma with a modenumber determined self consistently from the plasma and device dimensions. The large axial wavelength is due to the low plasma density and is much larger than the antenna length $l = 0.3\,\mathrm{m}$. It is therefore not surprising that an $m = 0$ mode is excited, because the wave is, literally speaking, too large to be sensitive to the axial $m = 1$ structure of the antenna. Instead, only the ring ends of the antenna are seen by the wave, resembling a loop antenna with azimuthally symmetric $m = 0$ mode structure [Shamrai and Shinohara, 2001; Mouzouris and Scharer, 1998].

Magnetic fluctuations measurements were also made in a horizontal plane parallel to the ambient magnetic field in the helicon wave sustained discharge mode. Again, a clear $m = 1$ mode wave structure was identified with perpendicular wave number $k_\perp = 3.83/0.05\,\mathrm{m}^{-1}$ and parallel wave number $k_\parallel = 2\pi/0.15\,\mathrm{m}^{-1}$. In addition to that, curved and broken phase fronts were observed in the plot. This finding is in agreement with the picture of geometrical optics of a wave propagating oblique to the magnetic field until it is totally reflected at the reflection layer, similar to the propagation of light in an optical fibre. The angle between the phase front normals and the magnetic field is estimated to be in the range of $\theta = 78°$–$84°$. From these angles, a range of parallel and perpendicular wave vectors can be derived: $k_\parallel = 11$–$27\,\mathrm{m}^{-1}$ and $k_\perp = 75$–$200\,\mathrm{m}^{-1}$. These values are on the correct order of magnitude if compared to theoretically predicted values or to the previously measured. A truly satisfying agreement cannot be achieved for multiple reasons. First of all, the angle of the phase fronts changes if traced radially outwards with a propagation almost parallel to the magnetic field at $r > 40\,\mathrm{mm}$ (cf. Fig. 6.6). This is, of course, due to the plasma density gradient, i.e. the density decreases with increasing radial position. The parallel propagation of the phase fronts at radial positions with low plasma density can probably be explained by wave propagation in a vacuum wave guide. The axial and radial plasma density gradients must be fully taken into account and make it necessary to derive the parallel and perpendicular wave vectors locally at each position instead of assuming an average density. Therefore, only a range of wave vectors instead of an exact value was derived. A third interesting point is the exact location of the point of reflection. From Figs. 6.5 and 6.6 these points seem to be within $r = 20$–$40\,\mathrm{mm}$ and indicate a reflection layer instead of a sharp point. This wide range cannot be explained from inhomogeneities in the magnetic field strength or plasma density alone. But if one compares the gradient length $\approx 20\,\mathrm{mm}$ with the the wavelengths $\lambda_\parallel = 150\,\mathrm{mm}$ this is not surprising at all. In contrast to all other electromagnetic waves in plasmas, whistler waves do not exhibit a lower cut-off frequency and can consequently not be reflected

at a certain critical boundary layer. Thus, for a correct theoretical description, ray tracing calculation have to be made [Lundin and Krafft, 2002]. This possibility of directly measuring the phase distribution is a waveguide system is rather fascinating and in particularly promising to contribute to the understanding of the wave damping mechanism, which is dramatically altered due to this multiple reflections and interferences if compared to parallel wave propagation. To summarise this subsection, the observation of complex structured phase fronts strongly support the picture of a wave with oblique propagation being reflected at the plasma boundary layer.

Magnetic fluctuation profile measurements in the helicon mode were done in the planes parallel and perpendicular to the ambient magnetic field. As stated above, a clear $m = 1$ mode wave structure was identified and the wave numbers have been determined to be $k_\perp = 3.83/0.05\,\mathrm{m}^{-1}$ and $k_\parallel = 2\pi/0.15\,\mathrm{m}^{-1}$. In the theoretical treatment of helicon discharges it is usually assumed that the wave vectors are fully determined by the geometry of the source antenna [Light et al., 1995]. The measured values are in good agreement with the antenna radius and half the antenna length, fully supporting this assumption. From simple helicon wave theory one can see that the parallel and perpendicular wave numbers play a crucial role [Boswell and Chen, 1997; Chen and Boswell, 1997; Light and Chen, 1995]. The plasma density is self-consistently determined by Eq. (2.53), if the parallel and perpendicular wave numbers ($k_\parallel$ and $k_\perp$), the axial magnetic field strength B_0, and the rf frequency ω are given. In other words, the discharge geometry directly influences the plasma density. It was verified in the present work that this picture holds true: for a fixed antenna geometry and fixed rf frequency, the plasma density increase is proportional to the magnetic field strength (cf. Fig. 6.8). Consequently, the plasma density can in principle be changed by varying rf frequency and the antenna geometry. First experiments exploiting this principle were already successful [Gilland and Hershkowitz, 2001].

A particularly interesting behaviour of helicon sources is that the transition between the three discharge modes is discontinuous. It is well known for inductive discharges that the collisionless skin depth $\delta_p = c/\omega_{pe}$, and therefore the plasma density, is the crucial parameter for the transition from the capacitive mode to the inductive mode [Lieberman and Lichtenberg, 1994; Hopwood, 1992]. It was also shown that the inductive power coupling in unmagnetised discharges is most efficient when the skin depth δ_p equals the device radius R [Lieberman and Lichtenberg, 1994]. An axial magnetic field reduces the perpendicular conductivity and it was reported that the transition occurs at $\delta_p \approx R/2$ [Degeling et al., 1996]. The present measurements fully confirm the latter finding as the transition occurs at a plasma density of $n = 4 \cdot 10^{16}\,\mathrm{m}^{-3}$. At this density, the skin depth $\delta_p = 25\,\mathrm{mm} = R_{ant}/2$ is exactly half the source antenna radius. The measurements of the transition to helicon discharge mode contradict other existing models. It was previously suggested by Kaeppelin et al. [2001] that similarly to the transition from capacitive to inductive mode discharge, the plasma density is the control parameter determining the transition point from the inductive to the helicon wave sustained discharge. A ‘critical

density' [Kaeppelin et al., 2001] was derived from the helicon wave dispersion [Boswell, 1984b; Chen, 1991] at which the transition is expected to occur. In contrast to the measurements reported in [Kaeppelin et al., 2001], the present experiments show a discharge mode transition with a density increase by more than a factor of twenty. The 'critical density' calculates to be $n = 6.8 \cdot 10^{18}\,\mathrm{m}^{-3}$ in the experiments reported here, which is in good agreement with the centre-density in the helicon mode, but is orders of magnitude larger than the density in the capacitive mode. Moreover, the measurements show a transition from the capacitive mode directly to the helicon mode but remain at an intermediate density mode (inductive) in the downward direction. This as well contradicts models that assume the plasma density to be the control parameter for discharge mode transitions. A direct transition from the capacitive to the helicon wave sustained mode was previously reported at very low magnetic fields ($B < 3\,\mathrm{mT}$) [Degeling et al., 1996; Perry et al., 2002]. At such low magnetic fields, the plasma density calculated for the appropriate axial wavelength from the helicon wave dispersion is lower than the minimum density required for efficient inductive coupling. The transition therefore always goes directly from the capacitive mode to the helicon wave sustained mode and no inductive mode is established. In the present experiments, the magnetic field is considerably larger and the axial wavelength of the helicon wave is in agreement with helicon wave dispersion only in the high-density helicon regime. Therefore, the experiments clearly rule out the plasma density but suggest that the rf power density is the control parameter for the transition from the capacitive to the helicon mode as well as for the transition from the helicon mode to the inductive mode, which both occur at exactly the same forward rf power level.

9

Summary and Conclusions

Within the scope of this work, a large linear magnetised plasma device was designed to study whistler waves in bounded and unbounded plasma geometry. Besides the large geometric dimensions and the high plasma density at moderate magnetic fields, the machine concept put emphasis on easy accessibility and maintenance of the device, enabling a versatile use even beyond the extent of this work. The functionality and performance of the VINETA device fully met the conceptual expectations. The plasma is established by a standard rf helicon source with a right-helical antenna and can be operated in three different discharge modes. With it, the plasma density range extends over four orders of magnitude. Standard diagnostic tools like Langmuir probes, laser induced fluorescence measurements, and microwave interferometer measurements together with the computer controlled probe positioning systems were implemented successfully and yield all necessary background plasma parameters. For the wave measurements, magnetic fluctuations probes are used. An optimum probe design was identified and absolutely calibrated in external test fields.

Different aspects of whistler wave dispersion have been examined. First, whistler waves are excited in a high density plasma, where the boundary of the plasma is expected to have only little influence on the plasma. The waves are identified by their polarisation and their dispersion. It is explicitly demonstrated that the approximation for unbounded whistler waves can be used in laboratory experiments if the ratio of the parallel wavelength to the perpendicular experimental dimension is small ($\lambda_\parallel / R_c \ll 1$). This confirms earlier wave experiments in large volume plasma devices.

Second, an important aspect of whistler waves concerns helicon waves, whistler waves in strongly bounded plasma geometry ($\lambda_\parallel / R_c \approx 1$). These waves are used to produce a plasma with very high efficiency in so-called helicon sources. Although they are widely used in laboratory experiments, the detailed discharge mechanism is still far from being understood. The present work examines the equilibrium plasma parameters of all three discharge modes of helicon sources. The discharge mechanism in the capacitive and inductive modes were identified and are in agreement with the commonly accepted models. The helicon mode operation show clear signs of wave heating, completely detached from the antenna sheaths. This picture is confirmed by magnetic fluctuation profile measure-

ments in planes parallel and perpendicular to the ambient magnetic field with high spatial resolution. The phase measurements in planes parallel to the ambient magnetic field showed that the wave propagation in the helicon mode can be understood in terms geometrical optics as well. The waveguide situation resembles that of an optical fibre. The commonly used assumption that the parallel and perpendicular wave vectors in helicon discharges are mainly set by the antenna geometry was confirmed. Moreover, the plasma parameters are found to be determined self-consistently by the rf source parameters and the wave dispersion.

Not confirmed, in turn, is that the plasma density is the control parameter determining the transition from low density capacitive mode to high density helicon mode. In fact, high resolution measurements clearly rule out the plasma density as the critical parameter and indicate that the rf power density plays the pivotal role instead. The plasma density is just self-consistently established by the particular discharge mode.

As the third aspect of whistler waves, the transition regime between the two approximated dispersion behaviours, waves in unbounded and strongly bounded plasma geometry, is studied both experimentally and numerically. It is shown that the dispersion is not uniquely determined by measuring just the parallel wavelength. For a correct description, the perpendicular profile has to be taken into account. It is shown that in this intermediate wavelength region the perpendicular wave number is determined by the plasma dimensions and not, as usually assumed, by the conducting vessel boundary. Moreover, the perpendicular wave number is not at all constant for all frequencies, again in contrast to commonly used approximations. In so far, these experimental and numerical challenge some commonly accepted models for bounded whistler wave propagation.

A first step towards the more complete understanding of whistler wave propagation taking into account the ion motion is done. At frequencies below the ion cyclotron frequency $\omega_{c,He}$, right- and left-hand polarised waves were successfully excited. Whereas the dispersion above $\omega_{c,He}$ agrees with the R-wave dispersion, both wave modes interact below $\omega_{c,He}$ and the dispersion behaviour is strongly distorted. The experiments at such low frequencies turned out to be very difficult with magnetic fluctuation probes and refined diagnostics with the non-intrusive laser-induced fluorescence technique was tested and proposed for a more systematic study. Nonetheless, to our best knowledge, this is the first experimental evidence for L-wave propagation in a laboratory plasma.

Bibliography

A. Aanesland, C. Charles, R. Boswell, and A. Fredriksen. Helicon plasma modification by an immersed current carrying rf antenna. *Bull. Am. Phys. Soc.* **46**(8), UP1.45 (2001).

M. Abramowitz and I.A. Stegun. *Pocketbook of Mathmatical Functions*. Verlag Harri Deutsch Frankfurt/Main, Germany (1984).

P. Aigrain. Les "hélicons" dans les semiconducteurs. In *Proc. Conf. Semicond. Phys.* pages 224–227 Prague, Czeckoslovakia (1960).

J. E. Allen. Probe theories and applications: modern aspects. *Plasma Sources Sci. Technol.* **4**, 234–241 (1995).

Y. Al'pert. 40 years of whistlers. *J. Atmos. Terr. Phys.* **42**, 1–20 (1980).

J. Amorim, G. Baravian, and J. Jolly. Laser-induced resonance fluorescence as a diagnostic technique in non-thermal equilibrium plasmas. *J. Phys. D: Appl. Phys.* **33**, R51–R65 (2000).

APS Mini-Conference on Applications of Helicon Plasma Sources. . *Bull. Am. Phys. Soc.* **46(8)**, 30 (2001).

J. G. Bak, S. G. Lee, B. C. Kim, J. Hong, J. G. Yang, M. Kwon, and J. Chung. Diamagnetism measurements in the Hanbit magnetic mirror device. *Rev. Sci. Instrum.* **72**(1), 431–434 (2001).

M. M. Balkey, R. Boivin, J. L. Kline, and E. E. Scime. Ion heating and density production in helicon sources near the lower hybrid frequency. *Plasma Sources Sci. Technol.* **10**, 284–294 (2001).

J. F. Bamber, W. Gekelman, and J. E. Maggs. Whistler wave mode conversion to lower hybrid waves at a density striation. *Phys. Rev. Lett.* **73**(22), 2990–2993 (1994).

H. Barkhausen. Zwei mit Hilfe der neuen Verstärker entdeckte Erscheinungen. *Physik. Zeitschr.* **XX**, 401–403 (1919).

H. Barkhausen. Whistling tones from the earth. *Proceedings of the Institute of Radio Engineers* **18**(7), 1155–1159 (1930).

J. M. Beall, Y. C. Kim, and E. J. Powers. Estimation of wavenumber and frequency spectra using fixed probe pairs. *J. Appl. Phys.* **53**(6), 3933–3940 (1982).

D. Bilitza. International reference ionosphere – status 1995/96. *Adv. Space Res.* **20**(9), 1751–1754 (1997).

J. A. Bittencourt. *Fundamentals of Plasma Physics*. National Institute for Space Research (INPE) San Jose dos Campos, SP(BR) (1995).

D. C. Black and R. M. Mayo. High sensitivity, inductively coupled miniature mangetic probe array for detailed measurement of time varying magnetic field profiles in plasma flows. *Rev. Sci. Instrum.* **67**(4), 1508–1516 (1996).

D. D. Blackwell and F. F. Chen. Two-dimensional imaging of a helicon discharge. *Plasma Sources Sci. Technol.* **6**, 569–576 (1997).

D. D. Blackwell, T. G. Madziwa, D. Arnush, and F. F. Chen. Evidence for Trivelpiece-Gould Modes in a Helicon Discharge. *Phys. Rev. Lett.* **88**(14), 145002 (2002).

G. G. Borg and R. W. Boswell. Power coupling to helicon and Trivelpiece-Gould modes in a helicon source. *Phys. Plasmas* **5**(3), 564–571 (1998).

G. G. Borg and R. C. Cross. Guided propagation of Alfvén and ion-ion hybrid waves in a plasma with two ion species. *Plasma Phys. Controlled Fusion* **29**(6), 681–896 (1987).

G. G. Borg and T. Jahreis. Radio-frequency power combiner for cw and pulsed applications. *Rev. Sci. Instrum.* **65**(2), 449–452 (1994).

M. Born. *Ein Lehrbuch der elektromagnetischen Lichttheorie*. Springer Verlag Berlin, D 3 edition (1985).

R. W. Boswell. Effect of boundary conditions on radial mode structure of whistlers. *J. Plasma Phys.* **31**(2), 197–208 (1984)a.

R. W. Boswell. Very efficient plasma generation by whistler waves near the lower hybrid frequency. *Plasma Phys. Controlled Fusion* **26**(10), 1147–1162 (1984)b.

R. W. Boswell and F. F. Chen. Helicons – the early years. *IEEE Trans. Plasma Sci.* **25** (6), 1229–1244 (1997).

M. Brambilla. Propagation and absorption of waves at the lower hybrid resonance. *Plasma Phys.* **18**, 669–674 (1976).

M. Brambilla. Waveguide launching of lower hybrid waves. *Nucl. Fusion* **19**(10), 1343–1357 (1979).

N. Bretz. Diagnostic instrumentation for microturbulence in tokamaks. *Rev. Sci. Instrum.* **68**(8), 2927–2964 (1997).

F. R. Chang Diaz. Research status of the variable specific impulse magnetoplasma rocket. *Fusion Tech.* **35**(1T), 87–93 (1999).

F. R. Chang Diaz. The VASIMR rocket. *Sci. Am.* **283**(5), 90–97 (2000).

F. F. Chen. Electric probes. In H. Huddlestone, editor, *Plasma Diagnostic Techniques* pages 113–200. Academic Press New York (1965).

F. F. Chen. *Introduction to Plasma Physics and Controlled Fusion*. Plenum Press New York 2 edition (1984).

F. F. Chen. Plasma ionization by helicon waves. *Plasma Phys. Controlled Fusion* **33**(4), 339–364 (1991).

F. F. Chen. Experiments on helicon plasma sources. *J. Vac. Sci. Technol. A* **10**(4), 1389–1401 (1992).

F. F. Chen. Helicon plasma sources. In O. A. Popov, editor, *High Density Plasma Sources* pages 1–75. Noyes Publications Park Ridge, NJ, USA (1995).

F. F. Chen and D. D. Blackwell. Upper Limit to Landau Damping in Helicon Discharges. *Phys. Rev. Lett.* **82**(14), 2677–2680 (1999).

F. F. Chen and R. W. Boswell. Helicons - the past decade. *IEEE Trans. Plasma Sci.* **25** (6), 1245–1257 (1997).

F. F. Chen, J. D. Evans, and G. R. Tynan. Design and performance of distributed helicon sources. *Plasma Sources Sci. Technol.* **10**, 236–249 (2001).

F.F. Chen, M.J. Hsieh, and M. Light. Helicon waves in a non-uniform plasma. *Plasma Sources Sci. Technol.* **3**, 49–57 (1994).

B. Cherry. Lecture notes of the IMPRS mini course on electric probes. IPP, Greifswald, Germany (2000).

G. Chevalier and F. F. Chen. Experimental modeling of inductive discharges. *J. Vac. Sci. Technol. A* **11**(4), 1165–1171 (1993).

S. Cho. The role of the lower hybrid resonance in helicon plasmas. *Phys. Plasmas* **7**(1), 417–423 (2000).

S. Cho and J. G. Kwak. The effects of the density profile on the power absorption and the equilibrium density in helicon sources. *Phys. Plasmas* **4**(11), 4167–4172 (1997).

S. Cho and D. G. Swanson. Dispersion relations for the lower hybrid frequency range. *Phys. Fluids* **31**(5), 1123–1129 (1988).

M. A. Clilverd, A. J. Smith, and N. R. Thomson. The annual variation in quiet time plasmaspheric electron- density, determined from whistler mode group delays. *Planetary and Space Science* **39**(7), 1059–1067 (1991).

G. D. Conway, A. J. Perry, and R. W. Boswell. Evolution of ion and electron energy distributions in pulsed helicon plasma discharges. *Plasma Sources Sci. Technol.* **7**, 337–347 (1998).

A. Davey. On the Numerical Solution of Difficult Eigenvalue Problems. *J. Comput. Phys.* **24**, 331–338 (1977).

A. Degeling, N. Mikhelson, R. Boswell, and N. Sadeghi. Characterization of helicon waves in a magnetized inductive discharge. *Phys. Plasmas* **5**(3), 572–579 (1998).

A. W. Degeling, C. O. Jung, R. W. Boswell, and A. R. Ellingboe. Plasma production from helicon waves. *Phys. Plasmas* **3**(7), 2788–2796 (1996).

V. I. Demidov, S. V. Ratynskaia, R. J. Armstrong, and K. Rypdal. Probe measurements of electron energy distributions in a strongly magnetized low–pressure helium plasma. *Phys. Plasmas* **6**, 350–358 (1999).

V. I. Demidov, S. V. Ratynskaia, and K. Rypdal. Electric probes for plasmas: The link between theory and instrument. *Rev. Sci. Instrum.* **73**(10), 3409–3439 (2002).

C. P. DeNeef and A. J. Theiss. Effect of finite analyzer size on the distribution function measured in field-free plasmas. *Rev. Sci. Instrum.* **50**(3), 378–381 (1979).

G. Donoso and P. Martin. Space-charge effects in a velocity analyzer of variable geometry. *Rev. Sci. Instrum.* **61**(11), 3381–3383 (1990).

I. Duran, J. Stöckel, G. Mank, K. H. Finken, , G. Fuchs, and G. Van Oost. Measurement of magnetic field fluctuations using an array of Hall detectors on the TEXTOR tokamak. *Rev. Sci. Instrum.* **73**(10), 3482–3489 (2002).

A. Durandet, R. W. Boswell, and D. McKenzie. New plasma-assisted deposition technique using helcion activated reactive evaporation. *Rev. Sci. Instrum.* **66**(4), 2908–2913 (1995).

T. L. Eckersley. Musical Atmospherics. *Supplement to Nature* **January**, 104–105 (1935).

H. U. Eckert. The hundred year history of induction discharges. In Boening, editor, *Proceedings of the 2nd annual International Conference on Plasma Chemistry and Technology* pages 171–202. Technomic Lancaster, PA, USA (1986).

T. Edlington, R. Martin, and T. Pinfold. MAST magnetic diagnostics. *Rev. Sci. Instrum.* **72**(1), 421–425 (2001).

A. R. Ellingboe and R. W. Boswell. Capacitive, inductive and helicon-wave modes of operation of a helicon plasma source. *Phys. Plasmas* **3**(7), 2797–2804 (1996).

A. R. Ellingboe, R. W. Boswell, J. P. Booth, and N. Sadeghi. Electron beam pulses produced by helicon-wave excitation. *Phys. Plasmas* **2**(6), 1807–1809 (1995).

Equipe TFR. Tokamak plasma diagnostics. *Nucl. Fusion* **18**(5), 647–731 (1978).

R. K. Fisher and R. W. Gould. Resonance cones in the field pattern of a short antenna in an anisotropic plasma. *Phys. Rev. Lett.* **22**(21), 1093–1095 (1969).

C. M. Franck, O. Grulke, and T. Klinger. Investigation of the influence of different boundary conditions on helicon discharges. *Proceedings of the 11th International Congress on Plasma Physics* Sydney, Australia (2002)a.

C. M. Franck, O. Grulke, and T. Klinger. Magnetic fluctuation probe design and capacitive pickup rejection. *Rev. Sci. Instrum.* **73**(11), 3768–3771 (2002)b.

C. M. Franck, O. Grulke, and T. Klinger. Transition from unbounded to bounded plasma whistler wave dispersion. *Phys. Plasmas* **9**(8), 3254–3258 (2002)c.

C. M. Franck, O. Grulke, and T. Klinger. Mode transition in helicon discharges. *Phys. Plasmas* **10**(1), 323–325 (2003).

C. M. Franck, E. E. Scime, J. Kline, and T. Klinger. Wave electric field measurements of Trivelpiece-Gould waves in a helicon discharge. *Bull. Am. Phys. Soc.* **45**(7), GP 1.91 (2000).

B. D. Fried and S. D. Conte. *The Plasma Dispersion Function*. Academic Press (1961).

R. M. Gallet, J. M. Richardson, B. Wieder, G. D. Ward, and G. N. Harding. Microwave whistler mode propagation in a dense laboratory plasma. *Phys. Rev. Lett.* **4**(7), 347–349 (1960).

J. Gilland and N. Hershkowitz. Multiple antennae and power levels in a helicon discharge. *Bull. Am. Phys. Soc.* **46**(8), BM 1.6 (2001).

V. A. Godyak and R. B. Piejak. ICP diagnostics with magnetic probes. *J. Phys. IV France* **8**, 241–256 (1998).

M. J. Goeckner, J. Goree, and T. E. Sheridan. Laser-induced fluorescence characterization of a multidipole filament plasma. *Phys. Fluids B* **3**(10), 2913–2921 (1991).

R. J. Goldston and P. H. Rutherford. *Introduction to Plasma Physics*. Inst. of Phys. Pub. (1995).

H. R. Griem. *Principles of Plasma Spectroscopy*. Cambridge University Press Cambridge, UK (1997).

D. A. Gurnett, S. D. Shawhan, N. M. Brice, and R. L. Smith. Ion Cyclotron Whistlers. *J. Geophys. Res.* **70**(7), 1665–1688 (1965).

G. N. Harding and P. C. Thonemann. A study of helicon waves in indium. *Proc. Phys. Soc.* **85**, 317–328 (1965).

HARE© helicon source. Australian National University, licensed to Enya Ltd. (Japan); for details see [Durandet et al., 1995; Higgins et al., 1995].

H. J. Hartfuß. RF techniques in plasma diagnostics. *Plasma Phys. Controlled Fusion* **40**, A231–A250 (1998).

H. J. Hartfuß, T. Geist, and M. Hirsch. Heterodyne methods in millimetre wave plasma diagnostics with applications to ECE, interferometry and reflectometry. *Plasma Phys. Controlled Fusion* **39**, 1693–1769 (1997).

R. A. Helliwell. *Whistlers and Related Ionospheric Phenomena*. Stanford University Press Stanford, California, USA (1965).

N. Hershkowitz. How langmuir probes work. In O. Auciello and D. L. Flamm, editors, *Plasma Diagnostics* volume 1 pages 113–183. Academic San Diego, CA (1989).

B. Higgins, A. Durandet, and R. W. Boswell. Investigation of silicon transport in the neutral background of a plasma activated reactive evaporation system. *J. Vac. Sci. Technol. B* **13**(2), 192–197 (1995).

D. N. Hill, S. Fornaca, and M. G. Wickham. Single frequency scanning laser as a plasma diagnostic. *Rev. Sci. Instrum.* **54**(3), 309–314 (1983).

B. Hofmann-Wellenhof, H. Lichtenegger, and J. Collins. *Global Positioning System: Theory and Practice*. Springer Wien, AU 5 edition (2001).

J. Hopwood. Review of inductively coupled plasmas for plasma procesing. *Plasma Sources Sci. Technol.* **1**, 109–116 (1992).

P. Horowitz and W. Hill. *The Art of Electronics*. Cambridge University Press Cambridge 2nd edition (1989).

C. Hutchinson, editor. *The ARRL Handbook*. ARRL - the national association for Amateur Radio Newington, CT, USA 78 edition (2001).

I.H. Hutchinson. *Principles of Plasma Diagnostics*. Cambridge University Press (1987).

S. M. Hwang, G. S. Lee, J. G. Yang, K. K. Choh, J. H. Choi, J. W. Choi, K. S. chung, C. J. Dhoh, J. Hong, B. C. Kim, D. E. Kim an dW. C. Kim, H. K. Lee, S. G. Lee, H. K. Na, Y. K. Oh, H. L. Ynag, S. J. Yoo, N. S. Yoon, K.-I. You, and Duk-In Choi. Present status of HANBIT magnetic mirror device. *Nucl. Fusion* **35**, 99–106 (1999).

J. D. Jackson. *Classical Electrodynamics*. Wiley New York, USA 3 edition (1999).

V. Kaeppelin, M. Carrère, and J. B. Faure. Different operational regimes in a helicon plasma source. *Rev. Sci. Instrum.* **72**(12), 4377–4382 (2001).

P. Keiter. *Experimental Investigation of Ion Temperature Anisotropy Driven Instabilities in a High Beta Plasma*. PhD thesis West Virginia University, (WV) USA (1999).

P. A. Keiter, E. E. Scime, and M. M. Balkey. Frequency dependent effects in helicon plasmas. *Phys. Plasmas* **4**(7), 2741–2747 (1997).

G. H. Kim, N. Hershkowitz, D. A. Diebold, and M. H. Cho. Magnetic and collisional effects on presheaths. *Phys. Plasmas* **2**(8), 3222–3233 (1995).

G. Klawitter. *Ionosphäre und Wellenausbreitung*. Siebel Meckenheim, D 3 edition (2000).

R. Kleiber. *Zur Stabilität astrophysikalisch relevanter rotierender viskoser Überschallströmungen*. PhD thesis Georg-August Universität zu Göttingen (1996).

J. Kline, C. M. Franck, and R. Spangler. First order perturbed velocity distribution theory and measurement. Technical report West Virginia University, Plasma Physics Group WV, USA (2000).

J. P. Klozenberg, B. McNamara, and P. C. Thoneman. The dispersion and attenuation of helicon waves in a uniform cylindrical plasma. *J. Fluid Mech.* **21**(3), 545–563 (1965).

A. Komori, T. Shoji, K. Miyamoto, J. Kawai, and Y. Kawai. Helicon waves and efficient plasma production. *Phys. Fluids B* **3**(4), 893–898 (1991).

H. H. Kuehl. Electromagnetic radiation from an electric dipole in a cold anisotropic plasma. *Phys. Fluids* **5**(9), 1095–1103 (1962).

J. G. Kwak, H. D. Choi, H. I. Bak, S. Cho, J. G. Bak, and S. K. Kim. Frequency dependence of the plasma density for helicon plasmas. *Phys. Plasmas* **4**(5), 1463–1467 (1997).

L. D. Landau and E. M. Lifschitz. *Lehrbuch der theoretiscen Physik II*. Akademie Verlag Berlin, D 7 edition (1977).

E. Leer, K. M. Johansen, and R. Albrigtsen. Group Velocity of Whistlers in a Two-Ion Plasma. *J. Geophys. Res.* **83**(A7), 3125–3135 (1978).

C. R. Legéndy. Macroscopic theory of helicons. *Phys. Rev.* **135**(6A), 1713–1724 (1965).

J. A. Lehane and P. C. Thonemann. An experimental study of helicon wave propagation in a gaseous plasma. *Proc. Phys. Soc.* **85**, 301–316 (1965).

M. A. Lieberman. Analytic Solution for Capacitive RF Sheath. *IEEE Trans. Plasma Sci.* **16**(6), 638–644 (1988).

M. A. Lieberman and A. J. Lichtenberg. *Principles of Plasma Discharges and Materials Processing*. John Wiley & SONS, INC. New York (1994).

M. A. Lieberman, A. J. Lichtenberg, and S. E. Savas. Model of Magnetically Enhanced Capacitive RF Discharges. *IEEE Trans. Plasma Sci.* **19**(2), 189–196 (1991).

M. Light and F. F. Chen. Helicon wave excitation with helical antennas. *Phys. Plasmas* **2** (4), 1084–1093 (1995).

M. Light, I. D. Sudit, F. F. Chen, and D. Arnush. Axial propagation of helicon waves. *Phys. Plasmas* **2**(11), 4094–4102 (1995).

P. K. Loewenhardt, B. D. Blackwell, R. W. Boswell, G. D. Conway, and S. M. Hamberger. Plasma production in a toroidal heliac by helicon waves. *Phys. Rev. Lett.* **67**(20), 2792–2794 (1991).

P. K. Loewenhardt, B. D. Blackwell, and S. M. Hamberger. Helicon wave propagation in the SHEILA heliac. *Plasma Phys. Controlled Fusion* **27**, 229–254 (1995).

P. K. Loewenhardt, B. D. Blackwell, and Beichao Zhang. A simple miniature magnetic probe with inherent electrostatic rejection. *Rev. Sci. Instrum.* **64**(11), 3334–3335 (1993).

R. H. Lovberg. Magnetic probes. In L. Huddlestone, editor, *Plasma Diagnostic Techniques* pages 69–112. Academic Press New York (1965).

B. V. Lundin and C. Krafft. Modified electron whistler dispersion law. *J. Plasma Phys.* **67**(2-3), 149–161 (2002).

D. W. Mahaffey. Microwave porpagation through a plasma in a magnetic field. *Phys. Rev.* **129**(4), 1481–1488 (1963).

G. Mank, I. Duran, K.H. Finken, and G. Van Oost. Measurement of magnetic fluctuations by means of a multiple Hall probe in TEXTOR-94. *Verhandl. DPG* **VI, 36**(5), P 8.12 (2001).

S. K. Mattoo, V. P. Anitha, L. M. Awasthi, G. Ravi, and LVPD-Team. A large volume plasma device. *Rev. Sci. Instrum.* **72**(10), 3864–3872 (2001).

S. Mazouffre, C. Foissac, P. Supiot, P. Vankan, R. Engeln, D. C. Schram, and N. Sadeghi. Density and temperature of N atoms in the afterglow of a microwave discharge measured by a two-photon laser-induced fluorescence technique. *Plasma Sources Sci. Technol.* **10**, 168–175 (2001).

D. J. McEwen and R. E. Barrington. Ion composition below 3000 km derived from ion whistler observations. In A. P. Mitra, L. G. Jacchia, and W. S. Newman, editors, *COSPAR space research VIII* pages 396–404 Amsterdam (1968). North-Holland Publishing Company.

A. W. Molvik, A. R. Ellingboe, and T. D. Rognlien. Hot-electron production and wave structure in a helicon plasma source. *Phys. Rev. Lett.* **79**(2), 233–236 (1997).

MORI© helicon source. Plasma & Materials Technologies (Trikon), Inc., Cal., USA; for details see [Tynan et al., 1997].

Y. Mouzouris and J. E. Scharer. Wave propagation and absoption simulations for helicon sources. *Phys. Plasmas* **5**(12), 4253–4261 (1998).

L. Muschietti, I. Roth, and G. Delory. Oblique turbulence driven by field-aligned electron fluxes in the auroral ionosphere. *J. Geophys. Res.-Space Phys.* **102**(A12), 27217–27226 (1997).

D. R. Nicholson. *Introduction to Plasma Theory*. John Wiley & Sons New York, USA (1983).

J. C. Park and B. Kang. Reactor Modeling of Magnetically Enhanced Capacitive RF Discharge. *IEEE Trans. Plasma Sci.* **25**(3), 499–506 (1997).

H. L. Pécseli. *Fluctuations in Physical Systems*. Cambridge University Press Cambridge, UK (2000).

A. Perry, G. Conway, R. Boswell, and H. Persing. Modulated plasma potentials and cross field diffusion in a helicon plasma. *Phys. Plasmas* **9**(7), 3171–3177 (2002).

A. J. Perry, D. Vender, and R. W. Boswell. The application of the helicon source to plasma processing. *J. Vac. Sci. Technol. B* **9**(2), 310–317 (1991).

R. C. Phillips and E. B. Turner. Construction and calibration technique of high frequency magnetic probes. *Rev. Sci. Instrum.* **36**(12), 1822–1825 (1965).

R. I. Pinsker. Introduction to wave heating and current drive in magnetized plasmas. *Phys. Plasmas* **8**(4), 1219–1228 (2001).

W. H. Preece. Earth currents. *Letters, Nature London* **49**, 554 (1894).

M. B. Priestley. *Spectral Analysis and Time Series*. Academic Press San Diego 6 edition (1989).

J. P. Rayner, A. D. Cheetham, and G. N. French. Radio frequency matching for helicon plasma sources. *J. Vac. Sci. Technol. A* **14**(4), 2048–2055 (1996).

P. G. Richards, T. Chang, and R. H. Comfort. On the causes of the annual variation in the plasmaspheric electron density. *J. Atmos. Solar-Terr. Phys.* **62**, 935–946 (2000).

K.-U. Riemann. The bohm criterion and sheath formation. *J. Phys. D: Appl. Phys.* **24**, 493–518 (1991).

C. L. Rousculp, R. L. Stenzel, and J. M. Urrutia. Pulsed currents carried by whistlers. Part V: Detailed new results of magnetic antenna excitation. *Phys. Plasmas* **2**(11), 4083–4093 (1995).

T. S. Ruud. Plasma Wave Phenomena observed with the FREJA satellite. Master's thesis University of Oslo (2000).

M. Sarfaty, S. De Souza-Machado, and F. Skiff. Direct determination of ion wave fields in a hot magnetized and weakly collisional plasma. *Phys. Plasmas* **3**(12), 4316–4324 (1996).

D. A. Schneider, G. G. Borg, and I. V. Kamenski. Measurements and code comparison of wave dispersion and antenna radiation resistance for helicon waves in a high density cylindrical plasma source. *Phys. Plasmas* **6**(3), 703–712 (1999)a.

T. P. Schneider, W. W. Dostalik, A. D. Springfield, and R. Kraft. Langmuir probe studies of a helicon plasma system. *Plasma Sources Sci. Technol.* **8**(3), 397–403 (1999)b.

U. Schumacher. *Fusionsforschung*. Wissenschaftliche Buchgesellschaft Darmstadt, D (1993).

E. E. Scime, P. A. Keiter, , M. W. Zintl, M. M. Balkey, J. L. Kline, and M. E. Koepke. Control of ion temperature anisotropy in a helicon plasmas. *Plasma Sources Sci. Technol.* **7**, 186–191 (1998).

M. R. Scott. An Initial Value Method for the Eigenvalue Problem for Systems of Ordinary Differential Equations. *J. Comput. Phys.* **12**, 334–347 (1973).

G. D. Severn, D. A. Edrich, and R. McWilliams. Argon ion laser-induced fluorescence with diode lasers. *Rev. Sci. Instrum.* **69**(1), 10–15 (1998).

K. P. Shamrai and S. Shinohara. Spectral and spatial characterization of a radio frequency power absorption in high pressure helicon plasmas. *Phys. Plasmas* **8**(10), 4659–4674 (2001).

K. P. Shamrai and V. B. Taranov. Resonances and anti-resonances of a plasma-column in a helicon plasma source. *Phys. Lett. A* **204**(2), 139–145 (1995).

K. P. Shamrai and V. B. Taranov. Volume and surface rf power absorption in a helicon plasma source. *Plasma Sources Sci. Technol.* **5**, 474–491 (1996).

T. Shoji, Y. Sakawa, S. Nakazawa, K. Dadota, and T. Sato. Plasma production by helicon waves. *Plasma Sources Sci. Technol.* **2**, 5–10 (1993).

F. Skiff. Determination of wave fields from perturbed particle orbits. *IEEE Trans. Plasma Sci.* **20**(6), 701–704 (1992).

F. Skiff and F. Anderegg. Direct observation of plasma dielectric motion. *Phys. Rev. Lett.* **59**(8), 896–899 (1987).

D. E. Smith, E. J. Powers, and G. S. Caldwell. Fast–Fourier–Transform Spectral–Analysis Techniques as a Plasma Fluctuation Diagnostic Tool. *IEEE Trans. Plasma Sci.* **PS-2**, 261–272 (1974).

R. L. Smith and N. Brice. Propagation in Multicomponent Plasmas. *J. Geophys. Res.* **69** (23), 5029–5040 (1964).

R. L. Smith, N. M. Brice, J. Katsufrakis, D. A. Gurnett, S. D. Shawhan, J. S. Belrose, and R. E. Barrington. An ion gyrofrequency phenomenon observed in satellites. *Letters, Nature* **204**, 274–275 (1964).

V. S. Sonwalkar, X. Chen, J. Harikumar, D. L. Carpenter, and T. F. Bell. Whistler-mode wave-injection experiments in the plasmasphere with a radio sounder. *J. Atmos. Solar-Terr. Phys.* **63**(11), 1199–1216 (2001).

SR830. *DSP Lock-In Amplifier Manual*. Stanford Research Systems. chapter 3.

P. C. Stangeby. *The Plasma Boundary of Magnetic Fusion Devices*. Series in Plasma Physics. IOP Publishing Bristol, UK (2000).

R. L. Stenzel. Whistler wave propagation in a large magnetoplasma. *Phys. Fluids* **19**(6), 857–864 (1976).

R. L. Stenzel. Whistler waves in space and laboratory plasmas. *J. Geophys. Res.* **104**(A7), 14379–14395 (1999).

R. L. Stenzel and J. M. Urrutia. Pulsed currents carried by whistlers. Part VII: Helicity and transport in heat pulses. *Phys. Plasmas* **3**(7), 2599–2609 (1996).

R. L. Stenzel and J. M. Urrutia. Pulsed currents carried by whistlers. Part VIII: Current disruptions and instabilities caused by plasma erosion. *Phys. Plasmas* **4**(1), 26–35 (1997).

R. L. Stenzel, J. M. Urrutia, and C. L. Rousculp. Pulsed currents carried by whistlers. Part I: Excitation by magnetic antennas. *Phys. Fluids B* **5**(2), 325–338 (1993).

R. L. Stenzel, J. M. Urrutia, and C. L. Rousculp. Pulsed currents carried by whistlers. Part IV: Electric fields and radiation excited by an electrode. *Phys. Plasmas* **2**(4), 1114–1128 (1995).

Stenzel I-IX. Stenzel et al. [1993]; Urrutia et al. [1994, 1995]; Stenzel et al. [1995]; Rousculp et al. [1995]; Urrutia and Stenzel [1996]; Stenzel and Urrutia [1996, 1997]; Urrutia and Stenzel [1997].

R. A. Stern and J. A. Johnsen III. Plasma ion diagnostics using resonant fluorescence. *Phys. Rev. Lett.* **34**(25), 1548–1551 (1975).

T. H. Stix. Radiation and absorption via mode conversion in an inhomogeneous collision-free plasma. *Phys. Rev. Lett.* **15**(23), 878–882 (1965).

T. H. Stix. *Waves in Plasmas*. AIP New York, USA (1992).

I. D. Sudit and F. F. Chen. A non-singular helicon waves equation for a non-uniform plasma. *Plasma Sources Sci. Technol.* **3**, 602–603 (1994)a.

I. D. Sudit and F. F. Chen. RF compensated probes for high-density discharges. *Plasma Sources Sci. Technol.* **3**, 162–168 (1994)b.

D. G. Swanson. *Plasma Waves*. Academic Press San Diego, CA, USA (1989).

K. Tachibana. VUV to UV laser spectroscopy of atamic species in processing plasmas. *Plasma Sources Sci. Technol.* **11**, A166–A172 (2002).

S. Takechi, S. Shinohara, and A. Fukuyama. Characteristics of RF wave propagation in large–diameter plasma with cusp magnetic field configuration. *Jap. J. Appl. Phys.* **38** (6A), 3716–3722 (1999).

S. Tanaka, S. Ichimura, M. Takayama, M. Inutake, S. Kanazawa, M. Nakamura, E. Ishikawa, C. Satake, S. Motegi, T. Saito, H. Hojo, A. Mase, K. Ishii, T. Tamano, and K. Yatsu. Low frequency fluctuations measured by probes in the GAMMA10 tandem mirror. *Rev. Sci. Instrum.* **70**(1), 979–982 (1999).

V. Y. Trakhtengerts and M. J. Rycroft. Sounding the magnetosphere by signals from VLF radio transmitters. *J. Atmos. Solar-Terr. Phys.* **60**(5), 545–549 (1998).

S. K. P. Tripathi and D. Bora. Normal modes of bounded whistler produced toroidal plasmas. *Phys. Plasmas* **8**(3), 697–703 (2001).

A. W. Trivelpiece and R. W. Gould. Space charge waves in cylindrical plasma columns. *J. Appl. Phys.* **30**(11), 1784–1793 (1959).

G. R Tynan, A. D. Bailey III, G. A Campbell, R. Charatan, A. de Chambrier, G. Gibson, D. J. Hemker, K. Jones an A. Kuthi, C. Lee, T. Shoji, and M. Wilcoxson. Characterisation of an azimuthally symmetric helicon wave high density plasma source. *J. Vac. Sci. Technol. A* **15**(6), 2885–2892 (1997).

H. S. Uhm, K. T. Nguygen, R. F. Schneider, and J. R. Smith. Wave dispersion theory in a plasma column bounded by a cylindrical waveguide. *J. Appl. Phys.* **64**(3), 1108–1115 (1988).

J. M. Urrutia and R. L. Stenzel. Pulsed currents carried by whistlers. Part VI: Nonlinear effects. *Phys. Plasmas* **3**(7), 2589–2598 (1996).

J. M. Urrutia and R. L. Stenzel. Pulsed currents carried by whistlers. Part IX: In situ measurements of currents disrupted by plasma erosion. *Phys. Plasmas* **4**(1), 36–52 (1997).

J. M. Urrutia, R. L. Stenzel, and C. L. Rousculp. Pulsed currents carried by whistlers. Part II: Excitation by biased electrodes. *Phys. Plasmas* **1**(5), 1432–1438 (1994).

J. M. Urrutia, R. L. Stenzel, and C. L. Rousculp. Pulsed currents carried by whistlers. Part III: Magnetic fields and currents excited by an electrode. *Phys. Plasmas* **2**(4), 1100–1113 (1995).

B. Vowinkel. *22–40 GHz Interferometer*. Amtron GmbH Harzstr. 1c, 58706 Menden (2000).

J. Wesson. *Tokamaks*. Clarendon Press Oxford second edition (1997).

C. K. Yeh and C. H. Liu. *Theory of Ionospheric Waves*. Academic Press New York, USA (1972).

S. M. Yun and H. Y. Chang. Radial density profile change near lower hybrid frequency in m=0 helicon wave plasmas. *Phys. Lett. A* **248**, 400–404 (1998).

P. Zhu and R. W. Boswell. Ar II laser generated by landau damping of whistler waves at the lower hybrid frequency. *Phys. Rev. Lett.* **63**(26), 2805–2807 (1989).

Acknowledgements

First of all I thank Prof. Klinger for offering me to do my Ph.D. in his group. His continuous interest and confidence in my work and the wide autonomy and responsibilities he allowed during the time were ideal and stimulating.

I'm also thankful to Prof. Scime for his hospitality and the challenging work during my time in West Virginia. Moreover, I'm indebted for his valuable help with the helicon source setup during his stay in Greifswald and the many suggestions on diode-laser LIF.

Many thanks to Dr. Grulke for numerous discussions and his practical support, to Thomas Kinder for his extensive help with the LIF construction and setup, to Dr. Kleiber for openly sharing his eigenvalue solver and for helping me to adjust it to the appropriate differential equations and boundary conditions, to Prof. Pécseli for suggesting ion whistler wave experiments and openly sharing his unpublished results, to Prof. Bonhomme for many valuable discussions and suggestions, to Dr. Thomsen for lively discussions not only about physics, and to Prof. Boswell for initiating and stimulating recommendations during his stay in Greifswald.

The numerous and excellent pieces of work for the VINETA experiment from both workshops of the physics department of the university and of the Max-Planck-Institut in Greifswald are gratefully acknowledged. Without their help, this work would have never been possible, especially not within this period of time.

The social component during work-life was ensured by the other graduate students and the rest of the VINETA team. I enjoyed especially the habits and opinions from almost all around the world.

The manuscript was proof-read by (in alphabetical order) Prof. Bonhomme, Jade Comfort, Dr. Grulke, Dr. Thomsen, and Jacob Zalach. Thank you very much.

A big big hug is to Birte Hein who counter-balanced all my moody moments which are inevitably triggered by writing such a thesis. Without her, I'd likely gone mad of physics.